ABSTRACT

Title of Dissertation: LIPID FORCE FIELD PARAMETERIZATION FOR IMPROVED MODELING OF ION-LIPID INTERACTIONS AND ETHER LIPIDS, AND EVALUATION OF THE EFFECTS OF LONG-RANGE LENNARD-JONES INTERACTIONS ON ALKANES

Alison N. Leonard, Doctor of Philosophy, 2019

Dissertation directed by: Dr. Jeffery B. Klauda
Associate Professor
Department of Chemical and Biomolecular Engineering

Chemical specificity of lipid models used in molecular dynamics simulations is essential to accurately represent the complexity and diversity of biological membranes. This dissertation discusses contributions to the CHARMM36 (C36) family of lipid force fields, including a revised model for the glycerol-ether linkage found in plasmalogens and archaeal membranes; interaction parameters between ions and lipid oxygens; and evaluation of the effects of long-range Lennard-Jones parameters on alkanes.

Long-range Lennard-Jones interactions have a significant impact on structural and thermodynamic properties of systems with nonpolar regions such as membranes. Effects of these interactions on properties of alkanes are investigated. Implementation of the Lennard-Jones particle-mesh Ewald (LJ-PME) method with the C36 additive and Drude polarizable force fields improves agreement with experiment for thermodynamic and kinetic properties of alkanes, with Drude outperforming the additive FF for nearly all quantities. Trends in the temperature dependence of the density and isothermal compressibility are also improved.

Phospholipids containing an ether linkage between the glycerol backbone and hydrophobic tails are prevalent in human red blood cells and nerve tissue. *Ab initio* results are used to revise linear ether parameters and develop new parameters for the glycerol-ether linkage in lipids. The new force field, called C36e, more accurately represents the dihedral potential energy landscape and improves solution properties of linear ethers. C36e allows more water to penetrate an ether-linked lipid bilayer, increasing the surface area per lipid compared to simulations carried out with the original C36 parameters and improving structural properties.

In addition to modulating membrane structure, lipid-ion interactions influence protein-ligand binding and conformations of membrane-bound proteins. Interaction parameters are introduced describing Be^{2+} affinity for binding sites on lipids. Experimental binding affinities reveal that Be^{2+} strongly binds to phosphoryl groups. Revised interaction parameters reproduce binding affinities in solution simulations. In a separate effort, experimental results for the radius of gyration (R_g) of polyethylene glycol (PEG) in various concentrations of KCl reveal that, while C36e parameters reproduce experimental R_g of PEG in the absence of KCl, adding salt results in underestimation of R_g. It is found that the water shell around PEG affects R_g calculated from neutron scattering experiments, and K^+-PEG interactions increase the *gauche* character of PEG.

LIPID FORCE FIELD PARAMETERIZATION FOR IMPROVED MODELING OF ION-LIPID INTERACTIONS AND ETHER LIPIDS, AND EVALUATION OF THE EFFECTS OF LONG-RANGE LENNARD-JONES INTERACTIONS ON ALKANES

by

Alison N. Leonard

Dissertation submitted to the Faculty of the Graduate School of the
University of Maryland, College Park, in partial fulfillment
of the requirements for the degree of
Doctorate of Philosophy, 2019.

Advisory Committee:
Dr. Jeffery B. Klauda, chair
Dr. Christopher Jarzynski
Dr. Silvina Matysiak
Dr. Sergei Sukharev, Dean's representative
Dr. John Weeks

Chapter 1
Alison N. Leonard, Eric Wang, Viviana Monje-Galvan, and Jeffery B. Klauda

Chapter 2
Alison N. Leonard, Andrew C. Simmonett , Frank C. Pickard IV, Jing Huang, Richard M. Venable, Jeffery B. Klauda, Bernard R. Brooks, and Richard W. Pastor

Chapter 3
Alison N. Leonard, Richard W. Pastor, and Jeffery B. Klauda

Chapter 4
Alison N. Leonard, Jeffery B. Klauda, and Sergei Sukharev

Dedication

For Hua Tong, "Alex" Linhe Xu, and Frank Battaglino. Teachers, experts, and leaders begin as students. They ultimately succeed because their compulsion to learn continues beyond the years of formal education.

Acknowledgements

With Jeffery Klauda's patient guidance and technical expertise, I was able to overcome research obstacles, develop the scope of research aims, think critically, take personal responsibility, and avoid or correct mistakes (not a skill to be overestimated). His flexibility with my work schedule enabled me to continue my studies after having children and, over time, to appropriately balance professional and personal responsibilities.

Conversations with Richard Pastor about lipids, numerical methods, the history of molecular dynamics (I once found a punch card in his office!), and the nuances of professionalism in our field have been immeasurably helpful in preparing me for the next step in my pursuit of a career in academia. Additionally, his exploratory approach to developing research aims resulted in well-organized publications that each tell a coherent story.

I was able to expand my skills beyond molecular dynamics by collaborating with experimentalist Sergei Sukharev, who instructed and assisted me in isothermal titration calorimetry and osmolality measurements. His insight into and experience with Be^{2+}/DOPS interactions informed research aims in Chapter 4 of this dissertation.

I am grateful for Rick Venable's extensive technical and scientific knowledge of how to properly design and run all-atom molecular dynamics simulations to answer research questions, and for his expertise in scripting and data analysis, some of which he has passed on to me.

I also enjoyed discussions with Andy Simmonet about quantum mechanical calculations and with Andreas Kraemer about mathematical methods and running simulations in GROMACS. I would like to thank Arvind Balijepalli for providing neutron scattering data for polyethylene glycol, and Jochen S. Hub and Milos T. Ivanovic for providing the GROMACS build that computes X-ray and neutron scattering curves from all-atom molecular dynamics simulations with explicit solvent.

I have enjoyed the company and encouragement of my family, especially Gideon, who discusses my work and asks about my posters and slides. I look forward to more in-depth discussions as the children grow.

Contents

Tables

Figures

Abbreviations

C22 – CHARMM22

C27 – CHARMM27

C27r – CHARMM27 revised

C36 – CHARMM36

CCSD – Coupled Cluster Single-Double

Cer – ceramide

CHARMM – Chemistry at Harvard Molecular Mechanics

Chol – cholesterol

DBOE - dibutoxyethane

DBOE – dibutoxyethane

DEOE - diethoxyethane

DFFT – Decomposition Fast Fourier Transform

DHPC – 1,2-di-O-hexadecyl-*sn*-glycero-phosphatidylcholine

DLPC – 1,2-dilauroyl-*sn*-phosphatidylcholine

DMOE – dimethoxyethane

DMPC – 1,2-dimyristoyl-*sn*-phosphatidylcholine

DOPC – 1,2dioleoyl-*sn*-phosphatidylcholine

DOPS – 1,2-dioleoyl-*sn*-glycero-phosphatidylserine

DPPC – 1,2-dipalmitoyl-*sn*-phosphatidylcholine

ESP – electrostatic potential

FEP – Free Energy Perturbation

FF – force field

FFT – Fast Fourier Transform

GROMACS – GROningen MAchine for Chemical Simulations

HM-IE – Hybrid Methods for Interaction Energies

IPS – Isotropic Periodic Sum

ITC – isothermal titration calorimetry

LB – Lorentz-Berthelot

LBS – large basis set

L_d – liquid disordered

LJ – Lennard Jones

L_o – liquid ordered

LPS – liposaccharide

LRC – isotropic long-range correction

MD – molecular dynamics

MD – molecular dynamics

MP – Moller Plesset perturbation theory

NAMD – Nanoscale Molecular Dynamics

NMR – nuclear magnetic resonance

NPT – constant number, pressure, and temperature

NVT – constant number, volume, and temperature

PA – phophatidic acid

PC – phosphatidylcholine

PE - phosphatidylethanolamine

PEG – polyethylene glycol

PEG2 – diethylene glycol

PEG3 – triethylene glycol

PG – phosphatidylglyceride

PI – phosphatidylinositol

PLAPE – phosphatidylethanolamine plasmalogen

PME – particle mesh Ewald

POPC – 1-palmitoyl-2-oleoyl-*sn*-glycero-phosphatidylcholine

POPE – 1-palmitoyl-2-oleoyl-*sn*-glycero-phosphatidylethanolamine

PS – phosphatidylserine

QM – quantum mechanical

SANS – small angle neutron scattering

SANS – small angle neutron scattering

SAXS – small angle X-ray scattering

SBS – small basis set

SDP – scattering density profile

SM – sphingomyelin

VMD – Visualize Molecular Dynamics

Chapter 1. Introduction

1.1. Organization of this dissertation.

This dissertation is organized by topic and covers three main areas of research in lipid FF development: evaluation of the effects of long-range Lennard-Jones interactions on alkanes in additive and polarizable force fields (Chapter 2), modeling of ether-linked lipids and model linear ethers (Chapter 3), and improvement of lipid-ion interaction parameters (Chapter 4). The proceeding sections of Chapter 1 introduce lipids and lipid membranes (1.2), and lipid force field use and development (1.3).

Chapters include both previously-published material and new research. Previously-published sections are listed below with the corresponding publications.

Chapter 1: Introduction; Sections 1.2 – 1.3:

Leonard, A. N.; Wang, E.; Monje-Galvan, V.; Klauda, J. B. Developing and Testing of Lipid Force Fields with Applications to Modeling Cellular Membranes. *Chem. Rev.* **2019**.

Chapter 2: Evaluation of the effects of long-range Lennard-Jones interactions on alkanes

Leonard, A. N.; Simmonett, A. C.; Pickard, F. C. t.; Huang, J.; Venable, R. M.; Klauda, J. B.; Brooks, B. R.; Pastor, R. W. Comparison of Additive and Polarizable Models with Explicit Treatment of Long-Range Lennard-Jones Interactions Using Alkane Simulations. *J. Chem. Theory Comput.* **2018**.

Chapter 3: Parameterization of ether lipids and model linear ethers; Sections 3.1, 3.2, 3.3, and 3.5:

Leonard, A. N.; Pastor, R. W.; Klauda, J. B. Parameterization of the CHARMM All-Atom Force Field for Ether Lipids and Model Linear Ethers. *J. Phys. Chem. B.* **2018**, *122*, 6744 - 6754.

Chapter 4: Investigation of lipid-ion interactions; Sections 4.1, 4.2, 4.4, and 4.6:

Leonard, A.; Sukharev, S.; Klauda, J. B. Isothermal Titration Calorimetry of Be^{2+} with Phosphatidylserine Models Guides All-Atom Force Field Development for Lipid-Ion Interactions. *J. Phys. Chem. B.* **2019**, *123*(7), 1554 - 1565.

Section 3.4 describes the extension of ether linkage parameters to plasmalogens. Sections 4.3 and 4.5 contain preliminary results for the effects of KCl on conformation and R_g of 29-mer PEG.

Conclusions in Chapter 5 summarize the significance of these FF contributions and look to future applications.

1.2. Lipids and lipid membranes.

Phospholipids are the primary constituents of cell membranes. They are amphipathic with hydrophobic tails and a hydrophilic headgroup. This characteristic drives the spontaneous assembly of bilayers, monolayers, micelles, and liposomes, allowing the compartmentalization essential for chemically specific biological processes. Lipid species are widely diverse across organisms, varying in factors such as chain length, chain unsaturation, and headgroup. Common phospholipid headgroups include phosphatidycholine (PC), phosphatidylethanolamine (PE), phosphatidylserine (PS), phosphatidylinositol (PI), phosphatidic acid (PA), and phosphatidylglycerol (PG) (Figure 1). Of these, PC is the most abundant lipid, making PC membranes a topic of frequent

study, including a new model for an ether-linked PC lipid introduced in Chapter 3 of this dissertation. PE has a smaller headgroup than PC and possess an additional hydrogen bond donor. PI has a ring in the headgroup with varying phosphorylations that make these lipids useful in signaling processes.[1] The terminal carboxyl of PS gives it an overall negative charge. In mammalian cells, PS is more abundant in the inner leaflet of the cell membrane, but it flips to the outer leaflet to signal apoptosis. Ionic interactions involved in this signaling process are discussed in Chapter 4.

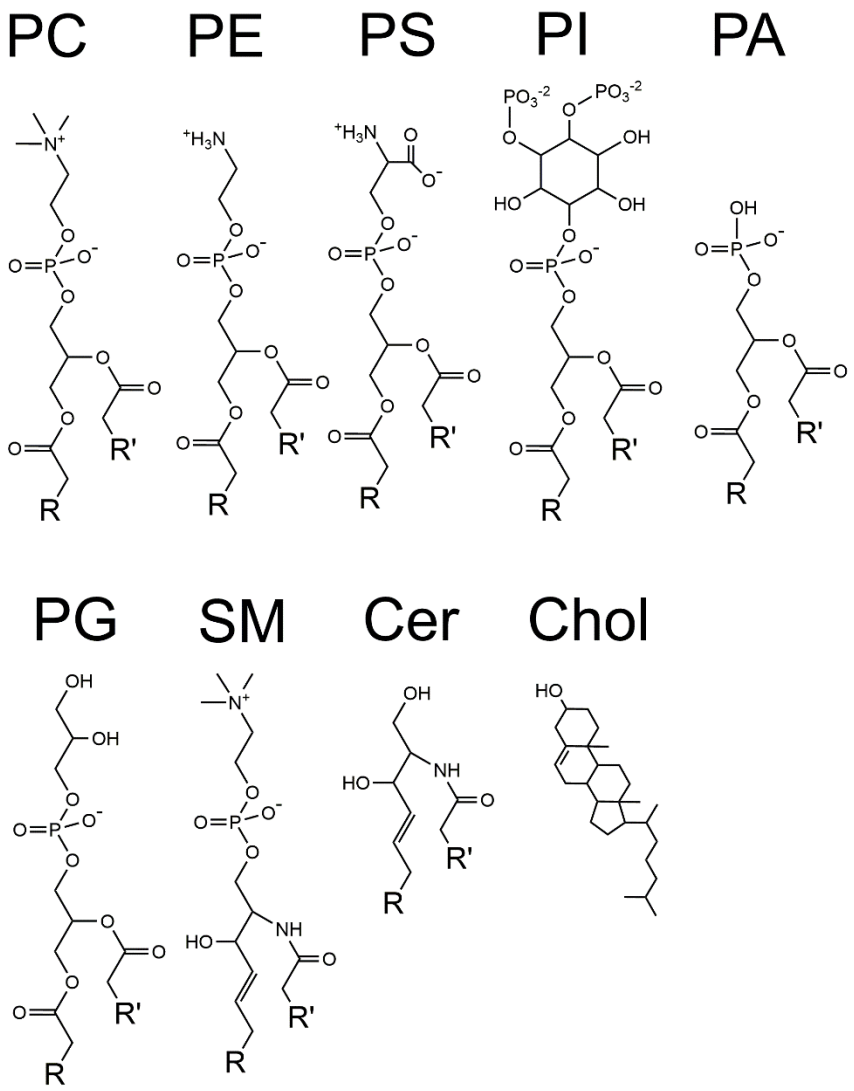

Figure 1. Chemical structures of phospholipid/sphingolipid headgroups and cholesterol. Headgroups represented are phosphatidylcholine (PC),

phosphatidylethanolamine (PE), phosphatidylserine (PS), phosphatidylinositol (PI), phosphatidic acid (PA), phosphatidylglycerol (PG), sphingomyelin (SM), and ceramide (Cer).

Another distinguishing characteristic of lipids is the length and degree of unsaturation of the hydrocarbon tails. Chain length and unsaturation affect the melting point of single-component bilayers—melting point increases as a function of chain length and decreases with degree of unsaturation.[2, 3] Melting point can be thought of as a measure of thermal order: the higher the melting point, the greater the tendency for order. We would expect bilayers rich in saturated lipids to exhibit more order. A common plumb line for lipid order is the acyl chain order parameter, S_{CD}, which is measured in solid state deuterium nuclear magnetic resonance (NMR) and can be calculated from simulation from the angle the C-D vector forms with respect to the bilayer's axis of orientation. Lower S_{CD} is correlated with less chain ordering with respect to the bilayer normal. Unsaturated chains exhibit lower S_{CD} than saturated chains; the acyl chain S_{CD} for the double-unsaturated *sn*-2 chain of 1-palmitoyl-2-isolinoleoyl-PC (PLPC; 16:0/18:2) are lower at each carbon position than DPPC at 40°C,[4, 5] with dramatic drop in S_{CD} seen at the positions of double bonds (acyl chain carbons C6-C7 and C9-C10 in the referenced study).

Lipid chain length and degree of unsaturation affect the mechanical properties of single-component bilayers and monolayers, including area per lipid (A_l), area compressibility modulus (K_A), and bending constant (K_C). Data for K_A for different lipid types is scant, and sampling different temperatures makes trends difficult to discern; however, one experimental study[6] determined that chain length and degree of unsaturation have little effect (<10%) on K_A of diacyl PCs with the number of double bonds varying from 1 – 6. The bending rigidity K_C increased with chain length from 0.56 x 10^{-19} J for

diC13:0 to 1.2 x 10^{-19} J for diC22:1, and dropped significantly when two or more double bonds were present (C18:0/2, diC18:2, diC18:3, diC20:4) to approximately 0.4 x 10^{-19} J. These data indicate that K_C increases with chain length and decreases with unsaturation.

Bilayer properties are also affected by headgroup structure, which contributes to monolayer or leaflet spontaneous curvature c_0. c_0 can be measured in monolayers that form the inverse hexagonal phase, but cannot be measured in bilayers because a symmetric bilayer will exhibit no net curvature. Monolayers of PE exhibit more negative curvature than their PC counterparts.[7] This means they curve about the headgroup region (Figure 2), which one would expect given the size difference between PE and PC (PC has a terminal choline group). While space-filling effects of headgroup and acyl chains are helpful in visualizing curvature, other factors such as hydrogen bonds and other electrostatic interactions also play a role.[8] Lastly, the linkage between the glycerol backbone and hydrophobic tails of phospholipids also affects mechanical properties; the ether-linked lipid di-hexadecyl-*sn*-glycero-phosphocholine (DHPC) has a higher A_l and lower water permeability than ester-linked DPPC at the same temperature. (Effects of the ether linkage are discussed in detail in Chapter 3.)

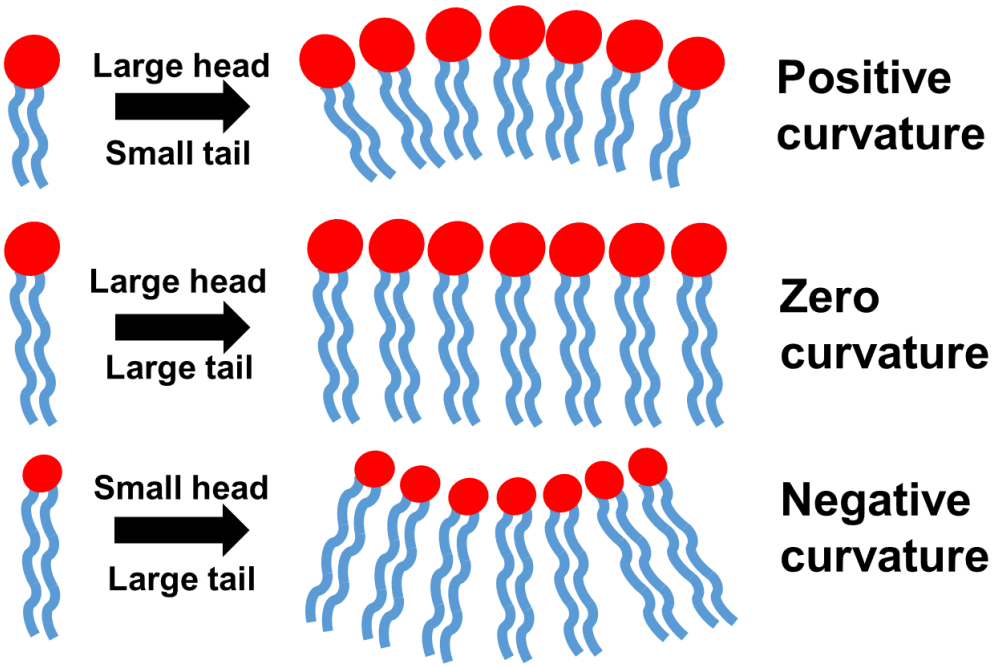

Figure 2. Influence of lipid structure on leaflet spontaneous curvature. (This simplified model does not address effects of molecular interactions.)

The mechanical properties discussed in the preceding paragraphs determine membrane thickness, its ability to compress and expand, and its propensity to curve. But such properties of single-component bilayers are of limited use in describing biological membranes. Discussion of a property as simple as the phase transition temperature of a mixed bilayer involves theoretical nuances when one considers phase separation, lipid clustering, and the existence of raft-like structures. The presence of cholesterol (Chol) and sphingomyelin (Figure 1) affect the order and thermodynamic properties of mixed bilayers. For example, a molecular dynamics (MD) study of DPPC/Chol mixed bilayers showed that Chol results in significant ordering of the DPPC chains, a reduced A_l, increased K_B, smaller K_A, and a reduced lateral diffusion of both DPPC and Chol.[9] It is hypothesized from experiments with detergent-resistant membranes that membrane domains high in both Chol and sphingomyelin exhibit the liquid ordered phase characterized by higher chain order

and packing density.[10] All-atom MD studies suggest this occurs through preferential hydrogen bonding between sphingomyelin and the rough face of Chol.[11]

In addition to ester-linked phospholipids with unbranched acyl chains, biological membranes include sterols, sphingolipids, liposaccharides, glycolipids, phospholipids with branched acyl chains, and phospholipids with at least one ether linkage between the glycerol backbone and acyl chain (ether lipids). Membrane lipid composition modulates the structure and mechanical properties of biological membranes,[12] and for this reason, composition varies among cell and organelle type and influences membrane function. For example, eukaryotic cells exhibit a 5-10-fold enrichment in cholesterol and sphingolipids in the plasma membrane relative to the endoplasmic reticulum;[13] this contributes to the relative rigidity of the plasma membrane. Phospholipids with at least one ether linkage between the glycerol backbone and an unsaturated acyl chain (plasmalogens) make up 18% of the total phospholipid mass in humans,[14] with elevated populations (52% of phospholipids) in nerve myelin,[15] and the effects these lipids have on membrane structure are not well characterized in current literature.

The outer and inner leaflets of the plasma membrane in eukaryotic cells are asymmetric in lipid composition,[16] with choline phospholipids (PC and sphingomyelin) preferring the outer leaflet and aminophospholipids (PE and PS) preferring the inner leaflet. The protein flippase or ATPas II translocates PE and PS from the outer to the inner leaflet against the electrochemical gradient.[17] Several structural proteins localize to the cytoplasmic side of the membrane through interaction with PS and contribute to membrane structure. Membrane translocation of specific phospholipids is involved in various

signaling pathways and plays a role in membrane restructuring events such as budding and endocytosis.

Lipids interact with membrane-bound proteins to affect protein structure and function. For example, membrane cholesterol has been shown to affect the structure and function of G-protein coupled receptors, the largest class of molecules involved in signal transduction across membranes.[18] Lipid composition also affects protein function indirectly through membrane mechanical properties.[19] The uneven distribution of lipids and membrane proteins gives rise to local curvature that serves to relax chemical stress. Local curvature in turn influences the function of embedded proteins.

Ion-lipid interactions affect membrane properties, structure and function of membrane-bound proteins, and signaling pathways. Positive ions interact with the polar headgroups of phospholipids. As a result, salt concentration has been shown to affect lipid phase transition temperature,[20] transmembrane potential,[21] and diffusion of water in the vicinity of lipid headgroups.[22] Specifically, Ca^{2+} associations with the phosphate oxygen of PS mediate recognition of PS by macrophages removing apoptotic cells in a non-inflammatory way, and toxic binding of Be^{2+} to PS in place of Ca^{2+} may inhibit this process.[23] Exploration of Be^{2+} interactions with PS can be found in Chapter 4.

1.3. Development of the CHARMM family of lipid force fields

1.3.1. Molecular dynamics simulations of lipids.

Molecular dynamics is a rapidly growing field enabling the description at the atomic scale. While a typical timestep in all-atom MD simulations is 1 or 2 fs, simulations of entire membrane-bound protein-ligand complexes in diverse bilayers have been extended to tens of microseconds. In protein-ligand simulations, such timescales enable the

identification of allosteric pathways[24] or, for those interested in lipid associations, identifying preferential binding sites for specific lipid types. In simulations of bilayers or fluids, long timescales are needed to characterize dynamic quantities such as diffusion.

The accuracy of data from MD simulations is determined by the FF used to model the system. With its amphipathic nature, the lipid molecule poses a parameterization challenge for chemically-specific FFs. Lipids self-assemble to form various structures depending on temperature and water concentration, e.g., micelles, bicelles, worm-like micelles, and bilayers.[25] Accurate balance is needed between the hydrophobic acyl chains and hydrophilic headgroups to allow for the assembly of these structures. The phase state of the lipid bilayer can also vary depending on conditions such as lipid composition. At physiological temperatures, bilayers without sterols typically exist in a fluid-like state known as the liquid-crystalline phase that contains disordered lipid acyl chains (mix of *trans* and *gauche* conformations).[13, 26] At low temperatures, a gel phase can form with ordered acyl chains (mainly in the *trans* conformation), forming a tilt angle with respect to the bilayer normal.[26] The introduction of sterols can alter phase behavior. Disordered acyl chains with cholesterol in the membrane are known as liquid disordered (L_d), but cholesterol can increase acyl chain order above the gel phase melting temperature and form ordered acyl chains with a phase called liquid-ordered (L_o).[13, 27] An accurate lipid FF must be able to capture the balance of these chemical-specific interactions to represent phase changes.

A molecular FF for lipids must be able to represent the internal molecular structure important for describing the bond distances, angles and dihedral states along with the intermolecular interactions. All-atom FFs, which represent each atom (including

hydrogens) as a specific interaction cite, provide the most chemical detail, but other less detailed models such as united atom (heavy atoms are parameterized to include effects of nonpolar hydrogens) and coarse grained (functional groups of various sizes are modeled as a single interaction cite), are also frequently used because they are less computationally expensive.

Molecular dynamics simulations can currently model a wide variety of lipids, including saturated and unsaturated hydrocarbon chains, PC, PE, PS, and PG headgroups, sphingomyelin (SM), ether and ester linkages between the glycerol backbone and tail, methylated tails, cyclopentene rings, and various sterols. Simulation studies commonly include membrane-bound proteins, peptides, ions, and water.

While mixed lipid bilayers more accurately model biological systems, simulations of single-component bilayers remain useful for FF validation. Such studies compare results from simulation with experimental data,[28] particularly order parameters obtained from NMR, or use single-component systems as initial tests for the development of new analyses such as lipid clustering,[29] permeability,[30] or curvature.[31] The permeability of water, ethanol, and small apolar molecules such as gases can be analyzed in unbiased MD simulations. Sampling the permeability of charged or large molecules requires long timescales or enhanced sampling methods.

Recent parameterization and development of commonly used lipid FFs aim to incorporate high lipid diversity and achieve long simulation trajectories, although these are computationally expensive. Efforts have been made to model diverse mixtures containing three or more components, and simulations have been extended into microsecond ranges, enabling the exploration of membrane dynamics.

1.3.2. The CHARMM family of force fields.

Research included in this dissertation focuses on the development of the CHARMM all-atom additive and CHARMM Drude polarizable FFs. An acronym for Chemistry at HARvard Macromolecular Mechanics, the CHARMM community actively develops a multifunctional simulation package[32, 33] that originated in the lab of Martin Karplus at Harvard University with a focus on proteins. This community has also developed a set of FFs for the standard building blocks in biology, i.e., lipids,[34] carbohydrates,[35-38] and nucleic acids,[39, 40] while continuing proteins.[41, 42]

The CHARMM family of lipid FFs includes all-atom and united-atom representation. In the united atom lipid FF, nonpolar hydrogens of lipid acyl chains are not independent interaction sites; instead, the nonbonded parameters of the parent atom are optimized to include the steric effect of hydrogens. Research in this dissertation focuses on the more chemically thorough all-atom FFs, in which hydrogens are explicitly modeled.

Various methods have been used to treat atomic polarizability in the CHARMM FFs over the years. The first method, developed by Patel and Brooks,[43-46] incorporated fluctuating charges. Due to computational expense, the classical Drude oscillator model was adapted by Roux and MacKerrell[47, 48] and is now the most commonly-used polarizability model in the CHARMM community. The Drude FF models each heavy atom as an oscillator in which a fixed net atomic charge is distributed between the two sites as a function of separation distance. This creates an atomic dipole moment capable of responding to the ambient electric and magnetic fields.

The remainder of this section will discuss the energy function and parameterization methods of the CHARMM all-atom lipid FF first, followed by additional terms for the Drude polarizable FF.

1.3.3. The CHARMM all-atom additive FF for lipids

In pairwise additive FF, the atomic charge distribution is assumed to be constant and therefore not influenced by environmental changes (such as local electric field). The potential is of the form:

$$U(r_1, r_2, \cdots, r_N) = \sum_{bonds} k_{b,ij}\left(r_{ij} - r_{0,ij}\right)^2 + \sum_{angles} k_{\theta,ijk}\left(f\left(\theta_{ijk}\right) - f\left(\theta_{0,ijk}\right)\right)^2 + \sum_{\substack{cross,\\ improper}} U_{cr,im}(r, \phi) + \sum_{dihedrals} U_{dih}\left(\varphi_{ijkl}\right) + \sum_{LJ} U_{LJ}\left(r_{ij}\right) + \sum_{electrostatic} \frac{q_i q_j}{4\pi\varepsilon_0 r_{ij}} \quad (1)$$

The first four terms in eq. (1) are bonded terms that describe internal degrees of freedom of neighboring molecules. These approximate the quantum mechanical (QM) description of shared electron orbitals that form chemical bonds. The *bonds* term in eq. (1) is a harmonic approximation of the bonded potential that describes the energy of stretching a bond from its equilibrium distance ($r_{0,ij}$). The angles term in eq. (1) describes the energy for scissoring the angle from its equilibrium value ($\theta_{0,ijk}$) and based triplicates of atoms connected by two bonds. For conditions typically observed in biological application, the harmonic approximation is valid as changes from the equilibrium distances are minimal

and these force fields are not reactive (no bond breaking or making). These two terms are obtained using experimental data on $r_{0,ij}$ and $\theta_{0,ijk}$ with their associated force constants from vibrational spectra, or if unknown, the use of QM to provide these values. The third term in eq. (1) (cross, improper) is added to provide proper description of: 1) out-of-plane orientations of an atom relative to a plane made by three other atoms (improper) and 2) 1-3 interactions between atoms that are not bonded but connected by two bonds (cross). The fourth term in eq. (1) is used to describe the dihedrals in a molecule and best represent torsional energies about a bond. The last two terms describe key non-bonded interactions that represent electrostatic (charge-charge) interactions and repulsion-attraction interactions with a Lennard-Jones (LJ) potential. The electrostatic term follows Coulomb's Law for charge-charge interaction with vacuum permittivity (ε_0). The charge is a partial charge to represent the QM description of charge distribution on atoms. To increase efficiency in computationally-expensive pairwise calculations for long-range electrostatics, the CHARMM additive FF treats the sum over electrostatic interactions with the particle-mesh Ewald (PME) method.[49] Within a supplied cutoff distance, interactions between each interaction site are summed directly. Outside the cutoff distance, interactions are approximated with a Fourier transform to provide the electrostatic contribution with no cutoff important for the slowly decaying inverse of distance. In the vicinity of the cutoff, the potential is modulated to maintain continuity.[49] The LJ term is used to represent both the repulsion (Pauli exclusion) and attraction (dispersion) felt between molecules. The CHARMM additive FF represents this with a 12-6 LJ potential with the attraction represented by a dipole-dipole dispersion term of $\mathrm{C}_{\mathrm{dis}} r^{-6}$, where C_{dis} is a constant. The repulsion term, which should theoretically be exponential, is represented by $C_{\mathrm{rep}} r^{-12}$

because this is just the square of the term used for the dispersion energy, thus simplifying the need to compute the exponential of a distance. Although this is an approximation, there is minimal loss of accuracy in biological applications that typically do not require an accurate description of unfavorable close contacts of atoms (only seen at very high pressures).

Historically, the FFs to describe proteins and nucleic acids were developed first as these were important targets to drugs and disease-associations. A preliminary lipid FF was tested in 1993 by Richard Pastor and Rick Venable at the 100-ps timescale,[50] followed shortly by the initial CHARMM22 (C22) lipid parameter set[51, 52] and subsequently by CHARMM27 (C27), the first widely-used all-atom lipid FF.[53] As with all FF families, parameterization is tied to a water model, and the CHARMM pairwise additive FF used the modified TIP3P water model.[54, 55] It is not recommended that other water models be used even though these might have superior properties due to issues of charge balance and free energies of solvation that would change.

These initial developments of the lipid FF followed the standard approach in CHARMM to develop FF parameters. The ultimate goal is to use small molecule representations of portions of the lipid molecule (alkanes for the acyl chain, for example) to develop parameters that are transferable to all lipids. The internal degrees of freedom (bond, angle, cross and improper) in eq. (1) were fit to reproduce experimental and *ab initio* results on geometries and vibrational spectra.

The parameterization of the non-bonded and dihedral terms in C27 followed the standard supramolecular approach used in CHARMM.[56-58] Structure, electrostatics and energies between select model compounds with water or noble gasses are calculated with

ab initio QM. Partial charges are obtained on the lipid model compounds based on reproducing minimum interaction energies with water. Then, LJ parameters ($r_i^{\min}$ and ε_i) using the standard functional form in CHARMM are fit based on interactions of these lipid model compounds with neon or helium:

$$\sum_{LJ} U_{LJ}(r_{ij}) = \sum_{\substack{\text{non-bonded} \\ \text{pairs}}} \varepsilon_{ij} \left[\left(\frac{r_{ij}^{\min}}{r_{ij}} \right)^{12} - 2 \left(\frac{r_{ij}^{\min}}{r_{ij}} \right)^{6} \right] \quad (2)$$

The lipid FF was parameterized using force-based cutoffs in which the force is smoothed to zero at the cutoff of 12 Å. Although the LJ forces are zero at the cutoff, the cutoff scheme also influences and changes the overall potential and thus lipid simulations must use this force-based cutoff scheme to conform to the way the CHARMM FF was developed.

Non-bonded pairs for LJ and electrostatics are considered for 1-4 interactions without scaling. Consequently, the dihedral potential parameters will depend on the LJ and electrostatic parameters. Optimization of these coupled parameters typically follows an iterative fashion (obtain LJ/electrostatics, fit dihedrals, and repeat). The dihedral potential is a sum over cosine terms:

$$\sum_{dihedrals} U_{dih}(\varphi_{ijkl}) = \sum_{dihedrals} \sum_{\forall n} k_{\varphi,n} \left(1 + cos(n\varphi_{ijkl} - \delta_n) \right) \quad (3)$$

The minimal amount of dihedral terms is selected to best match torsional energies calculated from QM. The force constant $k_{\varphi,n}$ depends on the periodicity *n*, which takes values from 1 to 6.

The most recent comprehensive CHARMM lipid FF is CHARMM36 (C36),[34, 59] which solved a problem with previous versions of the FF; the surface tension for a symmetric bilayer should sum to zero at the natural lipid packing condition. By accurately representing this property, C36 enabled bilayer simulations to be run in the constant number, pressure, and temperature (NPT) ensemble without need of an applied surface

tension. Initial development of C36 focused on common lipids with ample experimental data such as DPPC, 1-palmitoyl-2-oleoylphosphatidylcholin (POPC), 1,2-dimyristoyl-*sn*-phosphatidylcholine (DMPC), 1,2-dilauroyl-*sn*-phosphatidylcholine (DLPC), 1,2dioleoyl-*sn*-phosphatidylcholine (DOPC), and 1-palmitoyl-2-oleoyl-*sn*-phosphatidylethanolamine (POPE). Additional common headgroups were added: PA, PG, PI and PS.[29, 60, 61] Glycolipids (important in nerve membranes) and lipopolysaccharides (LPS) have also been developed and tested[61-64] using the existing CHARMM carbohydrate FF.[35-38] Sphingolipids and ceramides have also been incorporated into the C36 lipid FF for added diversity of lipid headgroups in CHARMM.[31, 65] Aside from the lipid headgroup, work has also be focused on the varying acyl chains, i.e., polyunsaturated,[66] branched,[67] and cyclic-containing (important in certain bacteria membranes),[68] and varying sterols (cholesterol,[69] ergosterol,[70] and plant sterols[71]), and modeling of the glycerol-ether linkage[72] (see Chapter 3).

1.3.4. The CHARMM Drude polarizable FF for lipids.

The assumption of constant atomic charge held by pairwise additive FFs distorts interactions between polar and nonpolar species. This is clearly illustrated by calculation of the dielectric constant (ε). Accounting for atomic polarizability is known to affect dipole potentials[73] and dielectric constants (ϵ).[74] For example, ϵ of decane in CHARMM27r[59] (the precursor to C36) is 1.02, approximately half the experimental value of 1.97.[74] The value of ϵ for decane in the CHARMM Drude FF is 2.06,[47] in near-perfect agreement with experiment. Because free energy of solvation scales with $(1 - 1/\epsilon)$, improvement of this quantity should give better energetics of transfer between polar and nonpolar media.

To resolve this issue, there have been varying approaches to account for atomic polarizability and better represent the effect of local environment on molecular electrostatics. CHARMM typically treats atomic polarizability with the classical Drude oscillator model.[73, 75, 76] The Drude FF uses a virtual particle, i.e., the Drude particle, that has a charge $q_{D,i}$ and is connected to a polarizable atom i with a harmonic force constant k_D. This allows the use of eq. (1) with additional terms to describe the energy associated with the Drude particle:[74]

$$U_{\text{Drude}}(r_1, \cdots, r_N, r_{D1}, \cdots, r_{Dn}) = \frac{1}{4\pi\varepsilon_0}\left(\sum_{i<j}\frac{q_{D,i}q_j}{\|r_{Di}-r_j\|} + \sum_{i<j}\frac{q_{D,i}q_{D,j}}{\|r_{Di}-r_{Dj}\|}\right) + \frac{1}{2}\sum_{\substack{\text{polarizable}\\ \text{atoms i}}} k_D\|r_{Di}-r_i\|^2 \quad (4)$$

The position of the Drude particle r_{Di} is allowed to fluctuate due to the variation of the electrostatic environment and thus represents the response of the electron cloud to its local environment. The charge on the Drude particle is represented by its polarizability α_i with $q_{D,i} = \sqrt{k_D\alpha_i}$. The Drude particles have a small mass (0.4 amu) taken from the attached real atom.[75, 77] In this approach, the simulation proceeds much like a classical pairwise additive MD simulation with an additional Drude particle on non-hydrogen atoms. The additional Drude particles and the need for a 1fs timestep (vs. 2fs) makes this slower than a pairwise additive FF but faster than fluctuating charge approaches.

In the initial parameterization effort by Anizimov et al.,[48] which included nucleic acid components, reference values for atomic polarizabilities (α) were based on Miller's atomic hybrid polarizability values.[78] Determination of α_i can be reduced to the determination of the partial charges of Drude particles, $q_{D,i}$, which were assigned with restrained fitting to quantum mechanical electrostatic potentials (ESP). Drude was

subsequently parameterized to include alkanes,[74] alcohols,[79] aromatic compounds,[80] ethers,[81, 82] nitrogen-containing heteroaromatic compounds,[83] lipids,[73, 75, 76] proteins,[84] and DNA.[85]

A Thole damping constant[86] was implemented to explicitly include dipole-dipole interactions for atoms within three bonds.[74] In additive FFs, interactions for 1-2 and 1-3 pairs are typically subsumed by the bonded potential energy function and excluded from the electrostatic energy. While electrostatic interactions of Drude oscillators with core charges are excluded for 1-2 and 1-3 atom pairs, Coulomb interactions between Drude oscillators (i.e., dipole-dipole interactions) corresponding to 1-2 and 1-3 atom pairs are included but shielded by a damping function. The magnitude of this shielding is governed by the Thole damping constant, which can now be calculated from parameter assignments for individual atoms.[87]

In addition to inclusion of dipole-dipole interactions, the Drude FF has a second inherent advantage over C36: It uses the polarizable SWM4-NDP water model, optimized for negatively charged Drude particles.[88] Relative to TIP3P used with C36, SWM4-NDP shows better agreement with experimental properties of bulk water including vaporization enthalpy, translational diffusion, shear viscosity, and surface tension at the air/water interface. However, it should be noted that SWM4-NDP was optimized near biological temperature and can result in reduced accuracy (water density and likely other properties) outside 290-310K.[89]

Until recently, the Drude FF was parameterized for only a single lipid: the saturated lipid DPPC.[73] Parameters were first obtained for model compounds including alkanes, dimethylphosphate, tetramethylammonium, and various esters. Partial charges and atomic

polarizabilities were fit as previously described. LJ parameters were selected to reproduce both QM gas phase interaction energies and liquid molecular volumes. Bonded term force constants were optimized against QM calculations of the vibrational spectra. Lastly, dihedral parameters were optimized against one-dimensional relaxed potential energy scans as well as rotamer energies to balance the local and global QM target data.

A recent parameterization effort by Li et al.[76] improved agreement with structural data for a DPPC bilayer and expanded the Drude FF, adding seven lipid types including saturated and unsaturated forms of PC and PE. The authors began by adjusting parameters for seven torsions located in the polar head and glycerol backbone region to bring G3S and G2 deuterium order parameters of DPPC in closer agreement with experiment than their first effort.[73] This was achieved, and A_l of DPPC was also improved. However, the new FF still underestimates A_l for all PC lipids (except DMPC) by an average of 2.3 $Å^2$/lipid. Additionally, bilayer area compressibility moduli are substantially overestimated, and the lipid self-diffusion coefficient of DPPC is too low by nearly a factor of 10.

Chapter 2. Comparison of Additive and Polarizable Models with Explicit Treatment of Long-Range Lennard-Jones Interactions in Alkane Simulations.

2.1. Introduction

The C36 additive FF for lipids has been widely used for MD simulations of pure and complex lipid bilayers since its publication in 2010. It has been extended from the original set of six lipids (five phosphatidylcholines and one phosphatidylethanolamine) to sphingolipids,[31] polyunsaturated lipids,[66] glycolipids,[64] and lipopolysaccharides.[61] While the initial validation of the FF was primarily based on bilayer surface areas and densities (from X-ray and neutron diffraction data), and chain order and dynamics (from deuterium and ^{13}C NMR data), subsequent comparisons with experiment for headgroup order parameters,[90, 91] bending constants, and spontaneous curvatures[7, 92] have been very positive. The FF has also been tested with lipid mixtures containing cholesterol with glycerophospholipids and/or sphingolipids, and agrees with X-ray form factors and NMR order parameters.[27-29, 68] This has allowed for accurate interpretations of liquid ordered/disordered phases of lipid mixtures[93] and lipid composition effects on hydrogen bonding and lipid clustering.[94, 95] Although simulations with the C36 lipid FF have been successful, the FF does have inherent flaws. It was appreciated at the time of publication that the surface tensions for bilayers and monolayers are inconsistent with experiment, and that the dipole potential is too large.[34] More recently, after taking periodic boundary conditions into account,[96] it has been demonstrated that diffusion constants are overestimated by a factor of 3 for at least two lipids.[97]

The C36 lipid FF (and other additive lipid FFs[98, 99]) has two attested shortcomings: it was parameterized without accounting for long-range Lennard-Jones (LJ) interactions

for most parameters,[100] and it is not polarizable. Polarizability is known to affect dipole potentials[73] and dielectric constants (ϵ).[74] For example, ϵ of decane in CHARMM27r[59] (C27r; the precursor to C36) is 1.02, approximately half the experimental value of 1.97.[74] This underestimation of ϵ increases the interaction of charges on opposite sides of the bilayer. The natural solution here is to use a polarizable FF.

The CHARMM Drude FF accounts for atomic polarizability by implementing the classical Drude oscillator model.[47] The value of ϵ for decane in the Drude FF is 2.06, in near-perfect agreement with experiment. Because free energy of solvation scales with $(1 - 1/\epsilon)$, improvement of this quantity should give better energetics of transfer between polar and nonpolar media. However, like C36, most of the Drude lipid FF was originally parameterized without inclusion of long-range LJ interactions.[34, 73] The lack of long-range LJ interactions is related to the difficulties of reproducing monolayer surface tensions, given the importance of these terms for alkane/air interfaces.[101]

This chapter sets the groundwork for a reparameterization of the C36 and Drude lipid FFs with explicit inclusion of long-range LJ interactions. Following the strategy used for the development of C36, alkanes, the principal component of saturated lipid chains, are considered first.[59] The main focus is on including the long-range LJ terms in a computationally efficient manner that is applicable anisotropic systems. This has proven to be difficult because most methods for including long-range LJ terms are only applicable to isotropic systems.[102, 103] Fortunately, recent work has refined the particle-mesh Ewald (PME) method for Lennard-Jones interactions.[104] Lennard-Jones PME (LJ-PME) can be used with bilayers, monolayers, and other anisotropic systems in both constant pressure and constant volume ensembles. The implementation of LJ-PME utilized here involves the

calculation of LJ interaction coefficients using geometric combining rules. It can be used in tandem with electrostatic PME, lowering the direct-space cutoff (r_{cut}) necessary for accurate calculations and computational efficiency. This paper introduces the implementation of LJ-PME in CHARMM and explores its effects on equilibrium and transport properties of alkanes in the condensed phase.

Section 2.2 provides simulation specifications and describes the implementation of LJ-PME in CHARMM. Section 2.3 presents simulation results. Section 2.4 discusses the effects of LJ-PME and evaluates trends in the temperature dependence of thermodynamic properties.

2.2. Methods

2.2.1. Molecular dynamics simulations and parameters.

Simulations were run using four distinct force fields: C36 without a correction for long-range LJ interactions, C36 with LJ-PME (denoted C36/LJ-PME), Drude without a correction, and Drude with LJ-PME (Drude/LJ-PME).

All simulations were performed in CHARMM.[33] The Nosé-Hoover thermostat[105] was used to maintain system temperature, and a modified Andersen-Hoover barostat to maintain constant pressure.[106, 107] A thermostat coupling constant of 2000 kcal/mole-ps^2 and a piston mass of 1200 amu were used to maintain NPT ensemble. All simulations were performed using periodic boundary conditions and SHAKE algorithm to constrain covalent bonds involving hydrogens.[108] Long-range electrostatic interactions were evaluated using PME[109] with a cutoff for real-space calculations $r_{\mathrm{cut}} = 12$ Å when LJ-PME was not used and $r_{\mathrm{cut}} = 10$ Å with use of LJ-PME, except where dependence on r_{cut} was evaluated.

Sec. 2.6 provides the details on the real-space cutoff scheme for the LJ portion of the FF. The standard errors *(se)* were estimated as the standard deviation (σ_B) in block averages divided by the square root of the number of blocks (n_B):

$$se = (1/\sqrt{n_B})\sigma_B \quad (5)$$

Quantities calculated from simulations were: density (ρ), isothermal compressibility (β_T), viscosity (η), surface tension (γ), translational diffusion constant (D), Nuclear Magnetic Resonance (NMR) C^{13} spin-lattice relaxation time (T_1), coefficient of thermal expansion (a_V), and radial distribution function ($g(r)$). Simulations were performed using each FF for each set of simulation specifications in

Table ***1*** using a 1-fs timestep. A separate set of simulations were used to examine the dependence of ρ and γ on r_{cut}. In these simulations, 64 molecules of $C_{16}H_{34}$ were simulated at 298.15 K for 10 ns using a 2-fs timestep in the NPT ensemble to calculate ρ, and in the NVT ensemble to calculate γ.

For simulations used to calculate η, γ, and D, initial coordinates were obtained from the equilibrated NPT simulations used to determine ρ. A coordinate set representing the average ρ of each simulation was used to start a simulation in the NVT ensemble. Systems for the surface tension simulations consisted of an alkane slab surrounded by vacuum layers, as described previously,[101] with the *x* and *y* dimensions matching the equilibrated box size from the NPT simulations used to calculate ρ and the *z* dimension (normal to the surface) elongated. For example, for hexadecane at 303.15 K in the Drude FF, the dimensions of the box were 50.1197 Å × 50.1197 Å × 100 Å.

Table 1. Simulations of alkanes. Species, temperatures (T), number and length of runs (t_{run}), ensembles, and quantities evaluated. For each set of specifications, simulations of 256 molecules were performed using C36 and Drude with and without LJ-PME.

Species	T (K)	t_{run} (ns)	Ensemble	Use
$C_{16}H_{34}$	303.15, 310.15, 323.15, 393.15	1 × 30	NPT	ρ, β_T, α_V, $g(r)$
$C_{16}H_{34}$	303.15, 310.15, 323.15; 323.15	3 × 100 (C36) 2 × 100 (Drude)	NVT	η; D
$C_{16}H_{34}$	303.15, 310.15, 323.15	1 × 50	NVT	γ
$C_{15}H_{32}$	312.15	2 × 30	NPT	T_1
C_7H_{16}	312.15	2 × 30	NPT	T_1

This paper uses standard alkane parameters in C36[34] and Drude.[74] There have been several adjustments to the alkane torsional parameters since publication of C27r.[66] Table 2 lists the parameters used here to avoid confusion. The form of the CHARMM torsion potential, where φ is the dihedral angle, is given in eq. (3), Sec. 1.3.3.

Table 2. Torsional parameters for alkanes.

Term	Drude			C36 Lipid FF[34]		
	k_φ	N	Δ	k_φ	n	δ
CH₃-CH₂-CH₂-CH₃	0.150	1	0	0.060	2	0
	0.170	2	0	0.035	5	0
	0.114	3	0			
	0.094	4	0			
	0.070	5	0			
CH₃-CH₂-CH₂-CH₂	0.093	1	0	0.162	2	0
	0.143	2	0	0.047	3	180
	0.055	4	0	0.105	4	0
	0.102	5	0	0.177	5	0
CH₂-CH₂-CH₂-CH₂	0.073	1	0	0.101	2	0
	0.043	2	0	0.142	3	180
	0.119	3	180	0.074	4	0
	0.098	4	0	0.097	5	0
	0.046	5	0			

2.2.2. Analysis of MD trajectories.

Density was determined by averaging the volume of the simulation box after equilibration. Isothermal compressibility β_T was evaluated from

$$\beta_T = \frac{\langle \delta V^2 \rangle}{\langle V \rangle k_B T}, \tag{6}$$

where k_B is Boltzmann's constant, $\langle V \rangle$ is the average volume, $\langle \delta V^2 \rangle$ is the fluctuation in volume, and T is the temperature.[102]

Shear viscosity was evaluated using the Green-Kubo formula:[102]

$$\eta = \frac{V}{k_B T} \int_0^\infty \langle P_{\alpha\beta}(t) P_{\alpha\beta}(0) \rangle dt, \tag{7}$$

where $P_{\alpha\beta}$ are the off-diagonal elements of the pressure tensor, and V is the volume of the simulation box. The pressure tensor was assumed to be symmetric ($P_{\alpha\beta} = P_{\beta\alpha}$). CHARMM[33] was used to compute the correlation function of the three unique off-diagonal elements, average them, and sum the integral.

The surface tensions of the alkane-vacuum interfaces were evaluated from:

$$\gamma = 0.5 \langle L_z \left[P_{zz} - 0.5 \left(P_{xx} + P_{yy} \right) \right] \rangle, \tag{8}$$

where L_z is the size of the simulation box normal to the interface,[110] P_{zz} is the normal component of the internal pressure tensor, and P_{xx} and P_{yy} are the tangential components. A prefactor of 0.5 accounts for the fact that the systems contained two interfaces.

Translational diffusion constants were obtained from the Einstein relation $\langle r^2 \rangle = 6Dt$, where r is the displacement of a molecule at time t. The Yeh and Hummer[111] correction was used to account for periodic boundary conditions:

$$D^\infty = D^{PBC} + \frac{k_B T \xi}{6\pi\eta L}, \tag{9}$$

where D^{PBC} is the diffusion constant measured from simulation, L is the box length, ξ = 2.837297, η is the viscosity of the fluid, and D^{∞} is the infinite system result.

NMR spin-lattice relaxation times T_1 were calculated using the standard formula for dipolar relaxation from the reorientational correlation function of the CH vectors in the motional narrowing limit:[112]

$$\frac{1}{NT_1} = (1.855 \times 10^{10} s^{-2}) \int_0^{\infty} \langle P_2\big(\hat{\mu}(0)\big)\big(\hat{\mu}(t)\big)\rangle dt, \quad (10)$$

where N is the number of protons bonded to the carbon, $\hat{\mu}$ is the CH vector, and the constant preceding the integral contains an effective CH bond length of 1.117 Å.[113]

2.2.3. Analysis of temperature dependence.

The volumetric coefficient of thermal expansion (α_V) describes the dependence of volume, and therefore also of density, on temperature at constant pressure:

$$\alpha_V = \frac{1}{V}\left(\frac{\partial V}{\partial T}\right)_p. \quad (11)$$

The same trajectories used to determine ρ were used to calculate α_V at 313.15 K and to compare with the experimental value of molar volume (V_{mol}) at that temperature. A linear dependence of V_{mol} on temperature was assumed.

To find the functional form of the temperature dependence of β_T, chi-squared statistical values were calculated for regressions of the form $a + bT^c$, with values of 1/3, 1/2, 1, 2, 3, 4, and 5 for c. The χ^2 statistic is given by:

$$\chi^2 = \sum_{i=1}^{N} \frac{1}{E_i}(O_i - E_i)^2, \quad (12)$$

where N is the number of data points in the sample, O_i is the value of the i^{th} sample, and E_i is the value predicted by the distribution. Values of χ^2/N were minimized to determine c.

2.2.4. Implementation of LJ-PME in CHARMM.

The contributions of long-range dispersion to the energy and pressure that are neglected by cutoff methods were historically accounted for by various correction terms. A popular correction, the isotropic long-range correction (LRC),[102] is derived by assuming that the radial distribution function $g(r)$ is unity beyond r_{cut}. The isotropic LRC is usually satisfactory for bulk fluids of small molecules, but fails when anisotropy is significant, as is the case for lipid bilayers and other interfacial systems. The pressure-based LRC,[103] where LJ interactions outside r_{cut} are approximated with the application of an additional pressure which is periodically calculated from the difference of the instantaneous pressures at the selected r_{cut} and a very long r_{cut}, is applicable to larger molecules, but not to interfaces. CHARMM also supports the IPS (Isotropic Periodic Sum) method[114] to approximate long-range LJ interactions. This method defines a local region for each particle, and sums the remaining region (including images) as an integral of virtual images of the local region statistically distributed in an isotropic and periodic manner. The version denoted 3D-IPS is not applicable to interfacial systems. 2D-IPS and the more computationally efficient 3D-IPS/DFFT[115] do accurately model interfaces.[101, 116] The IPS methods have not been widely implemented because of assumptions of homogeneity.

The preceding methods are all available in CHARMM. Others[117-119] have proposed a slab-based correction to specifically address inhomogeneity at interfaces. This method approximates long-range LJ forces with an additive force contribution in the direction perpendicular to the interface. The added force is a function of the density of an isotropic slice within the simulation box. Janeck[118] shows accurate treatment of surface tensions for Lennard-Jones fluids with an adaptation of this slab-based method.

As is well known, long-range electrostatic forces can be evaluated explicitly and with high computational efficiency, thereby eliminating the need to truncate interactions using a cutoff. The use of cutoffs leads to substantial artifacts for electrostatics,[120] and the PME[49] method is widely used for this reason. The PME approach for dispersion has its origins in the 1957 work of Nijboer and de Wette,[121] who generalized the Coulomb operator partitioning to faster decaying interactions. Williams used this generalized partitioning in 1971 to develop an Ewald-like treatment of dispersion interactions,[122] which was later expanded by Karasawa and Goddard to include energy derivatives.[123] Though in 1995 Pedersen and coworkers demonstrated a modification of Ewald dispersion to use the highly efficient PME methodology,[109] the use of a cutoff on the Lennard-Jones attractive (r^{-6}) term has persisted. Recently, a number of workers[124-127] have increased the computational efficiency of the PME method for r^{-6} potentials, and the method is being incorporated into popular simulation programs.[104] The repulsive potential term decays much more quickly and is therefore neglected at long range by simply truncating the interaction past r_{cut}. Hence, the name of the method, "LJ-PME," should not be understood to correct the entire LJ potential.

For the r^{-6} kernel, the Ewald partitioning of the summation over unit cells **n** can be expressed as:

$$E_6 = -2\sum_{\mathbf{n},i,j}\sqrt{\varepsilon_i\varepsilon_j}\frac{{r_i^{\min}}^3{r_j^{\min}}^3}{r_{ij}^6} = -2\sum_{\mathbf{n},i,j}\sqrt{\varepsilon_i\varepsilon_j}\frac{{r_i^{\min}}^3{r_j^{\min}}^3 f\left(\kappa r_{ij}\right)}{r_{ij}^6}$$

$$-2\sum_{\mathbf{n},i,j}\sqrt{\varepsilon_i\varepsilon_j}\frac{{r_i^{\min}}^3{r_j^{\min}}^3[1-f(\kappa r_{ij})]}{r_{ij}^6}, \qquad (13)$$

where we assume geometric mean combination rules:

$$\varepsilon_{ij} = \sqrt{\varepsilon_i \varepsilon_j};\ \ \mathrm{r}_{ij}^{\min} = \sqrt{\mathrm{r}_i^{\min} \mathrm{r}_j^{\min}} \tag{14}$$

and introduce the shorthand notation $r_{ij} = \left|\mathbf{r}_{ij} + \mathbf{n}\right|$ in addition to the screening function $f(x) = e^{-x^2}(1 + x^2 + x^4/2)$, which depends on the attenuation parameter κ (we avoid the often-used β for this quantity to disambiguate it from the isothermal compressibility). The decomposition of the lattice sum yields two terms. The first is short-ranged and rapidly convergent in a standard pairwise summation, while the second long-range, nonsingular term converges rapidly in reciprocal space and can be treated using Fast Fourier Transforms (FFTs). The attenuation parameter determines the relative computational efforts in real and reciprocal space. For suitably chosen r_{cut} and FFT grids, the answer is independent of κ, which is chosen to minimize computational cost with the pairwise r_{cut} adjusted accordingly.

The multiplicatively separable form assumed above is important for the PME treatment of the long-range term, which proceeds by first discretizing the density due to all particles on a grid, transforming the density to a potential via FFTs, and then probing the potential grid at each atomic center to yield the energy and forces. However, the CHARMM FFs use the Lorentz-Berthelot (LB) combination rule, which defines off-diagonal hard sphere radii in a form incongruous with the multiplicatively separable form described above:

$$r_{ij}^{\min} = \frac{r_i^{\min} + r_j^{\min}}{2}. \tag{15}$$

One potential remedy for this situation is to express the interaction coefficient using a binomial expansion:

$$\left(r_i^{\min} + r_j^{\min}\right)^6 = \sum_{n=0}^{6} \binom{6}{n} {r_i^{\min}}^n {r_j^{\min}}^{6-n}. \quad (16)$$

This expansion transforms E_6 in eq. (13) to a sum of seven terms possessing the requisite separable form. The need for multiple FFTs is avoided using the strategy developed by Wennberg *et al*.[104] Briefly, their approach proceeds by a subtle change to the partitioning introduced above:

$$E_6 = -2 \sum_{\mathbf{n},i,j} \sqrt{\varepsilon_i \varepsilon_j} \frac{\left(r_i^{\min} + r_j^{\min}\right)^6}{64 r_{ij}^6} = -2 \sum_{\mathbf{n},i,j} \sqrt{\varepsilon_i \varepsilon_j} \left[\frac{\left(r_i^{\min} + r_j^{\min}\right)^6}{64 r_{ij}^6} - \frac{{r_i^{\min}}^6 {r_j^{\min}}^6 [1 - f(\kappa\, r_{ij})]}{r_{ij}^6} \right] - 2 \sum_{\mathbf{n},i,j} \sqrt{\varepsilon_i \varepsilon_j} \frac{{r_i^{\min}}^6 {r_j^{\min}}^6 [1 - f(\kappa\, r_{ij})]}{r_{ij}^6}. \quad (17)$$

Again, the first term on the righthand side is treated in real space and the second term in Fourier space. The net effect is that a multiplicatively separable form is used to determine the long-range correction in Fourier space. This approach is also compatible with pair-specific LJ parameters (NBFIX terms) that are often used in FFs, with $r_i^{\min} + r_j^{\min}$ in eq. (17) replaced by the corresponding NBFIX parameters.

In real space, the exact functional form of the potential is used up to r_{cut}, and another term is present to partially account for spurious short-range multiplicatively separable terms introduced in reciprocal space. This scheme is no longer rigorously insensitive to the choice of r_{cut}, but the difference between the two sets of combination rules is small enough at long range that this is a very good approximation. A discontinuity in the potential energy is averted at r_{cut} by applying a shift to account for the difference between the treatments at short and long range:

$$E_{\text{shift}} = -2 \sum_{\mathbf{n},i,j} \sqrt{\varepsilon_i \varepsilon_j} \left(\frac{\left(\frac{r_i^{\min} + r_j^{\min}}{2}\right)^{12}}{r_{\text{cut}}^{12}} + \frac{{r_i^{\min}}^3 {r_j^{\min}}^3 [1 - f(\kappa\, r_{\text{cut}})] - \left(\frac{r_i^{\min} + r_j^{\min}}{2}\right)^6}{r_{\text{cut}}^6} \right). \quad (18)$$

In eq. (18), the first term cancels the repulsive part of the LJ potential at r_{cut}, while the second term ensures a smooth transition from the real-space treatment to the multiplicatively separable regime. Although this correction guarantees a smooth potential, there may still be discontinuities in the forces. Differentiation of eq. (18) yields

$$F_{\text{shift}} = 4 \sum_{\mathbf{n},i,j} \sqrt{\varepsilon_i \varepsilon_j} \left(12 \frac{\left(\frac{r_i^{\min} + r_j^{\min}}{2} \right)^{12}}{r_{\text{cut}}^{13}} + 6 \frac{{r_i^{\min}}^3 {r_j^{\min}}^3 [1 - f'(\kappa\, r_{\text{cut}})] - \left(\frac{r_i^{\min} + r_j^{\min}}{2} \right)^6}{r_{\text{cut}}^7} \right), \qquad (19)$$

where $f'(x) = e^{-x^2}(1 + x^2 + x^4/2 + x^6/6)$. eq. (19) quantifies the force discontinuity due to the truncation of the repulsive term and the handoff between the two combination rules; the logarithm of the absolute value of this quantity is displayed in Figure 3, for selected pairs of atom types, as a function of κ and r_{cut}.

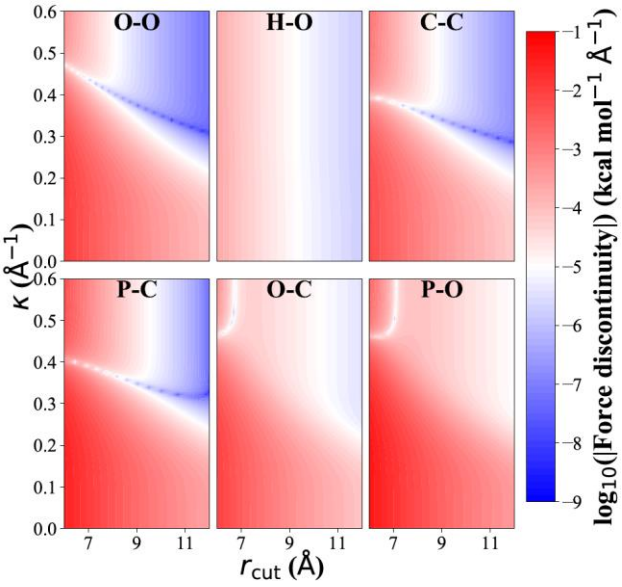

Figure 3. Force discontinuities when potential shifting is used. The logarithm of the magnitude of the force discontinuities present when only potential shifting is used to smooth the potential, as a function of κ and r_{cut}. Parameters for various atom types are taken from the C36 lipid FF.

As expected, the lowest discontinuity error occurs where κ is large, *i.e.*, there are long-range terms present to account for the truncation of the attractive LJ term, and also

where r_{cut} is large. Assuming a typical force on each atom to be ~10 kcal/mol/Å, the white contour lines in Figure 3 represent an error in the contribution to the forces of about 1 part per million, which will be incurred every time a pairwise interaction crosses r_{cut}. To further quantify the consequences of the force discontinuities, NVE simulations were carried out on n-hexadecane and neat water, demonstrating that the energy drift is within 0.2 kcal/mol/ns, even with r_{cut} as low as 7 Å; the supporting information contains full details of these tests. Because the microcanonical ensemble is maintained so well, a correction for the force discontinuity is not included in the current CHARMM implementation; there is an option to use potential switching[128] for ensuring continuous energies and gradients in free energy calculations.

Finally, the instantaneous virial stress tensor is required to generate constant pressure ensembles. The real-space contribution is exactly analogous to the standard outer-product form, involving forces and positions, that is used to evaluate the LJ virial. The reciprocal-space tensor is obtained by summation over reciprocal space lattice vectors **m**, with norm m,

$$\Pi_{\alpha\beta} = \frac{\pi^{3/2}}{6V}\sum_{\mathbf{m}} e^{-\frac{\pi^2 m^2}{\kappa^2}} \left(\begin{array}{c} 3\pi^2 \left(\pi^{3/2} m e^{\frac{\pi^2 m^2}{\kappa^2}} \mathrm{Erfc}\left(\frac{\pi m}{\kappa}\right) - \kappa \right) \mathbf{m}_\alpha \mathbf{m}_\beta + \\ \delta_{\alpha\beta} \left(2\pi^{7/2} m^3 e^{\frac{\pi^2 m^2}{\kappa^2}} \mathrm{Erfc}\left(\frac{\pi m}{\kappa}\right) + \kappa^3 - 2\pi^2 \kappa\, m^2 \right) \end{array} \right) \qquad (20)$$

and including the $\mathbf{m} = 0$ term, in contrast to the Coulombic case.

2.3. Results

2.3.1. Alkanes in C36 and Drude.

Results for ρ, β_T, η, γ, and D of hexadecane at biologically relevant temperatures are listed in Table 3. The final column of each table lists the deviation from experiment,

averaged over the temperatures. Table 3 also includes results for ρ, β_T, and η for systems simulated using the isotropic LRC with the Drude FF.

The effects of long-range Lennard-Jones interactions are statistically significant for all cases. LJ-PME increases ρ by 2% for C36 and 1% for Drude. As consistent with an increase in density, β_T decrease (20% for C36, 10% for Drude), η increase (17% for C36, 12% Drude), and *D* decrease (23% for C36, 11% for Drude).

Results using the isotopic LRC for ρ and β_T are 0.3% higher and 4% lower that for LJ-PME, respectively. These are close, but not statistically equivalent. (Statistical errors in η are large, so it is not possible to assign statistical significance to the differences.) Recall that the isotropic LRC assumes that $g(r) = 1$ for $r > r_{\text{cut}}$. As is evident from the $g(r)$ for hexadecane plotted in Figure 4, $g(r)$ only becomes constant at approximately 18 Å, well beyond the standard $r_{\text{cut}} = 12$ Å.

Table 3. Hexadecane simulation averages and standard errors for density (ρ), isothermal compressibility (β_T), sheer viscosity (η), surface tension (γ), and translational diffusion (D) at various biological temperatures

		Temperature (K)			Average deviation from Exp.
		303.15	310.15	323.15	
ρ [g/mL]	C36	0.7483 ± 0.0001	0.7416 ± 0.0001	0.7289 ± 0.0001	−2.7 %
	C36, LJ-PME	0.7654 ± 0.0003	0.7593 ± 0.0001	0.7481 ± 0.0001	−0.40 %
	Drude	0.7544 ± 0.0002	0.7483 ± 0.0003	0.7375 ± 0.0001	−1.8 %
	Drude, LJ-PME	0.7620 ± 0.0002	0.7564 ± 0.0001	0.7460 ± 0.0002	−0.70 %
	Drude, LRC	0.7649 ± 0.0002	0.7591 ± 0.0001	0.7490 ± 0.0002	−0.40 %
	Exp.[129]	0.7665	0.7617*	0.7528	
β_T	C36	12.48 ± 0.12	13.16 ± 0.11	14.40 ± 0.09	41 %
$[10^{-10}\mathrm{m}^2/\mathrm{N}]$	C36, LJ-PME	10.04 ± 0.16	10.48 ± 0.22	11.35 ± 0.20	13 %
	Drude	9.99 ± 0.35	9.99 ± 0.31	11.94 ± 0.46	12 %
	Drude, LJ-PME	8.78 ± 0.14	9.49 ± 0.15	10.22 ± 0.16	0.60 %
	Drude, LRC	8.51 ± 0.17	9.11 ± 0.23	9.68 ± 0.25	−3.7 %
	Exp.[129]	8.896	9.307*	10.059	
η [cP]	C36	2.16 ± 0.06	1.89 ± 0.14	1.47 ± 0.03	−22 %
	C36, LJ-PME	2.55 ± 0.13	2.05 ± 0.12	1.81 ± 0.07	−8.4 %
	Drude	2.37 ± 0.08	2.22 ± 0.11	1.80 ± 0.13	−8.4 %
	Drude, LJ-PME	2.70 ± 0.20	2.52 ± 0.10	1.95 ± 0.20	2.6 %
	Drude, LRC	3.07 ± 0.32	2.34 ± 0.30	2.08 ± 0.26	6.8 %
	Exp.[129]	2.766	2.388*	1.866	
γ [dyn/cm]	C36	18.03 ± 0.49	16.86 ± 0.68	16.74 ± 0.67	−34.6 %
	C36, LJ-PME	24.79 ± 0.80	22.77 ± 0.72	19.73 ± 0.60	−18.6 %
	Drude	21.97 ± 0.41	21.89 ± 0.33	20.58 ± 0.26	−17.2 %
	Drude, LJ-PME	27.74 ± 0.56	26.26 ± 0.57	25.06 ± 0.42	1.60 %
	Exp.[129]	26.7	26.1*	25.0	
$D[10^{-6}$ $\mathrm{cm}^2/\mathrm{s}]$	C36	5.48 ± 0.03	6.41 ± 0.04	8.47 ± 0.08	34 %
	C36, LJ-PME	4.16 ± 0.04	4.95 ± 0.05	6.53 ± 0.08	3.0 %
	Drude	4.81 ± 0.03	5.77 ± 0.07	7.45 ± 0.06	1.8 %
	Drude, LJ-PME	4.30 ± 0.01	5.02 ± 0.05	6.63 ± 0.10	5.0 %
	Exp.[130]			6.32	

*Experimental values at 310.15 K interpolated with a polynomial fit.

In agreement with previous work,[101, 116] the influence of long-range LJ terms on surface tensions of alkanes is large. For the cutoffs used here, γ is increased 18–37% for C36 and 20–26% for Drude, depending on the temperature.

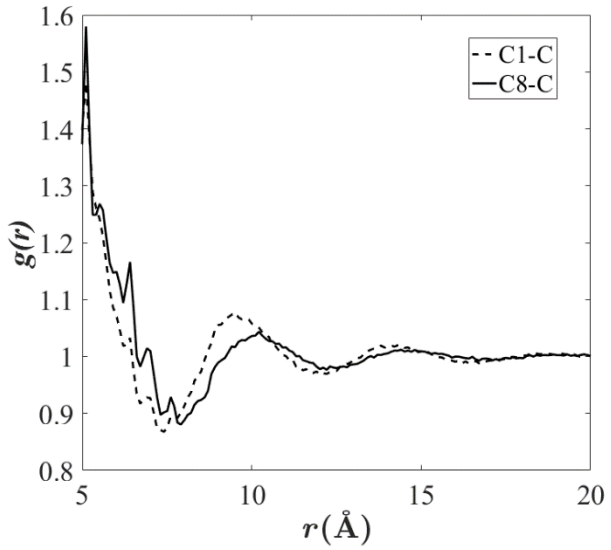

Figure 4. Radial distribution functions for hexadecane at 323.15 K. Drude FF without long-range LJ interactions. "C1-C" is between C1 and all other carbons; "C8-C" is between C8 and all other carbons. The first two peaks arising from nearest and next-nearest neighbors are not shown.

C36 without long-range LJ shows the largest differences from experiment for all quantities reported in Table 3. This is expected because the alkanes in C36 were originally parameterized with a pressure-based correction.[59] Both polarizability and the use of LJ-PME improve agreement with experiment in all cases, and in nearly all cases, Drude/LJ-PME achieves results closest to experiment. The agreement with experimental surface tensions is also best for Drude/LJ-PME (an average error of 1.6%).

Figure 5 plots T_1 for heptane and pentadecane at 312.15 K. Agreement with experiment for carbons near the center of pentadecane is excellent for all but C36. The terminal carbon (C1) is not as well described as the others in the Drude FF, indicating that a slight adjustment of the C1 torsional parameters should be considered. Differences with experiment are uniformly larger for heptane (approximately 25% lower for Drude/LJ-PME, and 40–65% higher for the others). The reduction in T_1 when long-range LJ terms are included is consistent with the increase in η. This is because rotational diffusion of the

long molecular axis, commonly referred to as tumbling, makes a significant contribution to the reorientational correlation functions of alkanes,[131] and the rotational correlation time τ (the integral of the correlation function) is proportional to viscosity. Hence, from eq. (10), an increase in τ reduces T_1. The effect of tumbling on hexadecane T_1 is somewhat smaller than for heptane, because the contribution of isomerization is larger. Heptane T_1 times are more influenced by rotational diffusion about the long axis (spinning) than those of hexadecane. Spinning of symmetric molecules is relatively insensitive to viscosity but is highly sensitive molecular shape and packing.[132] The large difference between Drude and Drude/LJ-PME results suggests a modulation of the relaxation associated with spinning.

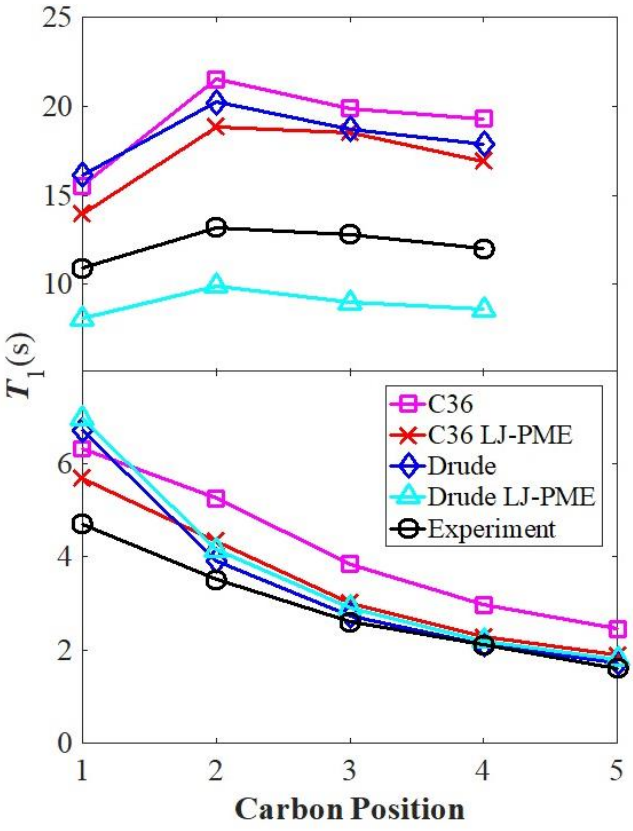

Figure 5. NMR spin-lattice relaxation times (T_1) from simulation and experiment. Heptane (top) and pentadecane (bottom).

2.3.2. Dependence on r_{cut} for non-bonded interactions.

To investigate the dependence of ρ and γ on r_{cut}, simulations of bulk hexadecane and the hexadecane/vacuum interface were carried out at 298.15 K using C36 and C36/LJ-PME for a range of values for r_{cut}. As Figure 6 indicates, LJ-PME is relatively insensitive to r_{cut}, and a value as low as 9 Å may be used for systems of pure alkanes. Without LJ-PME, ρ does not converge until approximately 24 Å, and γ is still increasing at this value of r_{cut}. The snapshots in Figure 7 illustrate the effect of cutoff for C36. The system simulated with LJ-PME has a smooth interface consistent with a surface tension of 25 dyn/cm (left). The surface is borderline unstable for r_{cut} = 8 Å, and a molecule can be seen evaporating (right).

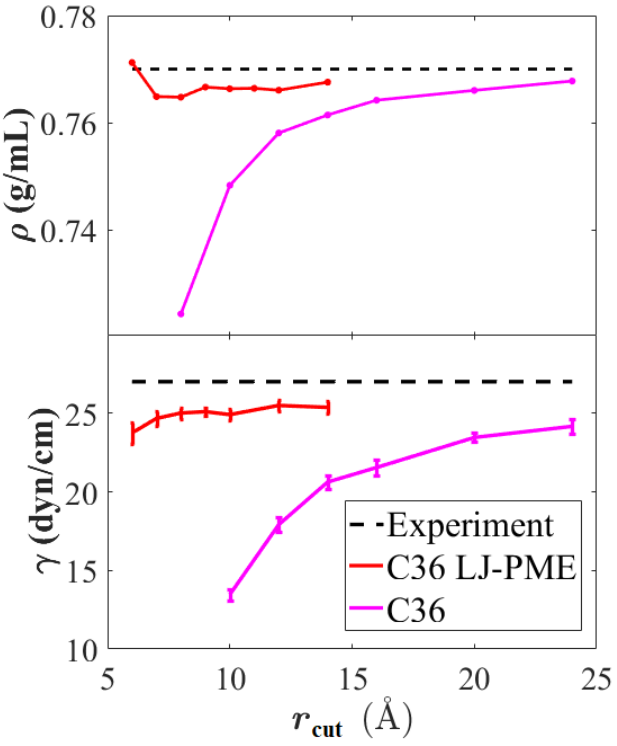

Figure 6. Density (top) and surface tension (bottom) of hexadecane vs. r_{cut}. . Standard errors are comparable to symbol for density

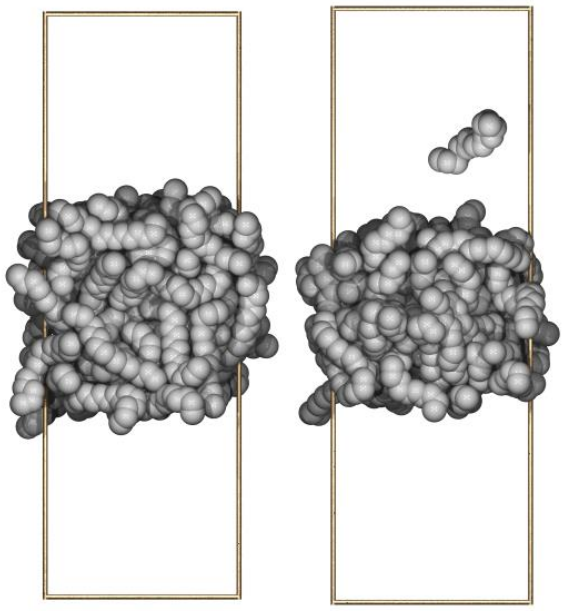

Figure 7. Hexadecane fluid/vacuum interface for r_{cut} = 8 Å. C36 with long-range Lennard-Jones interactions (left) and without (right). The boundaries of the unit cell are depicted with brass rods.

2.3.3. Temperature dependence of density and isothermal compressibility.

At 313.15 K, the volumetric coefficient of thermal expansion (α_V) for hexadecane is 9.07×10^{-4} K^{-1}.[133] This value is compared with simulation by fitting V_{mol} at three or four temperatures using a linear regression (Figure 8). While the trends are qualitatively correct, α_V from simulation overestimate experiment by 20–40% (Table 4). This indicates that the error in V_{mol}, and therefore density, will increase if simulations are run at higher temperatures. Slopes of the lines of best fit for Drude and Drude/LJ-PME are nearer to the slope of the experimental line of best fit; however, over the range of temperatures shown, V_{mol} for C36/LJ-PME most closely match the experimental data.

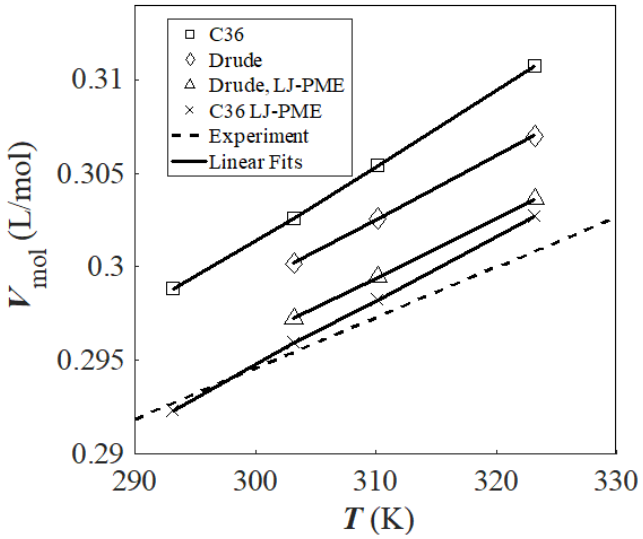

Figure 8. Temperature dependence of V_{mol} of hexadecane. Solid lines show the fit used to calculate values for α_V in Table 4.

Table 4. Thermal expansion coefficients α_V calculated for each FF over the range of biological temperatures tested, found using a linear fit.

Force Field	α_V ($K^{-1} \times 10^{-3}$)
C36	1.30
C36 LJ-PME	1.16
Drude	1.11
Drude LJ-PME	1.07
Exp.	0.907

Table 5 lists ρ and β_T at 393.15 K for an evaluation of the FFs at an elevated temperature. Deviations from experiment are generally 2–3 times larger than at biological temperatures (Table 3). The best agreement is obtained for Drude/LJ-PME.

Table 5. Hexadecane simulation averages at 393.15 K. ρ and β_T with standard errors.

		Temperature (K)	Avg. Error from Exp.
		393.15	
ρ [g/mL]	C36	0.6570 ± 0.0002	−6.6 %
	C36, LJ-PME	0.6775 ± 0.0002	−3.7 %
	Drude	0.6897 ± 0.0002	−2.0 %
	Drude, LJ-PME	0.6896 ± 0.0002	−2.0 %
	Exp.	0.7036	
β_T $[10^{-10}\mathrm{m}^2/\mathrm{N}]$	C36	32.98 ± 0.80	103 %
	C36, LJ-PME	20.44 ± 0.14	26 %
	Drude	21.20 ± 0.23	30 %
	Drude, LJ-PME	17.26 ± 0.23	6.0 %
	Exp.	16.24	

Experimental β_T for hexadecane at temperatures from 298.15–433.15 K, calculated from measurements of the velocity of sound, can be fit with a polynomial regression.[133] As evident from Figure 9, $a + bT^4$ provides a good fit to the data (Table 6 lists b for each fit), and Drude/LJ-PME again is the best model.

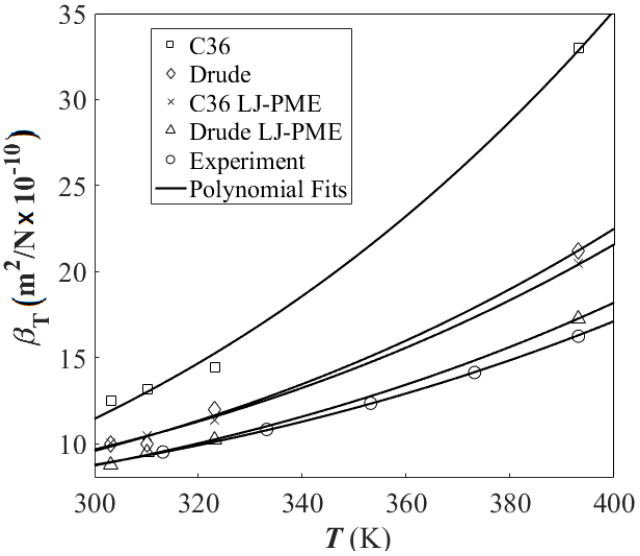

Figure 9. Temperature dependence of β_T for hexadecane. Curves show fits to the simulation and experimental data with a regression of the form $a + bT^4$. The exponent of T was chosen using χ^2analysis of the experimental data.

Table 6. Parameter b describing temperature dependence of β_T for hexadecane.

Force Field	b (K^{-4} m^2/N $\times$ 10^{-10})
C36	13.6
C36 LJ-PME	6.81
Drude	7.38
Drude LJ-PME	5.41
Exp.	4.77

2.4. Discussion

Long-range LJ dispersion interactions have a significant impact on numerous properties of alkanes. While they are especially important at the alkane-vacuum interface, they increase ρ and thereby decrease β_T and increase η. This effect is less pronounced in

systems of polar molecules (where long-range electrostatic interactions tend to dominate and are accounted for by PME). For example, increasing r_{cut} from 8 Å to 25 Å has a substantially smaller effect on the calculated surface tension (γ) of pure water than of pure hexadecane.[101] Specifically, water surface tension at 323.15 K for the C27r FF is 41.5 ± 0.5 dyn/cm for $r_{\mathrm{cut}} = 8$ Å and 51.3 ± 0.4 dyn/cm for $r_{\mathrm{cut}} = 25$ Å; an increase of nearly 25 %. For hexadecane, $\gamma = 5.9 \pm 0.2$ and 22.7 ± 0.4 dyn/cm at 8 and 25 Å respectively; an increase of nearly 400 %. Nevertheless, increasing r_{cut} to include more long-range LJ interactions brings γ closer to experiment in both cases.

The simplest way to include long-range LJ interactions is to use the isotropic correction.[102] This correction assumes the system is isotropic in pressure, which precludes its use for anisotropic systems. A key assumption in the isotopic LRC is that the $g(r)$ is 1 at distances larger than r_{cut}. The present study shows that fluids of larger molecules like hexadecane have significant structure beyond the usual 10–12 Å cutoffs (Figure 4), indicating that the isotopic LRC is less generally applicable than previously assumed. The pressure-based LRC[103] is also not applicable to anisotropic systems, while assumptions of homogeneity limit the appeal of the IPS methods.[101, 114]

The LJ-PME formalism solves a long-standing problem in the simulation field: the rigorous and computationally efficient treatment of long-range LJ interactions. Its recent reformulation permits the use of arbitrary LJ combination rules, making it ideally suited to macromolecular FFs. While the modified LJ-PME method suffers from small discontinuities in the forces at r_{cut}, microcanonical simulations of n-hexadecane and water boxes reveal that these force discontinuities have a negligible impact on simulations, even for r_{cut} as low as 7 Å. Our implementation defaults to potential shifting, with an option to

use switching to remove force discontinuities. Properties evaluated for alkane systems are consistent for values of r_{cut} as low as 9 Å (Figure 6).

The present study focuses on alkanes, a natural starting point for parametrization of lipid force fields. In Drude and C27r, which was later slightly modified to become C36, alkanes were originally parameterized using a pressure-based correction to account for long-range LJ interactions.[59, 74] This correction was needed, among other reasons, to bring the densities of alkanes into satisfactory agreement with experiment. The C36 lipid FF did not include long-range LJ interactions (explicitly or with a correction) for reasons of consistency with other CHARMM FFs.

The results here (Table 3) indicate that use of the new LJ-PME approach to evaluate density and surface tension has an effect similar to earlier methods for estimating the long-range LJ interactions. That is, the densities of both the C36 and the Drude systems increased slightly at all temperatures tested, while the surface tensions increased more significantly, bringing all measurements of these quantities closer to experimental target values. In some cases, the isotropic LRC yielded results nearer to experiment than LJ-PME. For example, Drude densities with the isotropic LRC are nearer to experiment than with LJ-PME. This result is expected because the Drude FF was originally parameterized using a spatially isotropic, pressure-based correction.[74] However, a distinction must be drawn between similarity with experimental results and accurate treatment of the long-range forces in simulation. Figure 4 shows that use of the isotropic LRC for $C_{16}H_{34}$ is not valid with the standard value of $r_{\mathrm{cut}} = 12$ Å because $g(r) \neq 1$. Figure 6 shows that increasing r_{cut} causes ρ to converge to the value obtained using LJ-PME, indicating that LJ-PME treats the long-range dispersion forces accurately.

In a recent study, Fischer *et al.*[134] found a similar increase in the surface tension of 146 organic liquids when LJ-PME is implemented with the C36 general FF;[135] the general FF systematically underestimates γ without a correction, but overestimates γ with LJ-PME. In contrast, present results for hexadecane show an approximately 20% underestimate of γ even with the use of LJ-PME. This discrepancy can be explained by the use of different correction methods for parameterization. The C36 general FF employed an isotropic correction for long-range LJ interactions,[135] whereas the parameterization of alkanes for C36 used a more intensive pressure-based correction.[59, 103] The deviation of γ from experiment in both instances suggests a reparameterization of C36 to include LJ-PME would improve results.

Like γ, isothermal compressibility (β_T) is significantly affected by long-range Lennard-Jones interactions. The Drude FF consistently over-estimates β_T, indicting the systems are not sufficiently compact because the long-range attractive LJ interactions are absent. In contrast, use of the isotropic LRC results in consistent under-estimation. With LJ-PME, there is less error in the compressibility measurements and no clear trend of over- or under-estimation in the range of temperatures applicable to biological phenomena.

LJ-PME brings the dynamical properties viscosity and self-diffusion closer to experiment, as consistent with an increase in density. Without LJ-PME, both C36 and Drude underestimate viscosity and overestimate diffusion.

NMR spin lattice relaxation times (T_1) for carbons of pentadecane are reasonably described for C36/LJ-PME and the Drude models (Figure 5, bottom), and improvements are likely to be found by modifying the torsion angles. The relatively worse results found for heptane (Figure 5, top) highlight the difficulties of accurately capturing the nuances of

molecule shape on rotational diffusion. It would be of interest to simulate rotational relaxation of highly symmetric molecules such as benzene to refine force field to this level of detail. However, because the primary application of the CHARMM FFs is to biopolymers and membranes, pentadecane is the more important target.

While many MD simulations are run at temperatures near standard or body temperature, simulations at elevated temperatures also yield valuable information for biomolecular systems. Simulations of pure bilayers with higher-than-biological melting temperatures can be compared with experimental data to check for force field accuracy.[29, 136] Furthermore, simulations of large systems, such as membrane-bound proteins, are routinely run at high temperatures to populate the energy landscape using the replica exchange method.[137]

Modeling atomic polarizability provides MD methods with additional degrees of freedom, which should increase the transferability of parameters, allowing polarizable FFs to achieve better temperature dependence trends. Figure 8 and Table 4 show that Drude/LJ-PME obtains the closest agreement with the experimental thermal expansion coefficient of hexadecane. The slope of the linear regression for V_{mol} vs. T is also nearest to the experimental slope for Drude/LJ-PME; however, the *y* intercept of the line of best fit is too high, causing V_{mol} to be slightly higher than experimental values across the temperatures tested. Although C36/LJ-PME has smaller errors from experiment in V_{mol} over the temperatures represented in the figure, the effective thermal expansion coefficient is not as close to the experimental value. Thus, Drude/LJ-PME obtains densities closer to experiment 393.15 K (Table *5*).

Because the dependence on temperature of β_T is quartic, errors in temperature dependence are exacerbated at elevated temperatures (Figure 9). The *b* parameter of C36 without LJ-PME is almost three times larger than experiment (Table 6), causing a greater than 100% overestimation of β_T at 400 K. With LJ-PME, this is dramatically improved, but C36/LJ-PME still overestimates β_T at 400 K by about 25 %. In contrast, Drude/LJ-PME over-estimates *b* by only 13%. At 393.15 K, Drude/LJ-PME overestimates β_T by only 6 % and under-estimates density by only 2 % (Table 5). While this advantage in temperature dependence could be attributed to parameterization, another possible explanation is the increase in degrees of freedom, allowing increased responsiveness of the polarizable systems to temperature fluctuations. For example, thermal excitation of the Drude oscillators creates a feedback loop in which resulting structural rearrangement affects electrostatic interactions.

Consistent with the second explanation, polarizable force fields have previously been shown to perform better at elevated temperatures in systems of pure water,[138] water/salt solutions,[139] and polypeptides.[140] Jiang *et al.*[139] found that, for various concentrations of aqueous NaCl, the Drude polarizable FF developed by Kiss and Baranyai, AH/BK3,[141, 142] yields ρ and η nearer to experimental values at 373.15 and 473.15 K than the additive SPC/E+SD models.[143, 144] The induced-dipole AMOEBA force field shows close agreement with experimental temperature dependence for ρ of pure water up to 363 K, whereas the additive, five-site TIP5P model underestimates density above 320 K.[138] Polarizability also improves the temperature dependence of spontaneous folding: A study on cooperative helix formation in the $(AAQAA)_3$ peptide indicates that, in events

driven by hydrogen bonding, the temperature dependence of secondary structure is more accurately represented by Drude than by C36.[140]

In summary, LJ-PME is a rigorous method for including long-range LJ interactions in simulations. It allows the use of a shorter real-space cutoff for LJ and electrostatic interactions, thereby increasing computational efficiency. The use of LJ-PME improves agreement with experiment for density, isothermal compressibility, viscosity, diffusion constant, and surface tension at all temperatures simulated for both the C36 additive and Drude polarizable FFs. Additionally, LJ-PME improves agreement with experimental trends in temperature dependence for calculations of V_{mol} and β_T, though results at biological temperatures (303 to 323 K) are better than at 393.15 K. It is now practical and advisable to include long-range LJ interactions in subsequent FF development. While the C36 additive force field with LJ-PME remains a useful model for liquid alkanes, overall, the Drude force field with LJ-PME shows the closest agreement with the experiments considered here.

When applied to simulations of linear ethers in Chapter 3, LJ-PME improves agreement with experimental densities. However, bilayers run with the C36 lipid FF condense when LJ-PME is used. The new Drude lipid FF, discussed in section 1.3.4, yields poor agreement with experimental A_l for all PC lipids except DMPC, substantially overestimates bilayer area compressibility moduli, and underestimates lipid self-diffusion coefficients by an order of magnitude.[76] So while use of LJ-PME and Drude would solve two enduring issues with lipid FFs; force imbalance between polar and nonpolar regions and energetics of transfer from water into the bilayer interior; further parameterization is needed before either atomic polarizability or long-range LJ interactions are included in all-

atom simulations of lipids. The results for alkanes lay the groundwork for future parameterization.

Chapter 3. Parameterization of the CHARMM All-Atom Force Field for Linear Ethers, Ether Lipids, and Plasmalogens.

3.1. Introduction

Compounds containing ether groups are widely used in industry and medicine. Ether groups consist of both a polar oxygen atom capable of participating in hydrogen bonds and a nonpolar aliphatic region. Polyethylene glycol (PEG) is a polyether with industrial and medical applications including use in protein purification,[145] in osmotic laxatives,[146] and cosmetic products.[147] Phospholipids that contain an ether linkage between the glycerol backbone and tail (hereafter referred to as ether lipids) are prevalent in mammalian nerve tissue and blood. Up to 52% of phospholipids in nerve myelin[15] and 15% in human red blood cells[148] are ether-linked. Additionally, ether lipids are predominant in membranes of archaea and are thought to contribute to the resilience of extremophiles over a wide range of temperatures, salinities, pressures, and pHs.[149] Recent experimental findings verify that the ether linkage alters bilayer structure, water permeability[150] and water organization in the bilayer.[151]

MD simulations of ethers and ether lipids have a range of applications. Recently, MD simulations of aqueous PEG have been used to characterize the role of PEG chain length in protein purification,[152] and a study of PEG-grafted membrane interactions with alginate gel foulant investigated the antifouling property of PEG which can inhibit water purification in the process of membrane separation.[153] MD simulations comparing ether- and ester-linked lipids[154, 155] have probed the chemical effects of the ether linkage. However, the surface areas per lipid for ether-linked bilayers in the biologically-relevant constant number, pressure, and temperature (NPT) ensemble have been systematically underestimated. In one such study, Pan et al.[155] modified the C36[34, 81] FF to model a bilayer

of ether-linked 1,2-di-O-hexadecyl-*sn*-glycero-3-phosphocholine (DHPC). The partial-charge and dihedral parameters for the ether linkage were adapted from the C36 lipid force field and an earlier study by Shinoda et al.[156] The partial charge on the ether oxygen was -0.40*e*, similar to the C36 charge on the ether oxygen in PEG (-0.34*e*). The resulting surface area per lipid (A_l) of DHPC was too low by over 8 Å^2/lipid in the NPT ensemble, and the authors resorted to fixing the volume of the simulation box to avoid condensing.[155] These results indicate a deficiency in the C36 parameters for linear ethers such as PEG.

C36 partial-charge assignments for the ether oxygen and adjacent carbons in linear ethers were chosen empirically with the goal of reproducing neat liquid properties and hydration energies.[81] Lennard-Jones parameters were directly transferred from parameterization of cyclic ethers. It was later shown that dihedral parameters for the linear ether dimethoxyethane ($C_4H_{10}O_2$; hereafter DMOE) underestimated the *gauche* character of the central O-C-C-O dihedral, resulting in reduced populations of TGT and TGG' conformations (C-O-C-C, O-C-C-O, and C-C-O-C dihedrals, respectively) in mixtures with water.[157] In the referenced study, Lee et al. presented revised dihedral parameters but did not reinvestigate the partial-charge assignments for linear ethers. The revised parameters yielded good agreement with experimental persistence lengths of a 27-mer PEG and various lengths of polyethylene oxide in water, but the official C36 release of the FF did not include the revisions.

The present study demonstrates that C36 parameters do not yield accurate densities for small chains of PEG, and the free energy of hydration (ΔG_{hyd}) of diethoxyethane ($C_6H_{14}O_2$; hereafter DEOE), a model for the glycerol-ether linkage in ether lipids, also deviates from experiment. Furthermore, in agreement with the findings of Pan et al.,[155]

applying C36 parameters for PEG to the glycerol-ether linkage of a DHPC bilayer results in bilayer condensation and A_l that is too low. Comparison of simulated and experimental scattering density profiles (SDP) indicates that water is not penetrating deeply enough into the bilayer, an issue that is likely related to the electronegativity of the ether oxygen and surrounding carbons.

Motivated by the preceding inaccuracies, *ab initio* results were applied to the development of a new FF for linear ethers and ether lipids, called C36e. Specifically, electrostatic potential (ESP) mapping is used to assign partial charges to linear ethers, and dihedral parameters are fit to reproduce potential energy scans. Resulting densities and ΔG_{hyd} for linear ethers are compared with experiment. The parameters for linear ethers are then applied to a DHPC bilayer and improve agreement with experimental SDP, A_l, and form factors. Results for DHPC bilayers are compared with 1,2-dipalmitoyl-*sn*-phosphatidylcholine (DPPC), identical to DHPC except having ester linkages between the glycerol backbone and saturated tails. This comparison is used to examine the structural and chemical effects of the ether vs. ester linkage on membrane A_l, area compressibility modulus (K_A), dipole potential drop ($\Delta\Psi$), and water organization in the headgroup region.

This approach is consistent with previous development of the C36 lipid FF by Klauda et al.[34] In that study, QM-based charges of DPPC model compounds in the gas phase were compared with AM1-based charges of hydrated lipid bilayers and were found to be very similar, typically differing by 0.05*e* or less. Torsional parameters for C36 were assigned from direct fits to vacuum QM-based conformational energies of model compounds. Also consistent with C36 development, the present chapter aims to reproduce

the experimental surface area lipid and density profiles from neutron and X-ray scattering experiments.

The C36e model for DHPC introduces parameters for the glycerol-ether linkage, and study of MD simulations of DHPC lipids are useful for understanding the effects of the ether linkage as a chemical perturbation. But DHPC lipids are not found in the human body. In a later study (in progress), the new C36e FF is applied to an ether lipid prevalent in human brain tissue: ethanolamine plasmalogen. Plasmalogens, which are characterized by an ether bond in position *sn*-1 to an alkenyl group, are present in high concentrations in brain, retina and other neural tissues such as gray and white matter.[158-161] Synaptic vesicles involved in neurotransmitter release have highly heterogenous bilayers enriched in the ethanolamine plasmalogen. [162-164] Perhaps because the *sn*-2 acyl chain tends to be polyunsaturated,[165] elevated quantities of plasmalogens are found in lipid rafts.[166, 167]

Phosphatidylethanolamine plasmalogen (PLAPE) investigated here corresponds to an ether phospholipid that has one of its fatty acyl chains linked with a *cis*-vinyl-ether bond at the *sn*-1 glycerol position and the ethanolamine polar headgroup at *sn*-3. The present results introduce CHARMM all-atom FF parameters for PLAPE. Simulations of POPC:PLAPE mixtures in 2:1, 1:1, and 1:2 ratios are compared with experimental low angle x-ray scattering data. Reasonable agreement is found in reproducing form factors indicative of bilayer structure.

Section 3.2 describes the methodology of quantum mechanical (QM) calculations and MD simulations. Section 3.3 presents and discusses new C36e parameters and resulting properties of linear ethers and bilayers, with comparison to a purely ester-linked bilayer.

Section 3.4 provides both small molecule and bilayer results for plasmalogens. Conclusions are summarized in section 3.5.

3.2. Methods

This section describes the methodology used in *ab inito* calculations (3.2.1), fitting the C36e FF to the QM results (3.2.2), and MD simulations (3.2.3 and 3.2.4).

3.2.1. Quantum mechanical calculations

The NWChem program[168] was used for all *ab inito* calculations. For the purpose of developing new partial-charge parameters, the ESP best-fit partial charges were found for several linear ether molecules using the optimized geometry of the all-*trans* state: 1,2-diethoxyethane (DEOE), 1,2-dimethoxyethane (DMOE), diethylene glycol (PEG2), triethylene glycol (PEG3), and 1,2-dibutoxyethane (DBOE); and two linear vinyl ethers for development of plasmalogen parameters: 1-ethoxypropene and diethylene glycol divinyl ether. Charges were computed from the MP2 densities using the CHELPG method.[169] In this method, atomic charges are fit to reproduce the molecular ESP at several points around the molecule.

To develop new dihedral parameters, potential energy scans were computed about the O-C-C-O and C-O-C-C dihedrals of DEOE and DMOE and the C-O-C=C and C-C-O-C(=C) dihedrals of 1-ethoxypropene (for plasmalogens) from $[-180:10:180]$ degrees with other geometries relaxed.

All optimization and ESP fitting was completed at the MP2/cc-pVDZ level using the DRIVER module with a starting structure near the corresponding geometry, and also for DMOE in the all-*trans* state using the aug-cc-pVDZ basis set to observe the effect of basis size on partial charges.

Conformational energies at the CCSD(T)/aug-cc-pVTZ level were estimated for the optimized configurations using Hybrid Methods for Interaction Energies (HM-IE) developed by Klauda et al.[170] The HM-IE assume that the effects of electron correlation and basis set size are additive. Energies at the CCSD(T) level of theory with a large basis set (LBS = aug-cc-pVTZ in this case) are estimated by calculating CCSD(T) energies with a smaller basis set (SBS = aug-cc-pVDZ) and a correction is added for the difference between the MP2 energies with a LBS and a SBS as follows:

$$E^{\mathrm{conf}}\left[\frac{\mathrm{CCSD(T)}}{\mathrm{LBS}}\right] \cong E^{\mathrm{conf}}\left[\frac{\mathrm{CCSD(T)}}{\mathrm{SBS}}\right] + \left(E^{\mathrm{conf}}\left[\frac{\mathrm{MP2}}{\mathrm{LBS}}\right] - E^{\mathrm{conf}}\left[\frac{\mathrm{MP2}}{\mathrm{SBS}}\right]\right)$$

$$\equiv E^{\mathrm{conf}}[\mathrm{MP2:CC}]. \qquad (21)$$

Since the MP2 energies are needed to compute the CCSD(T) energies, two sets of calculations were necessary to find $E^{\mathrm{conf}}[\mathrm{MP2:CC}]$.

3.2.2. C36 potential energy scan and dihedral fitting procedure

Potential energies were computed for various conformations of DMOE and DEOE, and of 1-ethoxypropene (for plasmalogens), using the CHARMM program.[171]

The initial configuration was set to all *trans* and then the specified torsion was rotated for successive energy evaluations (other torsions remained *trans*). At each conformation, the desired torsion was held constant while coordinates were relaxed, and the relative energy was found by subtracting the minimum.

Potential energy scans were performed by rotating the intended dihedral between $[-180:10:180]$ degrees with the torsional parameters in eq. (3) $k_{\varphi,n}$ and δ_n set to zero. A script by Guvench and MacKerell[172] was used to find the final dihedral parameters. The script uses Monte Carlo simulated annealing to minimize mean-squared error between the

MD potential energy and the QM relative conformational energies. To compare the final parameters, scans were completed with C36 and C36e about each fitted dihedral between $[-180:10:180]$ degrees with all other geometries relaxed.

3.2.3. Molecular dynamics simulations of saturated linear ethers

MD simulations of linear ethers, listed in Table 7, were used to find the densities (ρ) and the free energies of hydration (ΔG_{hyd}).

Table 7. MD simulations of linear ethers. Temperature (T), run time (t_{run}), and number of replicates (n_{run}), of each simulation. PME denotes that long-range interactions are summed for electrostatic, but not Lennard-Jones, interactions; LJ-PME indicates that electrostatic and Lennard-Jones interaction are included.[173]

	T (K)	Cutoff Method	t_{run} (ns)	n_{run}	Use
DEOE	288.15	PME	30	1	ρ
		LJ-PME	30	1	ρ
	298.15	PME	2*	3	ΔG_{hyd}
DMOE	288.15	PME	30	1	ρ
		LJ-PME	30	1	ρ
	298.15	PME	2*	3	ΔG_{hyd}
PEG2	293.15	PME	30	1	ρ
		LJ-PME	30	1	ρ
PEG3	293.15	PME	30	1	ρ
		LJ-PME	30	1	ρ

*Time per run for each value of attenuation parameter.[174]

ΔG_{hyd} of DEOE and DMOE were obtained using free energy perturbation (FEP) according to the protocol developed by Deng and Roux.[174] This approach involves perturbing the nonbonded potential in 3 stages, decoupling the electrostatic, LJ repulsive, and LJ dispersive interactions between the solute and solvent. The total LJ potential is decoupled into U_{ij}^{rep} and U_{ij}^{disp}:

$$U_{ij}^{\mathrm{rep}}(r_{ij}) = \begin{cases} \varepsilon_{ij}\left[\left(\frac{r_{ij}^{\min}}{r_{ij}}\right)^{12} - 2\left(\frac{r_{ij}^{\min}}{r_{ij}}\right)^{6} + 1\right];\ r \le r_{ij}^{\min} \\ 0;\ r > r_{ij}^{\min} \end{cases} \quad (22)$$

$$U_{ij}^{\mathrm{disp}}(r_{ij}) = \begin{cases} -\varepsilon_{ij};\ r \le r_{ij}^{\min} \\ \varepsilon_{ij}\left[\left(\frac{r_{ij}^{\min}}{r_{ij}}\right)^{12} - 2\left(\frac{r_{ij}^{\min}}{r_{ij}}\right)^{6}\right];\ r > r_{ij}^{\min} \end{cases} \quad (23)$$

For the free energy simulations, the potential energy is expressed in terms of three coupling parameters s, ξ, and λ:

$$U(\mathbf{X},\mathbf{Y},s,\xi,\lambda) = U_{\mathrm{u}}(\mathbf{X}) + U_{\mathrm{v}}(\mathbf{Y}) + U_{\mathrm{uv}}^{\mathrm{rep}}(\mathbf{X},\mathbf{Y};s) + \xi U_{\mathrm{uv}}^{\mathrm{disp}}(\mathbf{X},\mathbf{Y}) + \lambda U_{\mathrm{uv}}^{\mathrm{elec}}(\mathbf{X},\mathbf{Y}) \quad (24)$$

Here, U_{u} is the internal potential energy of the solute, U_{v} is the potential energy of the solvent, U_{uv} terms are decoupled interaction energies between solute and solvent, and **X** and **Y** are the coordinates of the solute and solvent, respectively. The repulsive LJ term, due to its sharp dependence on separation distance, cannot be accurately treated with a linear perturbation. Instead, a soft-core potential is used:

$$U_{ij}^{\mathrm{rep}}(r_{ij},s) = \quad (25)$$

$$\begin{cases} \varepsilon_{ij}\left[\dfrac{{r_{ij}^{\min}}^{12}}{\left(r_{ij}^2 + (1-s)^2{r_{ij}^{\min}}^2\right)^6} - 2\dfrac{{r_{ij}^{\min}}^{6}}{\left(r_{ij}^2 + (1-s)^2{r_{ij}^{\min}}^2\right)^3} + 1\right];\ r \le r_{ij}^{\min}\sqrt{1-(1-s)^2} \\ 0;\ r > r_{ij}^{\min}\sqrt{1-(1-s)^2} \end{cases}$$

The staging parameter *s* was set to 0.0, 0.2, 0.3, 0.4, 0.5, 0.6, 0.7, 0.8, 0.9, and 1.0. For the electrostatic term, the coupling parameter λ was increased from [0,1] in increments of 0.05, with a 0.1 window size, such that half of each window overlaps the previous window. The nonbonded free energies from simulations using the different staging or coupling parameters were processed and summed using a combination of Weighted Histogram Analysis Method[175-177] and thermodynamic integration.[178]

A single molecule was simulated in a vacuum for the initial stage of the thermodynamic cycle, and in the aqueous phase for the final stage. The water boxes used in the aqueous phase were pre-equilibrated and contained between 460 and 470 waters. Production simulations of 2 ns for each staging or attenuation parameter were run using the CHARMM program[33] in the NPT ensemble as described in Sec. 2.2.1. A timestep of 2 fs was used.

Two different cutoff schemes were employed to treat long-range Lennard-Jones (LJ) interactions to determine densities. Both schemes use a cutoff r_{cut} of 12 Å for evaluating non-bonded interactions directly in real space; outside of r_{cut}, electrostatic interactions are evaluated in reciprocal space with the particle-mesh Ewald method (PME). In the first scheme, a force-switching function was used to modulate LJ interactions near the interface between real and reciprocal space, and outside of r_{cut} the interactions are neglected. In the second scheme, a potential-switching function modulates LJ interactions near the interface, and outside of r_{cut} the long-range LJ interactions are computed with the newly-implemented LJ-PME,[179, 180] discussed in Chapter 2.

All small molecule simulations not used for FEP calculations were run using CHARMM[171] with a 1-fs timestep and an initial cubic box length of between 29 – 30 Å. The NPT ensemble was used as described in Sec. 2.2.1. Standard error in ρ was estimated from uncorrelated blocks of data (five 6-ns blocks for each 30-ns simulation), and in ΔG_{hyd} from replicates.

3.2.4. Molecular dynamics simulations of bilayers

Table 8 lists simulations of pure DHPC and pure DPPC bilayers presented in this study. Structural and mechanical properties calculated include form factors ($|F(q)|$), SDP,

A_l, and K_A. Properties focusing on the interaction of water with the ether and ester linkages are: pair-correlation functions, $g(r)$, of the ether oxygen (in DHPC) and ester and carbonyl oxygens (in DPPC) with water; and z-profiles of the electrostatic potential (ψ), water potential of mean force ($\mathrm{pmf_w}$), and density-weighted orientation of water dipole, $\rho(z)\cos\theta(z)$.

Table 8. MD bilayer simulations. Temperature (T), run time (t_{run}), number of replicates (n_{run}), and quantities evaluated.

	T (FF)	$t_{\mathrm{run}} \times n_{\mathrm{run}}$ (ns)	Use
DHPC	333 K (C36 and C36e)	100 × 3	A_l, K_A, SDP $\lvert F(q)\rvert$ $\rho(z)\cos\theta(z)$, ψ, $\mathrm{pmf_w}$ $g(r)_{\mathrm{ether-water}}$
	321 K (C36e)	100 × 3	A_l, K_A, SDP
	333 K (C36e); 0.15 M NaCl	100 × 3	A_l, SDP
DPPC	333 K (C36)	100 × 3	A_l, K_A $\rho(z)\cos\theta\,(z)$, ψ, $\mathrm{pmf_w}$ $g(r)_{\mathrm{ester-water}}$ $g(r)_{\mathrm{carbonyl-water}}$

Bilayer simulations contained a total of 80 lipids (40 per leaflet) and 30 waters per lipid. Initial coordinates were produced by the CHARMM-GUI[181] *Membrane Builder*[182-184] for DPPC. Necessary atom type substitutions and deletions were made to produce the ether linkage of DHPC. "C36" denotes partial charge assignments based on C36 charges for PEG and unchanged dihedral parameters. "C36e" denotes the new partial-charge and dihedral parameters.

3.3.1. Parameterization of model linear ethers. Simulations were run in NAMD[185] using a 2-fs timestep and Langevin damping coefficient of 1/ps. A LJ force-switching function was

used (10 to 12 Å) to modulate the LJ potential at the cutoff. Long-range electrostatic interactions were evaluated with the Particle mesh Ewald (PME) method.[49] Temperature was held constant by Langevin dynamics with a weak coupling constant of 1 ps^{-1}. Pressure was maintained in constant number, pressure, and temperature (NPT) simulations by a Nosé-Hoover-Langevin piston[186, 187] at 1 bar.

Data were analyzed after equilibration, from 30 – 100 ns. Standard errors between replicates were calculated for A_l and scattering parameters, and from uncorrelated blocks for K_A. "NBFIX" parameters for carboxylate, ester, and phosphate oxygens[188] were used in simulations with NaCl.

The scattering densities of functional groups from simulation were obtained with the software package SIMtoEXP.[189] For ready comparison with the experimental SDP,[155] three Gaussians were used to describe the volume probabilities of the lipid headgroup: one each for the glycerol and ether linkage (G1), the phosphate and CH_2CH_2N moiety (G2), and the trimethyl groups of the terminal choline (G3). For calculating the bilayer hydrocarbon thickness ($2D_C$), the total hydrocarbon region was represented by an error function. Matlab R2016a[190] was used to fit the Gaussian and error functions and obtain the difference between electron density maxima (D_{HH}). X-ray and neutron form factors were calculated using SIMtoEXP[189] with a Fourier transform of the total densities.

Area compressibility moduli of DHPC and DPPC bilayers were calculated using fluctuations in area:[191]

$$K_A = \frac{k_B T \langle A_l \rangle}{\langle \sigma_{A_l}^2 \rangle n_L}. \quad (26)$$

Here, $\langle \sigma_{A_l}^2 \rangle$ is the mean square fluctuation in area per lipid and n_L is the number of lipids per leaflet.

The electrostatic potential profile along the bilayer normal was calculated by integration of the Poisson equation:

$$\psi(z) = -\frac{4\pi}{\epsilon_0}\int_0^{z'} \rho_c(z'')dz'' \quad (27)$$

where ρ_c is the total time-averaged charge density and ϵ_0 is the permittivity of free space. ψ is greater at the center of the membrane than in bulk water. The total dipole potential drop across the membrane, $\Delta\Psi$, is here defined as the difference in the electrostatic potential of bulk water from that inside the membrane, $\psi(0)$:[120]

$$\Delta\Psi = \psi(0) - \psi(z) = -\frac{4\pi}{\epsilon_0}\int_0^{\infty}\int_0^{z'} \rho_c(z'')dz''dz'. \quad (28)$$

The upper limit of the inner integral, z', is set to be in bulk water. CHARMM[171] was used to find the water density and dipole orientation with respect to position along the bilayer normal, $\rho(z)\cos\theta\,(z)$. The software package Visual Molecular Dynamics (VMD)[192] was used to find the pair-correlation functions, $g(r)$, for ether oxygens of DHPC and carbonyl and ester oxygens of DPPC with water hydrogens, and to capture images of the bilayers. Peak positions and integrals of $g(r)$ were computed with Matlab R2016a.[190]

3.3. Results for Linear Ethers and DHPC

Section 3.3.1 presents parameters for linear ethers and simulation results. Section 3.3.2 presents parameters for the ether-linked lipid DHPC and simulation results for DHPC bilayers. Section 3.3.3 has a comparison of DHPC with ester-linked DPPC bilayers.

3.3.1. Parameterization of model linear ethers

Figure 10 shows the partial charges on heavy atoms (and terminal hydrogens in PEG3) obtained from the MP2 densities and averaged for symmetry. DEOE and DBOE were chosen as models for the glycerol-ether linkage in DHPC because of their saturated

hydrocarbon chains. The charges on ether oxygens and surrounding carbons are significantly greater in magnitude than the C36 partial-charge assignments for a PEG monomer. The C36 PEG oxygen has a partial charge of -0.34*e* in units of positive elementary charge (*e*), and -0.01*e* for neighboring carbons; QM results indicate PEG oxygens have a charge of approximately -0.60 *e* (depending on chain length), and around 0.4*e* for neighboring carbons. The longer hydrocarbon tails of DBOE exert a stabilizing effect on the charges of the four neighboring carbons; they range from (0.38*e*, 0.44*e*), whereas in the shorter-chained DEOE, the charges on the two central carbons are lesser in magnitude (0.31*e*) and carbons in positions 2 and 7 carry a greater charge (0.53*e*). To model the glycerol-ether linkage of phospholipids, the final partial-charge parameters for C36e (Figure 11) were chosen to mimic charges of the longer-chained DBOE. Changes were made to the general FF file and the lipids file. Compatible FF files and a stream file with all updated parameters is available for download at: https://user.eng.umd.edu/~jbklauda/ff.html

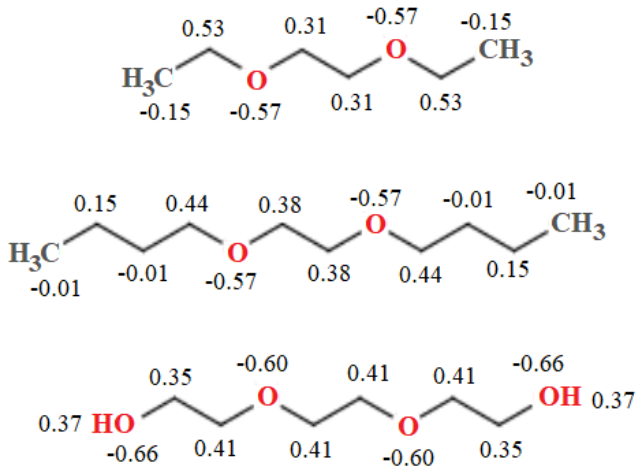

Figure 10. Partial charges for model linear ethers. MP2/cc-pVDZ and CHELPG method (averaged for symmetry). From top: 1,2-diethoxyethane, 1,2-dibutoxyethane, and triethylene glycol. Charges are in multiples of elementary charge, $+e$, and are shown for heavy atoms and terminal hydrogens of triethylene glycol.

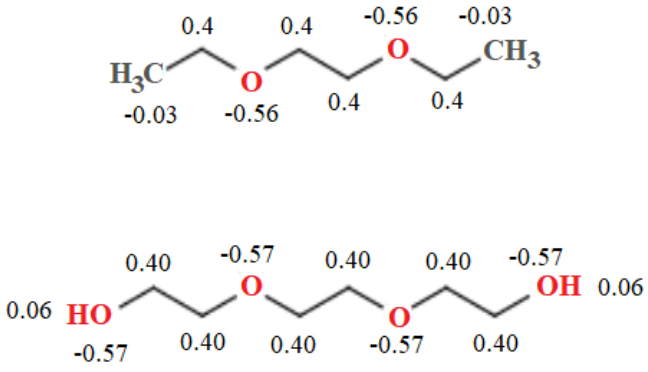

Figure 11. C36e partial-charge assignments for model linear ethers. 1,2-diethoxyethane (top); triethylene glycol (bottom). Charges are in multiples of elementary charge, $+e$, and are shown for heavy atoms and terminal hydrogens of triethylene glycol.

Figure 12 plots the torsional potential about two dihedrals of DEOE: C-O-C-C and the central O-C-C-O. Of note is the difference between the *trans* and *gauche* wells of the two dihedrals. The *gauche* well of O-C-C-O is only 0.265 kcal/mol higher than the *trans*; the C-O-C-C *gauche* well is 1.47 kcal/mol higher. The curvatures also differ. The *gauche* well of O-C-C-O is well-defined at 70°; the C-O-C-C well reaches a local minimum at 90° and has a large radius of curvature through 50°.

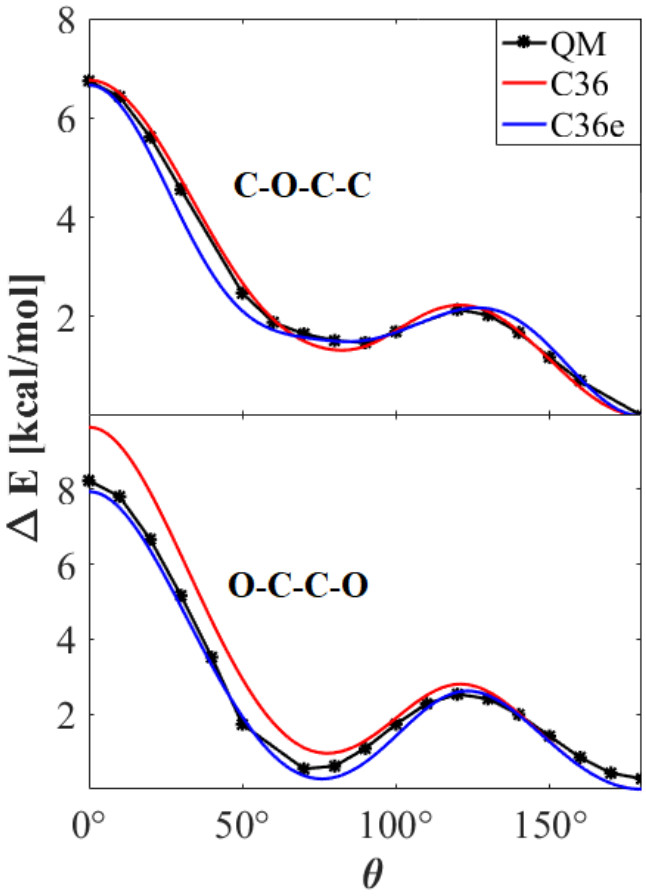

Figure 12. Potential energy scan about dihedrals of DEOE. C-C-O-C (top); O-C-C-O (bottom); MP2/cc-pVDZ//E^{int}[MP2:CC]. Other torsions remained *trans*.

While C36 is well-parameterized for C-O-C-C, it exhibits an elevated *gauche* well and cis barrier for O-C-C-O (at 70° and 0°, respectively). The elevated *gauche* well causes an underestimation of the *gauche* character of DEOE and DMOE. This is corroborated by Lee et al.,[157] who reported the TGT, TGG`, TTT, TTG, and TGG populations of DMOE at mole fractions of 1.0, 0.6, and 0.3. In C36, all XTX populations are over-estimated, whereas all XGX populations are underestimated, with the exception of slight over-estimation of TGT at 0.3 and TGG at 1.0 mole fraction. At all mole fractions, the TGG` populations were significantly under-estimated. In a DHPC bilayer, where an O-C-C-O chain connects the aliphatic lipid tails to the headgroup, this affects the tilt of the lipids.

C36e improves agreement with experiment for the densities of PEG (Table 9). The newly implemented LJ-PME (discussed in Chapter 2) increases ρ and has a greater effect on nonpolar species. Whereas PME enables swift estimation of long-range electrostatic interactions, CHARMM's use of Lorentz-Berthelot combination rules inhibited use of this method with long-range LJ interactions until recently.[180] Newly-implemented LJ-PME is accurate with anisotropic systems such as interfaces and allows use of a lower real-space cutoff for nonbonded interactions. Long-range LJ interactions significantly impact the ρ, isothermal compressibility, and liquid-vacuum surface tensions of nonpolar fluids. Recent investigation into liquid hexadecane indicates that use of LJ-PME with C36 improves agreement with experiment for liquid alkanes.[179] Table 9 shows that it also improves agreement with experimental ρ of ethers, most notably DMOE and DEOE, which have nonpolar, hydrocarbon end groups.

Table 9. Densities linear ethers (g/mL). Diethylene glycol (PEG2), triethylene glycol (PEG3), 1,2-diethyoxyethane (DEOE), and 1,2-dimethoxyethane (DMOE). Per cent difference from experiment is indicated to the right of the average and standard error for each entry.

	Exp. (T)	**C36**		**C36e**		**C36e, LJ-PME**	
PEG2	1.1197[193] (288.15 K)	1.01868 ± 0.0005	-9.02%	1.08376 ± 0.0004	-3.21%	1.09023 ± 0.0006	-2.63%
PEG3	1.1274[194] (288.15 K)	1.05511 ± 0.0004	-6.41%	1.09005 ± 0.0003	-3.33%	1.10134 ± 0.0005	-2.31%
DEOE	0.8484[193] (293.15 K)	0.8375 ± 0.0001	-1.28%	0.8192 ± 0.0001	-3.44%	0.8388 ± 0.001	-1.13%
DMOE	0.8628[194] (293.15 K)	0.8473 ± 0.0011	-1.80%	0.8331 ± 0.0007	-3.44%	0.8483 ± 0.0005	-1.68%

Table 10. ΔG_{hyd} (kcal/mol) of linear ethers. 1,2-diethoxyethane and 1,2-dimethoxyethane at 298.15 K. Per cent difference from experiment is indicated to the right of the average and standard error for each entry.

	Exp.	C36		C36e	
DEOE	-3.54[195]	-5.08 ± 0.13	-30.3%	-4.03 ± 0.07	-13.8%
DMOE	-4.835[195]	-4.57 ± 0.05	5.80%	-4.20 ± 0.09	13.17%

C36e also demonstrates the correct trend of increasingly favorable hydration (ΔG_{hyd}) for the shorter DMOE chain than for the longer DEOE (

Table ***10***). The original parameterization of DMOE included experimental ΔG_{hyd} as a target;[81] thus, C36 agrees well with ΔG_{hyd} of DMOE. However, ΔG_{hyd} of the longer chain DEOE is far too negative with C36. Experimentally, the longer chain solvates less favorably than the shorter chain, but C36 exhibits the opposite trend. C36e shows the correct trend and improved ΔG_{hyd} for DEOE, which is of greater interest as a model compound for the linkage of saturated ether lipids.

3.3.2. Ether-linked bilayer parameterization and comparison with experiment

C36e introduces parameters for the saturated ether lipid DHPC. Partial charge parameters, based on those of linear ethers, are shown in Figure 13. A critical comparison with experiment is the area per lipid, and this is considered first. Figure 14 shows the equilibration of A_l during each of three replicates of a DHPC bilayer at 333 K. As is evident from Table 11, A_l for C36e is substantially closer to experiment (+3% error) than C36 (-14%). Compared with C36, C36e exhibits a 13% increase in A_l and a 12% decrease in bilayer thickness. Each functional group comprising the lipid headgroup shifts about 1 Å closer to the bilayer center, and the bilayer hydrocarbon thickness decreases by 3 Å. Table 11 compares the resulting structural parameters of C36e with those of C36 and the experimental SDP.[155]

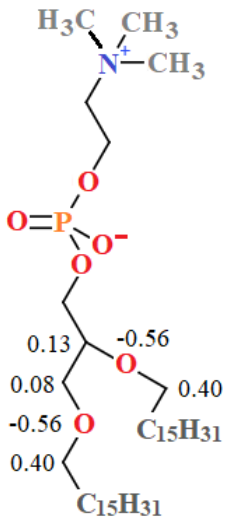

Figure 13. C36e partial-charge assignments for glycerol-ether linkage . Partial charges for the ether linkage of DHPC are shown in multiples of elementary charge, $+e$. Charges not shown for heavy atoms are identical to partial-charge assignments for the corresponding atoms of DPPC.

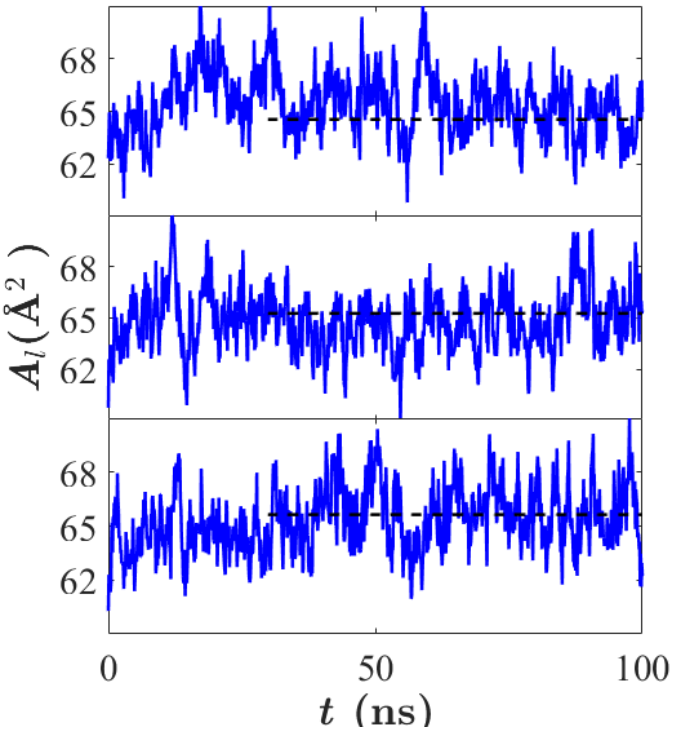

Figure 14. A_l as a function of time for three replicates of DHPC bilayers using C36e. Mean A_l, represented by a dashed line, was calculated after equilibration from 30 – 100 ns. Temperature = 333 K.

Table 11. Structural parameters of a DHPC bilayer. SDPs from experimental model and simulation.[a] "C36e, salt" simulations included 0.15 M NaCl**.**

	Temp. = 333 K				Temp. = 321 K	
	Exp.[155]	**C36**	**C36e**	**C36e, salt**	**Exp.[150]**	**C36e**
A_l **(Å^2)**	67.2	57.7 ± 0.3	65.4 ± 0.2	64.8 ± 0.1	65.1	63.6 ± 0.3
D_B **(Å)**	36.8	43.0	37.7 ± 0.3	37.65 ± 0.10	-	38.7 ± 0.1
$2D_C$ **(Å)**	27.1	31.8 ± 0.1	28.4 ± 0.1	30.25 ± 0.06	27.6	28.9 ± 0.1
D_{HH} **(Å)**	38	41.7 ± 0.1	38.7 ± 0.3	38.55 ± 0.12	38.2	39.0 ± 0.1
D_{H1} **(Å)**	5.4	4.93 ± 0.04	5.15 ± 0.06	4.19 ± 0.03	5.3	5.0 ± 0.1
z_{G1} **(Å)**	14.2	16.92 ± 0.03	15.60 ± 0.06	16.26 ± 0.03	-	15.88 ± 0.03
σ_{G1} **(Å)**	2.4	2.41 ± 0.01	2.71 ± 0.04	2.670 ± 0.01	-	2.77 ± 0.02
z_{G2} **(Å)**	19.2	20.94 ± 0.02	19.61 ± 0.06	19.74 ± 0.03	-	19.95 ± 0.03
σ_{G2} **(Å)**	2.6	2.39 ± 0.01	2.65 ± 0.04	2.677 ± 0.02	-	2.71 ±0.02
z_{G3} **(Å)**	20.1	22.15 ± 0.03	20.8 ± 0.07	21.08 ± 0.02	-	21.22 ± 0.03
σ_{G3} **(Å)**	2.8	3.13	3.20 ± 0.04	3.192 ± 0.01	-	3.25 ± 0.02

[a] A_l is the area per lipid. D_B, $2D_C$, D_{HH}, and D_{H1} are the overall bilayer thickness, the bilayer hydrocarbon thickness, the distance between electron density maxima, and the distance between the hydrocarbon surface and the maximum electron density in the same leaflet, respectively. Gaussian parameters (mean z_{GX} and standard deviation σ_{GX}) are listed for the glycerol-ether linkage (G1), phosphate and CH_2CH_2N (G2), and the trimethyl groups of the terminal choline (G3).

Table 11 also lists scattering parameters for DHPC with 0.15 M NaCl (4 NaCl molecules total). While most parameters are not significantly affected by salt, the bilayer hydrocarbon thickness ($2D_C$) increases by almost 2 Å (1 Å per leaflet). The peak position of the ether functional group (z_{G1}) also shifts outward along z by 0.66 Å, while other functional groups are not similarly affected. This indicates compaction of the G1 (ether) functional group into the headgroup in the presence of salt, as the hydrocarbon region of the bilayer expands slightly.

C36e exhibits experimental trends in the temperature dependence of A_l and bilayer hydrocarbon thickness ($2D_C$). Table 11 shows that experimental A_l for DHPC increases by 2.1 Å^2 when the temperature increases from 321 to 333 K; this is in near quantitative agreement with the 2.2 Å^2 obtained with C36e. C36e also matches the 0.5 Å decrease in $2D_C$ observed experimentally.

C36e shows closer agreement with experimental X-ray and neutron scattering factors than does C36 (

Figure **15** and Figure 16, respectively). The minima of the first three lobes of the X-ray form factors nearly match the experimental curve, indicating accurate A_l. The shape of the first lobe comports with experiment, and the relative heights of the second two lobes are within error margins. As would be expected from the underestimation of A_l, the parameter set based on C36 ethers produces form factors with inaccurate minima; i.e., $|F(q)| = 0$ are shifted to the left. This leftward shift is also found in the neutron form factors (Figure 16), especially at high percentages of D_2O. C36e shows excellent agreement with neutron form factors.

While positions of $|F(q)|$ minima are reliable, error in $|F(q)|$ heights are quite large for high values of wave vector q. In

Figure **15**, errors in height of $|F(q)|$ are approximately $0.5*|F(q)|_{\max}$ for values of $q > 0.4$ and $0.3*|F(q)|_{\max}$ for $0.25 < q < 0.4$.

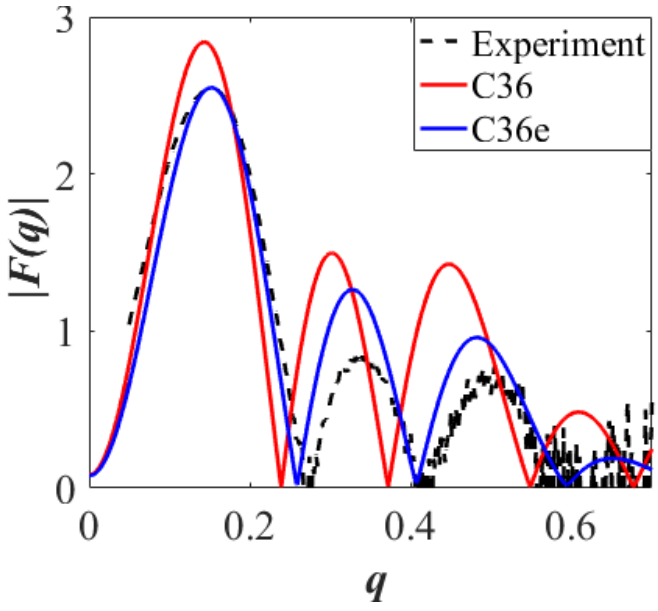

Figure 15. X-ray form factors for a DHPC bilayer at 333 K. Form factors from simulation and experimental form factors ($|F(q)|$) as a function of the total scattering vector q. For readability, error bars are not shown for experimental $|F(q)|$; they are approximately $0.5*|F(q)|_{\max}$ for values of $q > 0.4$ and $0.3*|F(q)|_{\max}$ for $0.25 < q < 0.4$.

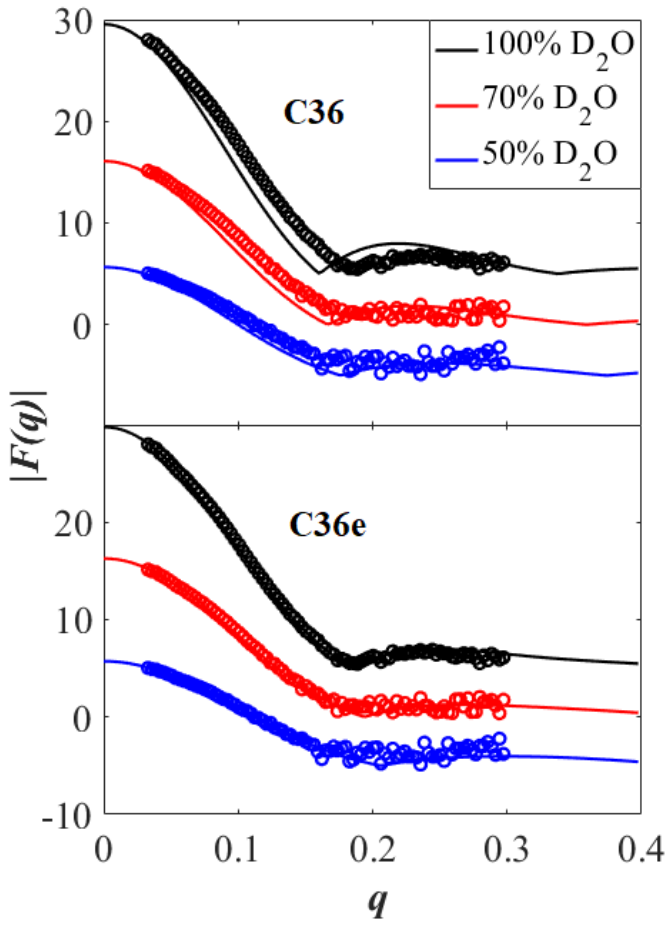

Figure 16. Neutron form factors for a DHPC bilayer at 333 K. $|F(q)|$ from simulation (solid lines) and experiment (open circles) in 100, 70, and 50 % D_2O as a function of the total scattering vector q. Form factors at 100 and 50 % D_2O are shifted vertically for clarity.

The electron density profiles of water and the G1 ether linkage group (Figure 17, top) indicate that water associates more with the G1 group in C36e: The water density profile intersects the peak of the G1 functional group. This is expected, because the increase in magnitude of the partial charge on the ether oxygen makes it more electronegative. The C36e water volume probability curve (Figure 17, bottom) nearly covers that of the G1 functional group, indicating water penetration to the z position of the ether linkage.

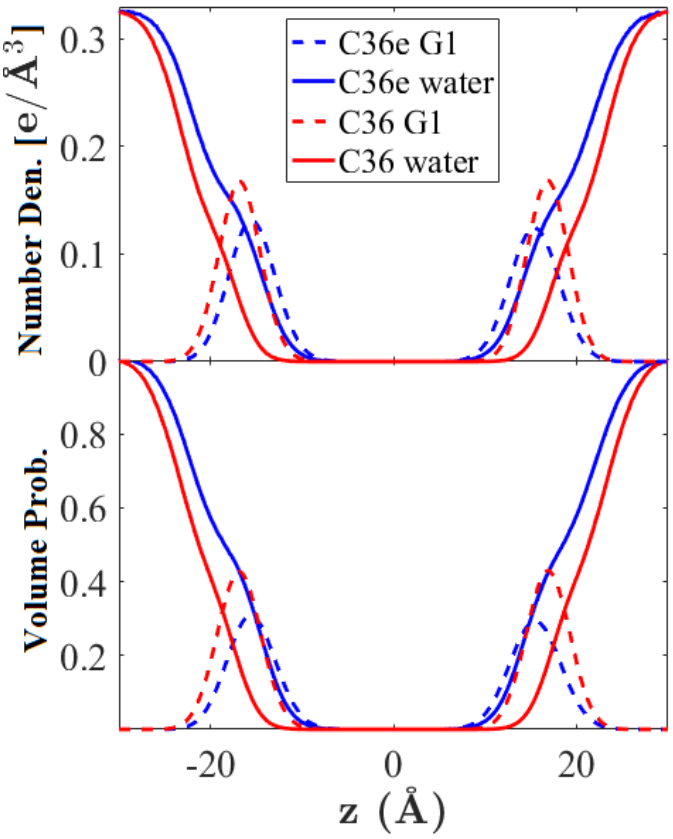

Figure 17. Electron number densities and volume probabilities for DHPC bilayers. Electron number densities (top) and volume probabilities (bottom) of the glycerol-ether linkage (G1) and water in a DHPC bilayer at 333 K.

C36e exhibits more instances of hydrogen bonding between the ether oxygen and water than does C36. Hydrogen bond lengths (oxygen to hydrogen) vary from 1.5 – 2.5 Å. Figure 18 shows the pair-correlation function for the ether oxygen-water hydrogen pair. The first peak positions (r_p) and number of waters in the first hydration shell (n_s) are $r_p = 1.73$ Å; $n_s = 0.94$ for C36e and $r_p = 1.86$ Å; $n_s = 0.43$ for C36. Thus, in C36e, each ether oxygen binds with a single water on average, whereas this association is less than half as likely with C36 ether parameters.

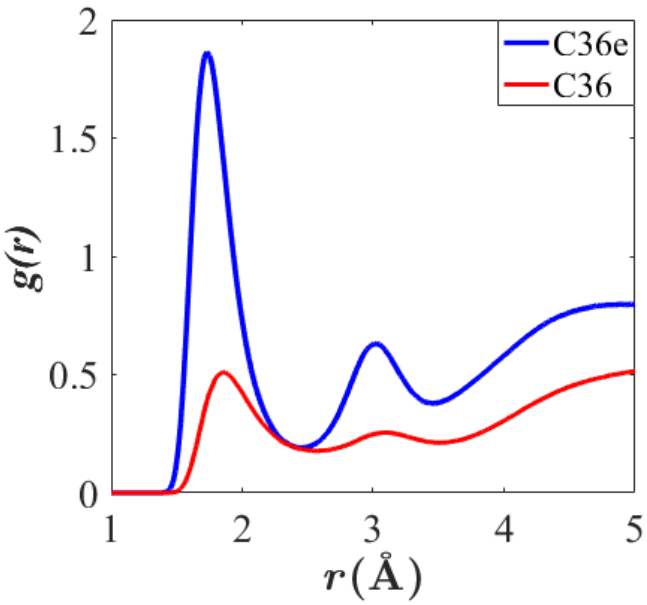

Figure 18. Pair-correlation function for the ether oxygen-water hydrogen pair . T = 333 K**.**

The volume probabilities of each functional group (defined in section 3.2.4) are compared in Figure 19. Note the total saturation of the headgroup region with water in C36e vs. the truncation in C36 at the glycerol-ether linkage. This causes A_l to increase with C36e. The resulting decrease in bilayer thickness is evident from the contraction along z.

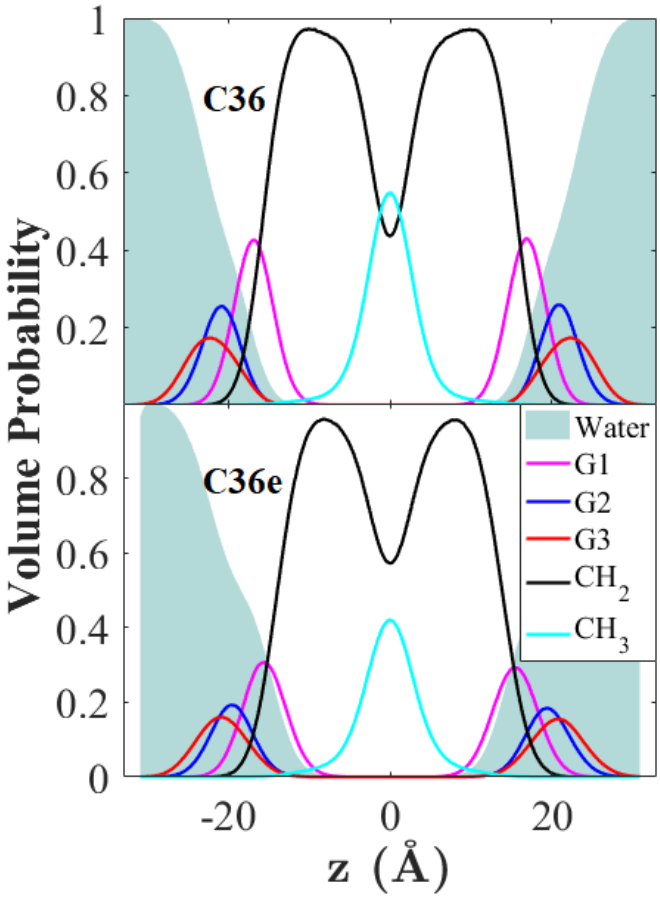

Figure 19. SDP of a DHPC bilayer at 333 K. Volume probabilities of selected functional groups.

3.3.3. Water organization in ether- and ester-linked lipids.

The effect of the ether linkage in DHPC, as compared with the more common ester linkage, is of interest as a well-localized chemical perturbation that affects physical properties. Like DHPC, DPPC has two 16-carbon saturated chains attached to the glycerol backbone; the only chemical difference between these two lipids is linkage between the glycerol backbone and hydrocarbon tails. Thus, the ether linkage in DHPC is responsible for its slightly larger A_l,[150, 155] lower water permeability,[150] and lower dipole potential.[151]

A recent all-atom MD study by Kruczek et al.[154] compared the organization of water in DHPC and DPPC bilayers. The authors proposed that increased water organization in the headgroup region of DHPC contributes to its relatively lower water permeability.

They found that waters near the DHPC headgroups were less mobile (lower lateral diffusion coefficient) and more ordered (higher autocorrelation times) than in a DPPC bilayer. Additionally, they found K_A to be higher for the DHPC bilayer, indicating it is more rigid. However, the parameterization scheme used in their study resulted in an underestimate of A_l for DHPC (sim. 60.0 Å^2 at 323 K; exp. 65.1 Å^2 at 321 K). Furthermore, in contrast to experiment, A_l for the simulated DHPC bilayer was lower than that of a DPPC bilayer at the same temperature. The condensation of the DHPC bilayer is consistent with both greater water organization and higher K_A.

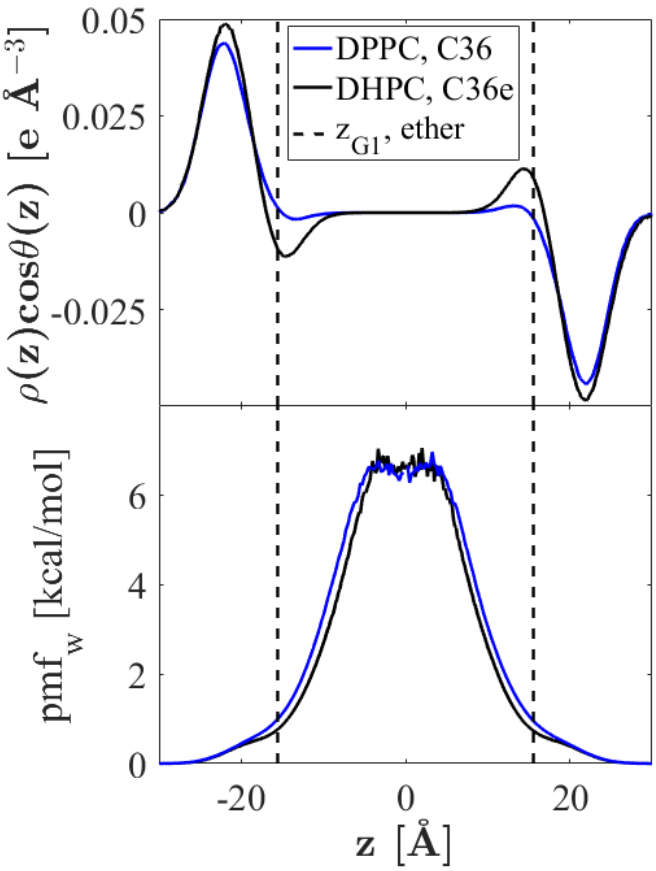

Figure 20. Water dipole orientation and potential of mean force at 333 K. Orientation of the water dipole with respect to the bilayer normal, scaled by the local water density (top). Water potential of mean force (bottom); region from [-10, 10] is not smooth due to infrequent permeation.

The present study examines water organization as a function of z, the position along the bilayer normal, using C36e parameters, which yield a higher A_l for DHPC than for DPPC. Figure 20 plots the density-weighted water dipole orientation, $\rho(z)\cos\theta\,(z)$, and water potential of mean force ($\mathrm{pmf_w}$). Indeed, waters in the headgroup region of DHPC display greater water dipole organization, particularly around the terminal choline ($z = 20.8$) and ether linkage (vertical black dashes). This is indicated by the greater magnitude of $\rho(z)\cos\theta(z)$. The $\mathrm{pmf_w}$ are nearly identical except for compaction along z observed with DHPC due to its greater A_l. The increased organization around the ether linkage is counter-intuitive because the ether oxygen is less electronegative than the carbonyl oxygen of DPPC, as determined from the partial-charge assignments (-0.56e ether oxygen in DHPC, -0.63e carbonyl oxygen in DPPC). However, perhaps due to steric hindrance arising from close proximity with the ester oxygen, the carbonyl oxygen in DPPC does not associate as strongly with water as the ether oxygen in DHPC. Figure 21 plots the pair-correlation functions $g(r)$ of various lipid oxygens with water hydrogens. The peak position (r_p) of the correlation function for the DHPC ether oxygen with water is the smallest, indicating the shortest bond association length; the integral of this peak is also the greatest, indicating the greatest number of associations per ether oxygen ($r_p = 1.73$ Å; $n_s = 0.94$). The carbonyl oxygen of DPPC has a comparable but slightly lesser interaction with the water ($r_p = 1.79$ Å; $n_s = 0.85$), and the ester oxygen of DPPC does not appear to associate strongly with water, despite its significant partial charge (-0.49e).

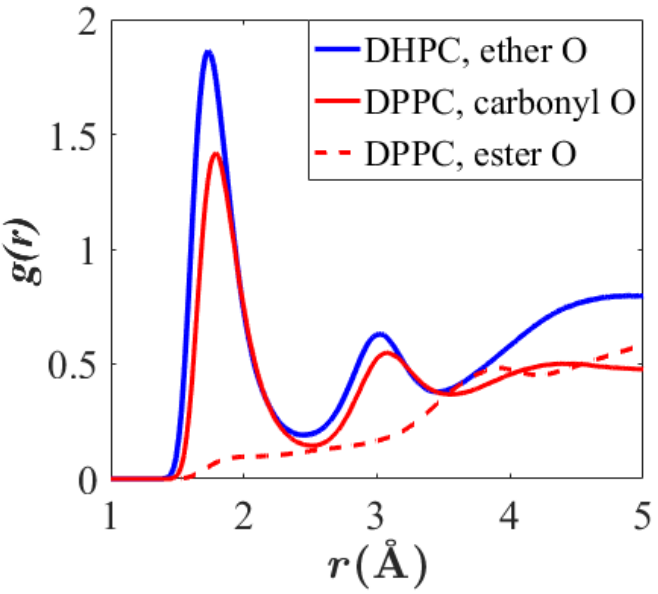

Figure 21. Pair-correlation function for various lipid oxygens with water hydrogen. T = 333 K.

The previously-mentioned MD study by Kruczek et al.[154] found the artificially condensed DHPC bilayer to have a significantly larger K_A than DPPC (418 dyn/cm for DHPC and 359 dyn/cm for DPPC), but the value found for DPPC at 321 K is considerably larger than the experimental value at a nearly equivalent temperature (231 dyn/cm at 323 K).[26] Parameterization of DPPC in C36 yields A_l and K_A in good agreement with experiment at 323 K; A_l matches the experimental value of 63.0 and estimates of K_A are 210 and 230 dyn/cm for systems of 648 and 72 lipids, respectively.[92] C36 DPPC therefore provides a more reliable comparison to DHPC with C36e. Results, listed in Table 12, indicate that K_A of DHPC is not significantly different from that of DPPC (the 95% confidence intervals are approximately twice that of the standard error). Thus, the claim by Kruczek et al.[154] that increased stiffness of DHPC bilayers relative to DPPC contributes to decreased permeability is not supported here. The increase in K_A observed in that study likely resulted from the relatively low A_l.

The comparable values for K_A listed in Table 12 imply that the ether linkage does not contribute to the increased membrane stiffness of observed in archaea.[196] In addition to the ether linkage, archaeal membranes contain methylated tails composed of repeating 5-carbon isopranoid or isoprenoid chains. Acyl chains with this structure have been shown to increase bilayer stiffness in simulations with C36 using ester-linked lipids.[197]

Table 12. Compressibility moduli and area per lipid of DHPC (C36e) and DPPC (C36)

	DPPC		**DHPC**			
	Exp. [198, 199]	**C36**	**Exp.**[150]	**C36e**	**Exp.**[155]	**C36e**
T (K)	323	333	321	321	333	333
K_A **(dyn/cm)**	231	244 ± 16	-	214 ± 18	-	230 ± 15
A_l **(Å^2)**	63 ± 1	63.2 ± 0.3	65.1	63.6 ± 0.3	67.2	65.3 ± 0.2

The electrostatic potential drop, $\Delta\Psi$, as a function of the *z* position along the bilayer normal, is plotted in Figure 22 for DHPC and DPPC at 333 K. $\Delta\Psi$ determines the electric field strength inside the membrane and has been shown to affect the conformation of ion-translocating proteins.[200] However, precise experimental values of $\Delta\Psi$ for bilayers remain controversial because direct measurement is not currently possible.[200] Experimental estimates vary significantly depending on methods. Two studies using different methods agree that DHPC bilayers should have a lower $\Delta\Psi$ than DPPC bilayers by about half.[151, 201]

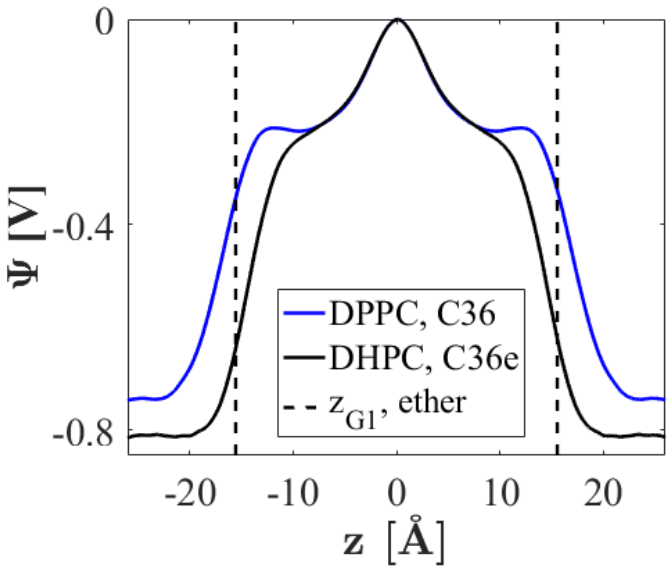

Figure 22. Electrostatic potential drops for DHPC and DPPC bilayers at 333 K.

As was noted previously,[34] C36 systematically over-estimates ΔΨ across lipid bilayers according to consensus of experimental values. Experimental estimates of ΔΨ for DPPC range from 220 – 280 mV,[200] while results with C36 are closer to 800 mV from the interleaflet region to water. C36e yields a slightly greater ΔΨ for DHPC, contrary to experimental estimates. A previous FF adaptation for ether-DPhPC bilayers, developed by Shinoda et al. for use with CHARMM27,[156] successfully yields lower ΔΨ for ether-DPhPC than for ester-DPhPC, but there are some issues with this FF. First, as with C36, the magnitude of ΔΨ for both lipids is significantly higher than experimental predictions, with ΔΨ of about 500 mV for ether-DPhPC and 1000 mV for ester-DPhPC, over four times higher than the experimental prediction.[202] Secondly, the ether-DPhPC bilayer has lower A_l (74.1 Å^2) than the ester-DPhPC bilayer (77.7 Å^2). This is likely incorrect, as DPhPC is identical to DPPC except for methylated tails, and the ether linkage is expected to increase A_l.[150, 155] Pan et al.[155] adapted these parameters for a DHPC bilayer and found that, indeed, the A_l for DHPC was 9 Å^2 too low, precluding use of the biologically-relevant NPT ensemble. Charge parameters for the ether linkage used in these studies were lower in

magnitude for ether oxygens and bonded carbons than C36e assignments. Results for the C36 PEG-based charge set in Table 11, also with decreased polarity in the ether linkage, yield DHPC A_l that is again 10 Å^2 too low. It is reasonable to assume from the poor results obtained with these alternate charge sets and from QM ESP results for linear ethers (Figure 10) that, while such reduced polarity may achieve a lower dipole potential for DHPC bilayers, it does not accurately represent the ether linkage. The inability of C36 to produce accurate $\Delta\Psi$ more likely results from underestimation of the dielectric constants of nonpolar liquids (models of lipid tails) in additive force fields.

The present study prioritizes agreement with bilayer structural parameters. While it is probable that use of a polarizable FF, such as the CHARMM Drude FF,[73, 74, 76] would yield more experimentally-consistent values for $\Delta\Psi$, adjustments to the Drude FF for lipids would be necessary to compare DPPC and DHPC.

3.4. Extension of C36e parameters to plasmalogens

DHPC differs from the experimentally ubiquitous DPPC only it the ether linkage. It serves as a chemical perturbation for investigating effects of the ether linkage; but DHPC is not found in the human body. In a study not yet published, ether linkage parameters are applied to a lipid prevalent in human brain tissue: ethanolamine plasmalogen. Plasmalogens, which are characterized by a vinyl ether bond in position *sn*-1 to an alkenyl group, are present in high concentrations in neural tissues.[158-161] This section introduces parameters for phosphatidylethanolamine plasmalogen (PLAPE).

Linear vinyl ethers are logical models for the vinyl ether linkage in plasmalogens. QM results for partial atomic charges of linear vinyl ethers are shown in Figure 23. While carbons bonded to ether oxygens carry substantially positive partial charge if no vinyl

group is present, the presence of a vinyl group reduces the positive charge of the bonded carbon. As with saturated linear ethers,[72] partial charges on carbons then alternate positive/negative moving outward from the ether oxygen on both ends of 1-ethoxypropene.

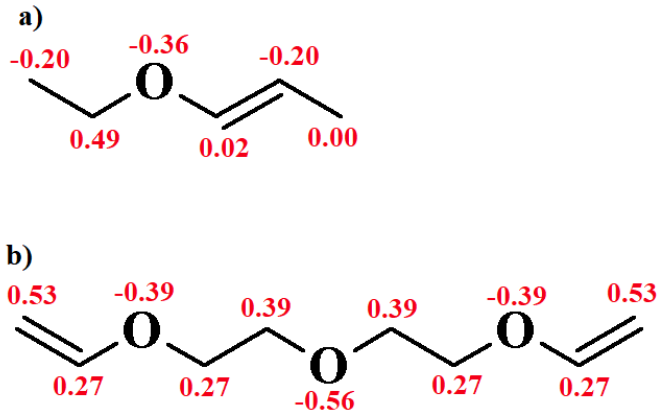

Figure 23. Partial atomic charges for model vinyl ethers from QM. Results for (a) 1-ethoxypropene and (b) diethylene glycol divinyl ether. Units of elementary charge, $+e$, averaged for symmetry where applicable.

Partial charge assignments for the vinyl ether moiety of PLAPE and model compound 1-ethoxypropene are shown in Figure 24. The partial charge on the C3 carbon of PLAPE is borrowed from C36 lipid assignment for the glycerol linkage,[34] and the ether oxygen and bonded carbon of the tail received charges consistent with the recently-published linear ether FF.[72] In this study, it was found that reducing C3 glycerol charge relative to QM results for linear ethers allows more water to penetrate the bilayer, improving agreement with experimental surface area per lipid. Because the glycerol linkage is branched rather than linear, borrowing partial charge from C36 results tuned specifically to the glycerol region of lipids is chemically consistent.

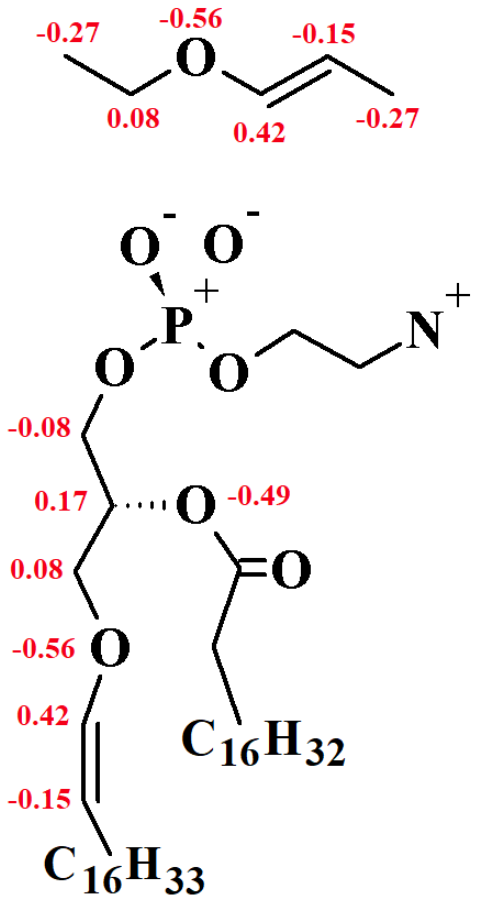

Figure 24. Partial charge assignments for vinyl ethers and PLAPE. (top) 1-ethoxypropene; (bottom) PLAPE. Units of elementary charge, $+e$. Charges on heavy atoms shown. Other charges for PLAPE are identical to C36 assignments for DOPE. 1-ethoxypropene charges were taken directly from the vinyl region of PLAPE as a model for fitting dihedral parameters, so this should not be considered a stand-alone model.

An alternate charge set was tested for PLAPE in which -0.36 was assigned to the ether oxygen, the attached vinyl carbon was neutral, and the second vinyl carbon of the tail was assigned -0.20, consistent with QM results in Figure 23, but this set did not show good agreement with experimental form factors, so the charge set in Figure 24 was chosen.

The model for 1-ethoxypropene in Figure 24 was used to fit appropriate dihedrals. Therefore, the charges were taken directly from the vinyl region of PLAPE. It should not be considered a stand-alone model for 1-ethoxypropene.

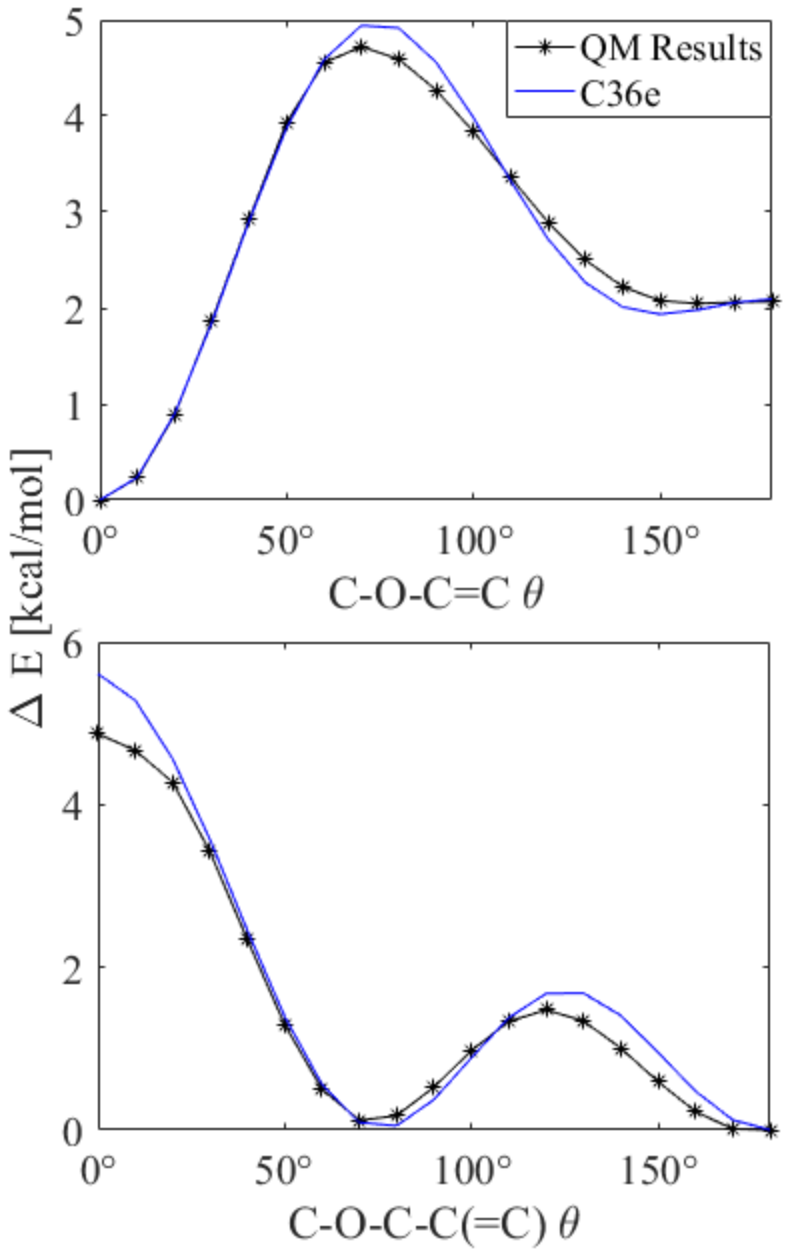

Figure 25. Potential energy scan about dihedrals of 1-ethoxypropene. (top) C-O-C=C; (bottom) C-O-C-C(=C); QM using MP2/cc-pVDZ//E^{int}[MP2:CC] plotted with results after dihedral fitting. Other torsions remained *trans*.

Figure 25 plots results for the QM potential energy scan about the C-O-C=C and C-O-C-C(=C) dihedrals of 1-ethoxypropene. The minimum of C-O-C=C occurs at 0°, and inversion of the potential energy landscape of typical C-C-C-C or C-O-C-C dihedrals which have an energy maximum in the same dihedral configuration. Final torsional fits

agree well with the QM minima and local minima for both dihedrals, indicating accurate representation of the torsional energy landscape at biological temperatures.

A_l for different POPC to PLAPE ratios at different temperatures are reported in Table 13, courtesy of Valeria Zoni at Universite de Fribourg (further results for POPC:PLAPE mixtures to be published soon). As expected, with an increase in temperature, the A_l also increases, but irrespective of composition; a 7 degree increase in temperature results in ~4 Å^2 increase in A_l. At increasing concentration of PLAPE, the overall A_l slightly decreases. This is likely due to the ability of the PE headgroup to form hydrogen bonds and thus have a more tightly packed membrane.

Table 13. Overall A_l (Å^2) from simulation for POPC/PLAPE mixtures.

Temp.	**Ratio of POPC/PLAPE**		
	2:1	1:1	1:2
303 K	61.3±0.5	60.2±0.2	59.5±0.3
310 K	65.4±0.1	64.5±0.1	63.5±0.1

X-ray form factors from simulation and experiment are compared in Figure 26. The simulation results for the second half of the second lobe, subsequent crossing points, and third lobe are in good agreement with experiment. Crossing points are important metrics for A_l and thus it appears that our estimates in lipid packing are reasonable, although the first crossing point is shifted to the left, indicating slight underestimation of A_l.

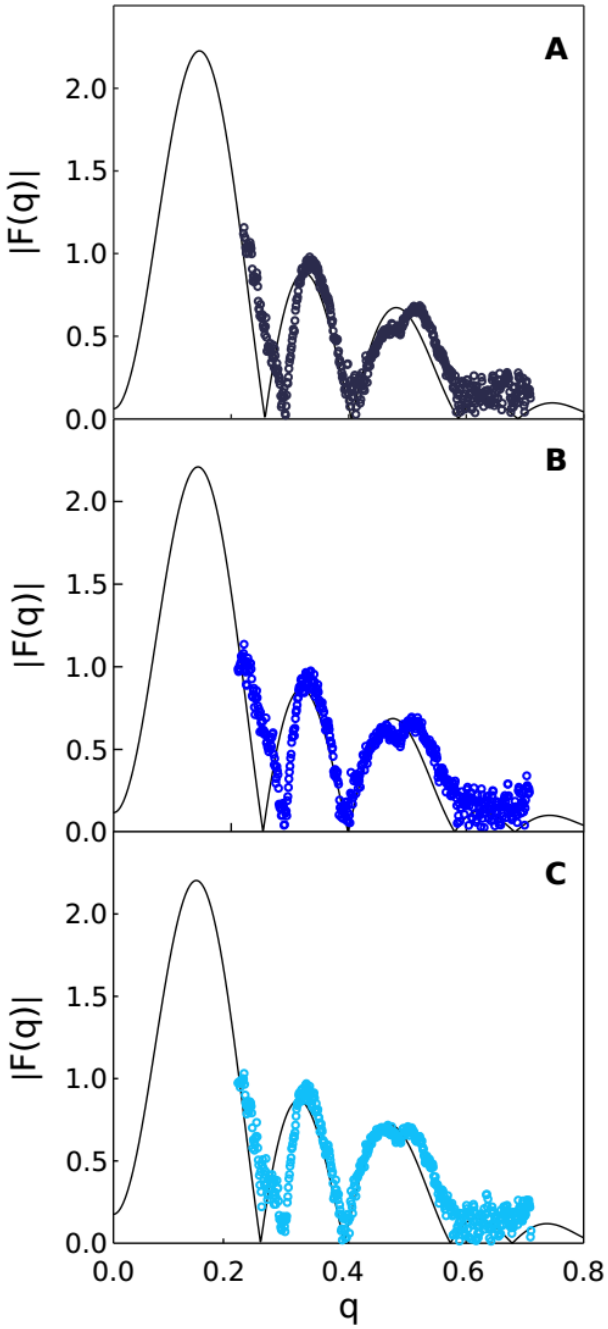

Figure 26. X-ray form factors for bilayers containing PLAPE. Obtained from simulations at 310K (black line) of different POPC/PLAPE mixtures, (A) 2:1, (B) 1:1 and (C) 1:2. The data are compared with experimental results (open circles). The experimental X-ray data are scaled to match the height of the second and third lobes.

3.5. Discussion

Changing the partial-charge assignments and associated dihedral parameters for linear ethers improves agreement with the QM dihedral potential energy landscape for 1,2-diethoxyethane (DEOE), while at the same time bringing free energy of hydration in closer agreement with the experimental value. Applying these new C36e parameters to small chains of polyethylene glycol considerably improves agreement with experimental densities.

Application of C36e parameters to the glycerol-ether linkage of a DHPC bilayer required a reduction in magnitude of partial charge on carbons in the glycerol chain to allow for deeper water penetration. This is consistent with charge assignments for glycerol in the similar, but ester-linked lipid, DPPC. The resulting structure of a DHPC bilayer shows close agreement with experimental scattering factors and improved agreement of scattering density parameters, including surface area per lipid. C36e accurately reproduces the experimental temperature dependence of neutron/X-ray form factors.

Examination of water-lipid associations reveals that water penetrates to the level of the ether linkage (Figure 17). Organization of the water dipole in the vicinity of the ether linkage is higher in a DHPC bilayer than in a DPPC bilayer around its ester linkage (Figure 20, top). Additionally, water associates more strongly with the ether oxygen in DHPC than with either the carbonyl oxygen or the ester oxygen in DPPC (Figure 21). The strong association between the ether oxygen and water, and the tendency of the ether oxygen to orient the water dipole, both increase the organization of water around the ether linkage. This increase in water organization occurs despite the greater surface are per lipid and

comparable area compressibility as compared with the ester-linked DPPC bilayer (Table 12), and is a likely explanation for the lower water permeability of the ether-linked DHPC.

The surface area per lipid decreases only slightly in the presence of 0.15 M NaCl (Table 11). The overall bilayer thickness is not significantly affected, but the bilayer hydrocarbon thickness increases by 1.8 Å, and the position of the glycerol and ether linkage functional group shifts outward from the bilayer center. This indicates compaction of the headgroup region in the presence of sodium ions.

For practical use in modeling mammalian membranes, ether linkage parameters were also adapted for PLAPE plasmalogen with satisfactory reproduction of experimental X-ray scattering factors; however, it is likely A_l of POPC/PLAPE mixtures is slightly underestimated with this parameter set. In simulation, A_l is seen to increase with the ratio of POPC/PLAPE, likely due to hydrogen bond capabilities of the PE headgroup.

Systematic under-estimation of area per lipid in previous MD studies of ether-linked bilayers has undermined comparison of the ester and ether linkages. C36e yields close agreement with experimental scattering factors for a DHPC bilayer in the NPT ensemble, making this comparison possible. The ether linkage is responsible for the experimentally lower water permeability of DHPC relative to DPPC[150] and is thought to contribute to the resilience of archaeal membranes over a range of pH.[196] C36e enables modeling of the effects of the ether linkage on membrane water permeability and stability over a range of salinities, pressures, and temperatures.

Chapter 4. Investigating Lipid-Ion Interactions: Isothermal Titration Calorimetry, Small Angle Neutron Scattering, and *Ab Initio* Interaction Energies Guide Additive FF Development.

4.1. Introduction

The electrolyte environment of biomembranes *in vivo* is characterized by varying concentrations and species of ions. Separating aqueous solutions with different salt concentrations is a primary function of membranes. Ions, in turn, interact with the polar headgroups of lipids to impact membrane assembly and affect structure and dynamics. Ions in solution can influence lipid phase transitions, modify the membrane potential, and alter the dynamics of the hydration layer, to give a few examples.[203] Sections 4.2 and 4.4 discuss the development of interaction parameters for beryllium with phosphatidylserine. Sections 4.3 and 4.5 discuss potassium interactions with polyethylene glycol.

A published study included[204] in this chapter investigates interactions between Be^{2+} and the negatively-charged headgroup phosphatidylserine (PS). More prevalent divalent ions such as calcium and magnesium play many functional roles in biological systems. While permanently associated ions are typically involved in catalysis,[205] weaker and more transient associations of divalent ions (primarily Ca^{2+}) with proteins and lipids play critical roles in cell adhesion,[206] blood clotting, and calcification[207] as well as cell recognition and signaling reactions.[208] Toxicity of some polyvalent ions has been linked to their ability to interfere with calcium-dependent processes. Toxic pro-inflammatory effects of Be^{2+} are proposed to be mediated not only by abnormal binding to specific MHC-II alleles,[209, 210] but also by its ability to outcompete Ca^{2+} on the surface of PS domains and thus negatively affect recognition of this signaling lipid by macrophages removing apoptotic cells in a non-inflammatory way.[23] While both Ca^{2+} and Be^{2+} interact strongly with PS, the smaller

atomic radius of Be^{2+} allows it to outcompete Ca^{2+} and bind with greater affinity to DOPS liposomes (with equilibrium binding constants $K_{eq} \sim 3 \cdot 10^4$ M^{-1} for Ca^{2+} and $\sim 3 \cdot 10^5$ M^{-1} for Be^{2+}).[23] The smaller size of the Be^{2+} ion also stipulates a small coordination number (n=4)[211] which prevents this ion from adequately substituting Ca^{2+} in physiological reactions between proteins and lipids.[205] The use of molecular dynamics simulations for studies of these events is often ineffective due to either imprecision or absence of force field parameters that would predict realistic affinities, ionic competition, and ion coordination by specific chemical groups.

Interactions of divalent ions with polar electronegative groups present a challenge in molecular dynamics simulations because in pairwise additive non-polarizable force fields, electrostatic interactions are effectively magnified at close range by the inability of atomic electron densities to adjust to the ambient electric field. Salt solutions therefore can be simulated in two regimes: near infinite dilution, in which ionic interactions are shielded, and high concentrations in which close-range interactions are common and can result in unnatural clustering.[212-214] Special adjustments are required to correct for over-binding artifacts.

The parameters of the LJ potential (eq. 2) for individual ions in additive force fields are developed to reproduce experimental data in concentrations around 0.5 to 5 M.[212, 213] Interaction potentials describing cation-anion pair interactions and ionic interactions with polar species can be adjusted for atoms of species i and j by changing of the LJ interaction parameters $r_{ij}^{\min}$ and ε_{ij}. Historically, changing only $r_{ij}^{\min}$ has been preferred by the CHARMM development community. For example, it has been shown that in sodium acetate solutions of more than 1 M concentration, Na^+ and acetate over-bind unless $r_{ij}^{\min}$ is

increased.[213] Because ions are more concentrated near a charged surface, they are prone to over-bind to charged lipid headgroups in bilayer and monolayer simulations. The artifacts are more severe when the simulated systems contain ions with strong interaction potentials, such as divalent ions especially with small atomic radii.

With the goal of investigating Be^{2+} binding to PS and its cognate receptors using all-atom molecular dynamics, in this iterative study we first find LJ parameters to describe the interaction of Be^{2+} with water. *Ab initio* data for ion-monohydrate interactions is considered, as well as solution properties including free energy of hydration ΔG_{hyd}, coordination number, and radial distribution function $g(r)$ peak position. Isothermal titration calorimetry (ITC) experiments are then used to characterize the association of Be^{2+} with model substances emulating ion-binding groups in PS. Solutions of sodium acetate or dimethyl phosphate (DMP) are titrated into $Be(SO_4)_2$ solutions. Resulting binding parameters are used to fit LJ interaction parameters $r_{ij}^{\min}$ between Be^{2+} and the free carboxylate and phosphate oxygens, yielding improved agreement with experimental free energy of binding.

The $r_{ij}^{\min}$ interaction parameters between Be^{2+} and phosphoryl and carboxylate oxygens are then used in DOPS monolayer simulations. Surface pressures of DOPS monolayers, found from Langmuir experiments, are dependent on salt species and concentration. Relative to Ca^{2+}, which has a larger atomic radius, Be^{2+} has a stronger compacting effect on DOPS monolayers in these experiments.[23] Revised interaction parameters for Be^{2+} with phosphoryl and carboxylate oxygens reproduce experimental surface tensions for DOPS monolayers, verifying the trend of compaction of the monolayer in the presence of Be^{2+} relative to K^+.

A later study (in progress) investigates the effect of K^+ on the radius of gyration (R_g) of PEG. New data from small angle neutron scattering (SANS) experiments, presented in subsection 4.5.2, show that R_g for solutions of 29-mer PEG decreases as a function of KCl concentration. There are multiple possible explanations for this dependence. In high concentrations of KCl, interactions between partially negative ether oxygens and positively charged K^+ might cause PEG to exhibit more *gauche* character, as has been demonstrated by the formation of crown ethers in solutions of longer PEG polymers and KCl.[215] Scattering of associated waters or ions may also affect experimental estimates of R_g in ways that are concentration dependent.

A package developed by Jochen Hub and colleagues computes SANS and small angle X-ray (SAXS) scattering curves from all-atom simulations using a Fourier transform of neutron or electron densities, respectively.[216, 217] In this way, contributions from the hydration shell are included in estimates of R_g, allowing direct comparison with experiment. Simulation results presented in section 4.5.2 show that, in the absence of KCl, C36e parameters presented in the previous chapter yield excellent agreement with experimental R_g for 29-mer PEG. However, in 3 M KCl solutions, R_g is underestimated. The separation distances of various atom pairs, including water-water and PEG oxygen/K^+, are computed and the fraction of *gauche* dihedrals in PEG is calculated to determine the cause of this discrepancy.

With the goal of investigating new parameterization methods for close lipid-ion interactions, we sought to characterize the interaction energy landscape of K^+ with the ether oxygen of PEG. Interaction energies were computed using QM calculations in implicit solvent, varying the separation distance between K^+ and the ether oxygens. The QM data

are compared with simulation results for various LJ ($\varepsilon_{ij}, r_{ij}^{\min}$) pairs. However, resulting K^+/ether oxygen interaction parameters do not affect R_g of PEG due to the weak nature of this interaction in solution. Accounting for the *gauche* character and end-to-end length of PEG reveals that the reduction of R_g in the presence of KCl can be attributed to changes in PEG conformation, perhaps due to charge shielding of the polar ether oxygen.

Section 4.2 describes methods used to investigate Be^{2+}-PS interactions; section 4.3 describes methods employed in studying K^+ interactions with the ether oxygen in PEG. There is very little overlap in these methods, as each study offers a unique perspective on ion-oxygen interactions. Section 4.4 presents results for Be^{2+}-PS interactions and DOPS monolayer simulations, and Section 4.5 for K^+ interactions with PEG. Section 4.6 discusses the significance of results and future directions.

4.2. Methods for Investigating Be^{2+} Interactions with PS

4.2.1. ITC experiments with Be^{2+} and PS components.

ITC experiments were used to find the equilibrium binding constants between Be^{2+} and PS component molecules. Solutions of $BeSO_4$, dimethyl phosphate ($C_2H_7O_4P$, DMP), or sodium acetate ($NaCH_3COO$, NaAc) were prepared in 10 mM KCl buffered with 2 mM Tris-HCl (pH 7.3) as a background electrolyte. Titrations were carried out on a MicroCal VP-ITC microcalorimeter at 30^{o}C using injections of 10-15 µl separated by 200-300 s time intervals. To avoid subtracting large enthalpies associated with dilution of a divalent ion, solutions containing the small molecule were the titrants and the solutions containing Be^{2+} were in the chamber initially in all experiments. 4 mM DMP or 20 mM NaAc were titrated into a 2 or 5 mM $BeSO_4$ solution for DMP or NaAc experiments, respectively. Fitting of the integrated thermograms was done with MicroCal Origin software's one-site fitting

routine[218] to extract a single binding constant for each reaction. For each experimental setup, a control was performed in which the titrant was injected into pure buffer and the resulting energy subtracted before fitting was performed. Each experiment was repeated three times, and error estimates were calculated from the standard error among trials.

4.2.2. Molecular dynamics simulations.

Standard C36 parameters were used for DOPS and DMP.[34] These can be found in the C36 lipid FF files. C36e parameters introduced in the previous chapter[72] were used for PEG and DEOE. Two sets of parameters were tested for acetate. The first is the standard model for soluble acetate found in the CHARMM CGEN force field files,[135] referred to hereafter as "acetate, CGEN FF." Because partial charge assignments for this model differ from those in the DOPS model, a new model for soluble acetate was developed that borrows lipid atom types and partial charges from DOPS, hereafter referred to as "acetate, lipid FF." Only interaction parameters developed for the lipid FF were tested in DOPS monolayer simulations.

The TIP3P water model[54] as modified[55] for CHARMM was used as the solvent. For solution simulations requiring counterions, revised Na^+ ion LJ interaction parameters for oxygen atoms occurring in carboxylate, carboxylate ester, and phosphate ester groups were employed.[213]

Simulations of Be^{2+} in solution with the desired small molecule were used to observe and count common configurations. Be^{2+}-small molecule pairs simulated include: Be^{2+} with DMP and Be^{2+} with acetate. Each system contained 60 small molecules, 20 divalent ions, 20 Na^+ ions to keep the system electroneutral and between 12,500 and 13,500 water molecules. Simulations of Be^{2+} with acetate were run for 40 ns, and of Be^{2+} with

DMP for 330 ns, at 303.15 K in the constant number, pressure, and temperature (NPT) ensemble for comparison with ITC data. Equilibration of the systems, determined by stability of the divalent ion/oxygen pair correlation functions, occurred by 30 and 5 ns for the Be^{2+}-acetate systems with default and adjusted parameters, respectively; and by 40 and 165 ns for the Be^{2+}-phosphate systems with default and adjusted parameters, respectively. Only equilibrated segments of trajectories were used to compute configuration probabilities. See supplemental information Figs. S1, S2, and S3 for plots demonstrating stability of the pair correlation functions for systems with revised interaction parameters.

Simulations of aqueous $BeCl_2$ to obtain the radial distribution functions $g(r)$ and evaluate coordination numbers and $g(r)$ peak positions were run at 298.15 K and contained between 570 and 580 TIP3P waters, 55 Be^{2+}, and 110 Cl^- distributed using random replacement. Resulting 5.3-molal solutions matched the concentration of a comparison X-ray scattering experiment used to generate the total $g(r)$.[219] In the present study, two 30-ns simulations from different starting configurations were run at standard temperature and pressure, with the last 10 ns evaluated and error computed from the standard error in measurements from the two simulations.

Simulations of pure DOPS monolayers contained 40 lipids/leaflet, 40 divalent ions or 80 K^+ ions, and 50 waters/lipid. Initial configurations were assembled using the CHARMM-GUI *Membrane Builder*,[182, 220-222] which splits a single bilayer into two oppositely-oriented leaflets separated by water. Two replicates each of DOPS monolayers with Be^{2+} or K^+ at 65.3 and 71.6 $Å^2$/lipid were run for 150 ns in NAMD[185] using the constant number, volume, and temperature (NVT) ensemble to simulate the Langmuir trough experiment, with T = 295.15 K for comparison with experimental results.[23] After

30-ns equilibration, monolayer surface tensions (γ_{m}), and residence times and pair correlation functions $g(r)$ of Be^{2+} with phosphate, carboxylate, and water oxygens were computed from 30 - 150 ns. To compute γ_{m}, pressure output was saved every 1,000 steps.

All solution ion-small molecule simulations and monolayer simulations were run in NAMD[185] in the NPT ensemble as described in Sec. 3.2.4. The C36 force field[34] was used with added Lennard-Jones (LJ) parameters for Be^{2+} and LJ interaction parameters between Be^{2+} and the deprotonated oxygen of PS component molecules.

All pair correlation functions $g(r)$ were computed from trajectories using the program Visual Molecular Dynamics (VMD).[223] Plots of $g(r)$ were normalized in VMD unless indicated otherwise. If not normalized, the raw histogram data was plotted for comparison of relative $g(r)$ peak heights of different species pairs.

4.2.3. Free energy calculations between Be^{2+} and PS components.

FEP simulations (described in Sec. 3.2.3) were used to calculate the free energy of hydration (ΔG_{hyd}) of Be^{2+}, and the free energy of binding between Be^{2+} and small molecules in a given configuration (ΔG_{c}). To calculate ΔG_{hyd}, a Be^{2+} ion in a vacuum was simulated for the initial stage of the FEP thermodynamic cycle, and in the aqueous phase for the final stage. When calculating free energies of hydration of highly charged species, the potential arising from crossing the liquid-vacuum interface, called the Galvani potential, is expected to contribute significantly:[224-226]

$$\Delta G_{\mathrm{hyd}} = \Delta G_{\mathrm{intrinsic}} + zF\Phi. \quad (29)$$

Here, $\Delta G_{\mathrm{intrinsic}}$ is the thermodynamic work required to move an ion from the vacuum state into the interior of pure water, and $zF\Phi$ is the work needed to cross the liquid-vacuum interface; z is the ion's charge, F is Faraday's constant, and Φ is the Galvani

potential of the liquid, which has been calculated to be -0.51 V for TIP3P at standard temperature and pressure.[225] Thus, values reported for ΔG_{hyd} of Be^{2+} include $\Delta G_{\mathrm{intrinsic}}$ (calculated from FEP simulations) and a correction of -11.76 kcal/mol to account for the Galvani potential.

To calculate ΔG_{c} for a given configuration, Be^{2+} in the aqueous phase was simulated for the initial stage, and in an appropriate binding configuration for the final stage. Standard errors between free energies calculated from at least three separate thermodynamic cycles are reported. Initial coordinates of the bound configurations for calculating ΔG_{c} were taken from the equilibrated solution simulations used to count probabilities. Water boxes were pre-equilibrated and contained between 350 and 380 waters.

4.2.4. Fitting Lennard-Jones parameters for Be^{2+} in water.

This subsection introduces CHARMM LJ parameters for Be^{2+} based on the structure and energetics of the ion's interactions with water. Target experimental data for the interaction of Be^{2+} with bulk water included the free energy of hydration,[227] coordination number,[211] and peak position of the radial distribution function, $g(r)$.[219] Additionally, *ab initio* data of ion-monohydrate binding energy and a derivative molecular mechanics model predicting the ion-monohydrate separation distance[228] were used as target data for ion-monohydrate interaction.

LJ parameters for Be^{2+} were varied and the free energy of hydration (ΔG_{hyd}) in TIP3P water was calculated using FEP as described in Sec. 3.2.3. The ion-monohydrate interaction energy and separation distance were also calculated using CHARMM directives.[33] CHARMM LJ parameters ε and $r^{\min}$ were varied along a grid, with ΔG_{hyd} and monohydrate interactions calculated for values of ε varied from $[-0.0115, -0.0006]$

in increments of 5×10^{-5} and $r^{\min}$ varied from $[0.2, 1.3]$ in increments of 0.1. The parameter set that minimized error in all three measurements was chosen.

The chosen ε, $r^{\min}$ pair was then used to find the peak position of $g(r)$ and coordination number of a 5.3-molal aqueous solution of $BeCl_2$. The coordination number can be found by integrating over the first peak of the radial distribution function of Be^{2+}:

$$n_{\text{coor}} = 4\pi\rho \int_0^{r_1} g(r) r^2 dr. \quad (30)$$

The integral is computed from a separation distance $r = 0$ to $r = r_1$, where r_1 is the minimum after the first peak of $g(r)$. Results for n_{coor} and $g(r)$ peak position were in satisfactory agreement with experiment.

4.2.5. Adjusting interaction parameters to fit experimental ΔG_{r} between Be2+ and PS component molecules.

FEP simulations were used to obtain the association energy of each observed configuration from bulk solution simulations of divalent ions with PS components described in Sec. 4.2.2. Decoupling of the nonbonded potential and selection of attenuation parameters for FEP simulations are described in Sec. 3.2.3. The total free energy of the reaction, ΔG_{r}, depends on the free energy of each binding configuration ΔG_{c}:[229]

$$\Delta G_{\text{r}} = -k_B T \ln\left(\sum_i e^{-\frac{\Delta G_{\text{c}}^i}{k_B T}}\right). \quad (31)$$

Each ΔG_{c}^i is computed from FEP simulations as described in Sec. 3.2.3, and ΔG_{r} is an effective free energy representing contributions from all binding configurations. It is related to the equilibrium binding constant of the reaction from ITC (K_r^{eq}) by:

$$\Delta G_{\text{r}} = -k_B T \ln K_{\text{r}}^{\text{eq}}. \quad (32)$$

Because DMP and acetate each present Be^{2+} with a single binding site at biological pH,[230] solution configurations of these molecules were defined as the number of associated small molecules per Be^{2+} ion. For a given ΔG_c^i, the initial stage of the thermodynamic cycle included aqueous Be^{2+} and the final stage included Be^{2+} bound to a given PS component, with starting coordinates taken from the bulk solution simulations described in Sec. 4.2.2. This cycle was chosen to mimic experimental conditions in which PS components were gradually titrated into solutions containing Be^{2+}. Experimental K_r^{eq} are therefore in terms of mols of PS components, requiring division of ΔG_r by the computed coordination of Be^{2+}. Because states with 0, 1, 2, 3, or 4 interacting PS components (representing coordination of 0, 1, 2, 3, or 4 PS components) consistently differed by at least 3 kcal/mol, bulk solution simulations contained two simultaneous states. For example, using adjusted LJ parameters, Be^{2+} interacts with 1 or 2 molecules of DMP after equilibration. The theoretical relative probability p_{rel} of the two relevant states can then be computed from the free energy difference between the states:

$$-kT \ln p_{rel} = \Delta G_c^{1\rightarrow 2}, \tag{33}$$

and the theoretical probabilities can be solved with a system of linear equations:

$$p_{rel} = \frac{p_2}{p_1};\ p_1 + p_2 = 1. \tag{34}$$

In the case of Be^{2+}/acetate reactions after adjustment of LJ parameters, Be^{2+} was seen to coordinate 1 or 0 acetate molecules, allowing simultaneous sampling of these states in a single series of FEP simulations and rendering division by coordination number unnecessary.

In this way, ΔG_{r} calculated from simulation was compared with the $K_{\mathrm{r}}^{\mathrm{eq}}$ found from ITC, and simulation parameters adjusted iteratively until ΔG_{r} from simulation was in satisfactory agreement with the experimental value.

In the CHARMM force field, interaction energy between nonbonded pairs is the sum of the Columbic and Lennard-Jones (LJ) contributions. The LJ potential (eq. 2) is a function of separation distance r_{ij} between atoms i and j; ϵ is the dielectric constant of the media, and q_i is the partial atomic charge of the i^{th} atom. Energies depend on the LJ interaction parameters ε_{ij} and $r_{ij}^{\min}$, given by:

$$\varepsilon_{ij} = \sqrt{\varepsilon_i \varepsilon_j}; \tag{35}$$

$$r_{ij}^{\min} = \frac{r_i^{\min} + r_j^{\min}}{2}. \tag{36}$$

Use of these combining rules implies lack of empirical, interaction-specific parameterization for a given pair of atom types. In the case of highly charged species, the parameters $r_{ij}^{\min}$ are doubly significant because they affect pair separation and therefore the strength of Coulomb interactions. Additionally, lack of atomic polarizability tends to augment ionic interactions at close range. Historically, pair-specific interactions have been adjusted by increasing $r_{ij}^{\min}$.[212] The value of $r_{ij}^{\min}$ can be supplied for a specific atom pair using the "NBFIX" directive in CHARMM or NAMD.

Values of $r_{ij}^{\min}$ were varied for each Be^{2+}/small molecule pair until ΔG_r from simulation reached satisfactory agreement with the value found from ITC binding experiments. Interacting atom pairs and values of $r_{ij}^{\min}$ tested for each pair are listed in **Error! Reference source not found.**.

Table 14. Values of r_{ij}^{min} used in FEP simulations to calculate free energy of association ΔG_c.

Small Molecule	CHARMM Atom Types	r_{ij}^{min} Tested/ # of Trials
DMP Lipid FF	O2L	2.51*/2
		2.8/2
		2.82/2
		2.84/4
		2.86/3
		2.88/3
		2.9/3
		2.92/3
		2.95/3
		3.0/1
acetate CGEN FF	OG2D2	2.51*/2
		2.6/2
		2.8/2
		3.0/2
		3.20/3
		3.23/2
		3.25/2
acetate Lipid FF**	OCL	2.51*/2
		3.0/3
		3.07/3
		3.1/4
		3.2/3

*Default values for $\boldsymbol{r_{ij}^{min}}$, calculated using eq. (36) and Be^{2+} LJ parameters developed in this study.
**New soluble acetate model for Lipid FF..

In addition to computing theoretical configuration probabilities according to eq. 31, configurations were counted from trajectories of solution simulations for comparison with FEP results. The number of associated small molecules per Be^{2+} ion (N_{SM}) was found. Probabilities of configurations with 0, 1, 2, 3, or 4 associated small molecules (N_{SM} = 0, 1, 2, 3, or 4) were counted using the integral of the pair correlation function from Be^{2+}/small molecule simulations. For example, it was observed that before adjusting LJ interaction parameters, Be^{2+} could take two possible configurations in association with DMP: It could associate with 2 or 3 molecules of DMP. The $g(r)$ of Be^{2+} with the deprotonated oxygen of DMP (O_{dp}) was used to count probabilities of bound configurations.

The number of binding events per Be^{2+} ion, $N_{Be^{2+}-O_{dp}}$, is associated with the integral of the pair correlation function:

$$N_{Be^{2+}-O_{dp}} = 4\pi\rho \int_0^{r_1} g(r)_{Be^{2+}-O_{dp}} r^2 dr. \quad (37)$$

Here, $g(r)_{Be^{2+}-O_{dp}}$ is the pair correlation function of the separation distance between Be^{2+} and O_{dp}. $N_{Be^{2+}-O_{dp}}$ is the average number of O_{dp} associating with a single Be^{2+} ion. The average binding distance is the position of the first peak of $g(r)_{Be^{2+}-O_{dp}}$, and the integral is computed over the first peak.

From $N_{Be^{2+}-O_{dp}}$, the probability of each divalent ion associating with 0, 1, 2, 3, or 4 PS component molecules in solution simulations can be calculated by solving a system of linear equations. The system of equations chosen depends on the possible values of N_{SM}. The sum of all configuration probabilities equals 1:

$$p_0 + p_1 + p_2 + p_3 + p_4 = 1. \quad (38)$$

Here, p_i is the probability of a divalent ion associating with i small molecules. To avoid double-counting of free divalent ions, p_0 was included with p_1 when calculating ΔG_r ($p_{1/0} = p_1 + p_0$), because dissociation was observed in FEP simulations where $N_{SM} = 1$ and $p_0 > 1$. Configurations with probabilities less than 0.02 were neglected. Systems of equations used to find configuration probabilities from solution simulations before and after adjustment of r_{ij}^{min} are listed in

Table **15**.

Table 15. Systems of equations to evaluate configuration probabilities for Be^{2+} interactions.*

Small Molecule		N_{SM}	System of Equations
DMP	Lipid FF	3, 2	$3p_3 + 2p_2 = N_{Be^{2+}-O_{dp}}$; $p_2 + p_3 = 1$
	Adjusted	2, 1	$2p_2 + 1p_1 = N_{Be^{2+}-O_{dp}}$; $p_1 + p_2 = 1$
Acetate	CGEN FF	4, 3	$4p_4 + 3p_3 = N_{Be^{2+}-O_{dp}}$; $p_4 + p_3 = 1$
	Adjusted	1, 0	$1p_1 = N_{Be^{2+}-O_{dp}}$; $p_0 + p_1 = 1$
	Lipid FF**	3, 2	$3p_3 + 2p_2 = N_{Be^{2+}-O_{dp}}$; $p_2 + p_3 = 1$
	Adjusted	1, 0	$1p_1 = N_{Be^{2+}-O_{dp}}$; $p_0 + p_1 = 1$

*N_{SM} = number of associated molecules; $N_{Be^{2+}-O_{dp}}$ = number of associated free oxygens; p_i = probability of associating with i small molecules.
**New soluble acetate model for Lipid FF.

4.2.6. Analyzing DOPS monolayer trajectories.

Interfacial tensions (γ_m) are calculated from simulation using the diagonal elements of the pressure tensor:[231]

$$\gamma_m = 0.5\left(L_z\left[P_{zz} - 0.5\left(P_{xx} + P_{yy}\right)\right]\right). \quad (40)$$

Here, L_z is the size of the simulation box normal to the interface, P_{zz} is the normal component of the pressure tensor, and P_{xx} and P_{yy} are the tangential components. The prefactor of 0.5 is needed to account for the presence of two water-lipid interfaces in the simulation box. For comparison, γ_m can be calculated from experimental surface pressures (π) by subtracting π from the surface tension of pure water (γ_0): $\gamma_m = \gamma_0 - \pi$.[232] At T = 295.15 K, $\gamma_0 = 72.5$ dyn/cm.[233] Error in γ_m from simulation was estimated from the standard deviation of samples computed over 1-ns blocks.

Residence times of divalent ions at DOPS monolayer binding sites were computed from 30 – 120 ns using the CHARMM program[33] and standard errors were computed. From the residence times, expected occupancies were also computed using CHARMM, here defined as the expected number of associations with interacting DOPS oxygen a given time (can be greater than 1). Be^{2+} and O_{DP} are considered to associate if they are found within association distance r_{cut}, which is 2.1 and 2.5 Å for phosphate and acetate oxygens, respectively, for Be^{2+}; and within 3.4 Å for both species with K^+. Water bridging associations were analyzed using the CHARMM directive "ncoor hbond" with "cuthb" set to 2.5 Å between associating species and TIP3P water residues.

4.3. Methods for Investigating K^+ Interactions with PEG

4.3.1. SANS experiments of PEG in solution with KCl.

R_g of 29-mer PEG in various concentrations of KCl were computed from analysis SANS intensity curves. Various weight/volume of PEG (0.05, 1.0, 2.0, and 2.5 %) were solvated in D_2O with electrolyte concentrations of 0.0, 0.5, 0.1, 0.5, 1.0, 1.5, 2.5, and 3.0 M KCl. All solutions were buffered with 10 mM tris and titrated using 3 M citric acid to a final pH of 7.0. Sodium azide at 0.1 % w/v was added to the solutions as a bacteriostat. Incoming wave vectors q as high as 0.3 $Å^{-1}$ were scattered and baseline intensity subtracted. From resulting scattering curves, R_g was extrapolated to infinite dilution of PEG at each KCl concentration. Experiments were performed by the Center for Neutron Research at the National Institute of Standards and Technology under the guidance of Arvind Balijepalli.

Guinier analysis was used to find R_g from scattering intensity curves $I(q)$. In Guinier analysis, the natural log of the intensity is plotted as a function of the wave vector

q squared: $\ln I(q)$ vs. q^2. From the slope m of the best-fit line to the low-angle portion of this graph, R_g can be calculated: $m = -{R_g}^2/3$.[234] In experimental estimates, linear extrapolation was made to infinite dilution of PEG.

4.3.2. Comparison of R_g of PEG from experiment and simulation.

Simulations of a single 29-mer PEG in 0, 1, and 3 M KCl were run at 298.15 K for 150 ns using the C36e FF[72] and the modified TIP3P water model.[54, 55] The NPT ensemble was maintained and the NAMD[185] software package used as described in Sec. 3.2.4. The C36 NBFIX parameters developed by Luo and Roux were used for KCl.[212] Twelve simulations were run with six sets (at 1 and 3 M KCl) of LJ ($\varepsilon_{ij}, r_{ij}^{\min}$) pairs specified between the PEG ether oxygen and K^+, one simulation in pure water, and 4 simulations with different LJ pairs specified between K^+ and Cl^- at 1 M KCl (a total of 17 trajectories). Guinier analysis was used to find R_g from simulation scattering intensity curves $I(q)$.

The SANS/SWAXS package for GROMACS developed by Jochen Hub and colleagues was used to compute $I(q)$ from simulation (citations include SWAXS development whereas SANS addition is not yet published).[216, 217] This code allows computation of R_g in user-specified D_2O-water mixtures from simulations of water, as the two have different neutron scattering lengths; deuterium has a substantially positive coherent scattering length, whereas that of hydrogen is negative.[235] Use of D_2O with non-deuterated samples can therefore increase contrast between solute and solvent scattering intensity.

Section 4.5.2 includes scattering curves for PEG in pure D_2O and in D_2O/KCl mixtures. The SANS code constructs an envelope around the solvent (Figure 27). All molecules within in the envelope are considered to contribute to $I(q)$. The envelope is

constructed from an icosphere with 5120 triangular faces (recommended from ref. [216, 217]). The icosphere is centered at the center of mass of the solute, and the vertices of the envelope are moved radially to reach a distance d from solute atoms; $d = 0.7$ Å. At each analysis step, the icosphere evolves to encompass the solute. For subtraction of base $I(q)$ of D_2O, the code also computes intensity from a projection of the envelope onto a trajectory of pure solvent. This procedure was used to compute R_g in pure water, but not in KCl mixtures.

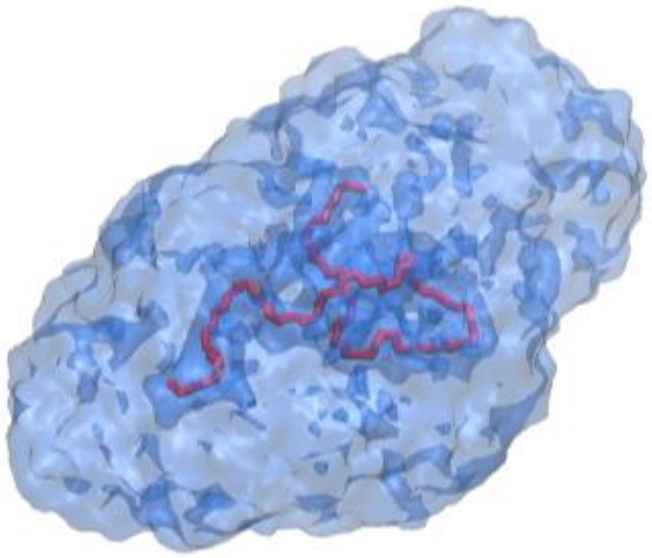

Figure 27. Hydration envelope of 29-mer PEG in pure D_2O. Waters within 7 nm of PEG were included in the envelope, which evolves to encompass the polymer at each analysis step.

While this method appropriately yielded a slightly higher R_g of PEG when the hydration envelope was accounted for in pure water simulations, PEG/KCl simulations did not show a change in R_g when the solvent envelope was included vs. when R_g was computed from PEG only. We believe this is incorrect and have omitted R_g results including the hydration envelope in KCl simulations from the results section (4.5.2). Figure 28 plots the pair correlation functions between PEG oxygen and water hydrogen in pure water and in 1 and 3 M KCl with various LJ interaction parameter sets between the ether

oxygen and K^+. While water density is very slightly decreased in the second and third peaks in higher concentrations of KCl (due to ions replacing water), the shape of $g(r)$ is unchanged, indicating a similar structure for water around PEG in all simulations. The SANS and SWAXS codes Jochen Hub provided compute the background scattering intensity by projecting the solvation envelope onto a separate pure solvent trajectory. This will not provide an accurate estimate of background intensity if differences exist between K^+ or Cl^- distributions in the PEG simulation vs. the pure solvent simulation. If, for example, PEG doesn't bind tightly to either ion, but is taking up space, it's possible that the pure salt simulation isn't indicative of actual ion density in the PEG simulation. Thus, to account for contributions of solvent in KCl mixtures, further analysis is needed. I intend to use SIMtoEXP,[189] which subtracts background intensity computed from the same simulation rather than a separate simulation, but adjustments will need to be made to account for SIMtoEXP's use of planar symmetry.

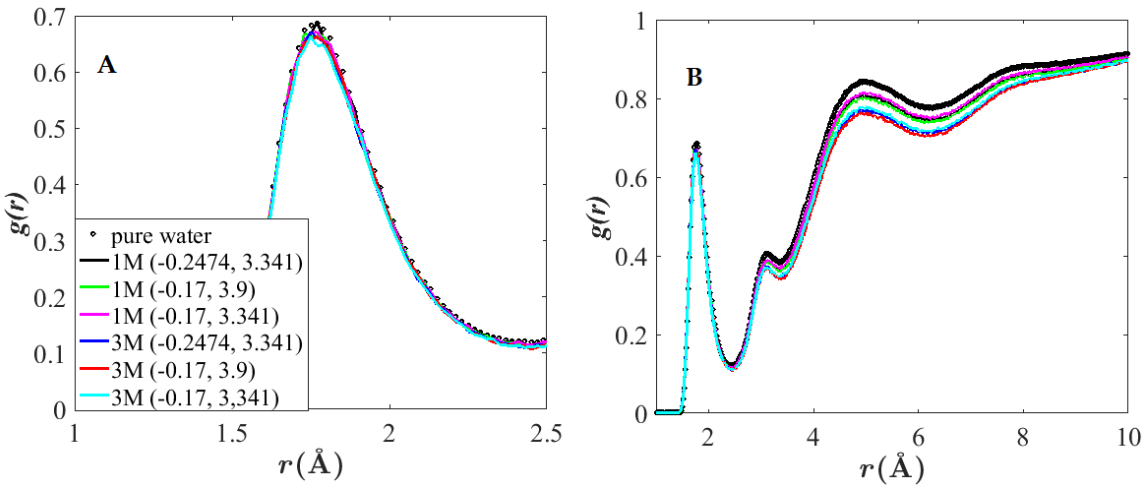

Figure 28. $g(r)$ between PEG oxygen and water hydrogen.. A) first peak; B) r > 10 Å. LJ ($\varepsilon_{ij}, r_{ij}^{\min}$) interaction parameters shown in key.

4.3.3. QM and MD calculations of K^+/PEG and K^+/Cl^- interaction energies

Quantum mechanical calculations of interaction energies between a single K^+ ion and diethoxyethane ($C_6H_{14}O_2$) in water were used to characterize K^+ interactions with the ether oxygen of PEG. Initial configurations were taken from trajectories of a 29-mer PEG in 3 M KCl solution described above. It was observed that the O-C-C-O dihedral had strong preference for the *gauche* configuration in these simulations (> 95 % *gauche* vs. *trans*), and that K^+ preferentially oriented in a triangular configuration between two PEG oxygens; starting configurations were chosen accordingly.

Gaussian09 with revision A.02[236] was used to compute QM interaction energies at various ion-DEOE separation distances. The interaction energy is defined as:

$$E_{\text{interaction}} = E_{\text{system}} - (E_{\text{DEOE}} + E_{\text{K+}}). \quad (41)$$

Coordinates for the DEOE-only system were taken directly from optimization of the DEOE-K^+ system; this allowed a more direct comparison to MD interaction energies, which were output directly from solution simulations after minimization (see below).

DEOE-K^+ calculations were completed at the MP2/def2TZVPP//MP2/def2QVZPP level. The TURBOMOLE triple and quadruple zeta basis sets with additional polarization functions were used,[237] to our knowledge the largest basis sets available for K^+. While these are typically used with DFT methods, they have been shown to match molecular bond energies with 0.01 to 0.07 eV/atom in MP2 calculations relative to high-performing reference basis sets.[238] For compounds containing third row electrons such as potassium, the inclusion of high-lying core orbitals in the active space can be necessary for accurate correlated treatments. The QZVPP basis sets provide sufficient flexibility to polarize the core in these cases.[237]

Because water is assumed to have a shielding effect on interacting charges, the implicit solvation model SMD was used in all QM calculations, where "D" denotes the full solute electron density is used without defining partial charge.[239] The solvent is represented as a dielectric medium with surface tension at the solute-solvent boundary. SMD achieves mean errors of 0.6−1.0 kcal/mol in the solvation free energies of tested neutrals and 4 kcal/mol for ions; acceptably low when one considers that the hydration free energy of potassium is estimated to be -80 kcal/mol.[240]

For comparison with MD, an ensemble of water configurations was needed to model the effects of using an implicit solvent. From simulations of DEOE with K^+ and explicit water, in which restraints were placed on the distance between K^+ and both ether oxygens and on the OCCO dihedral to maintain *gauche* character, 100 snapshots were taken. Interaction energy between the DEOE residue and K^+ was computed for each snapshot and the energies averaged for a given separation $r =$ (2.48, 2.63, 2.73, 2.77, 2.85, 2.865, 2.885, 3.0, 3.115, 3.215, 3.365) Å. Interaction energies were computed for 10 ($\varepsilon_{ij}, r_{ij}^{\min}$) pairs: ε_{ij} = (-0.17, -0.17, -0.05, -0.1, -0.08, -0.06, -0.17,-0.25, -0.09327, -0.2) and $r_{ij}^{\min}$ = (3.41375, 3.9, 3.9, 2.9, 2.9, 2.9, 2.9,3.44, 3.41375, 3.44).

MD simulations were run with the CHARMM program[33] using the NPT ensemble and the C36e FF[72] as described in Sec. 2.2.1. A 1-fs timestep was used. Snapshots were collected over 5 ns after a 6 ns equilibration. Systems contained 420 waters. Long-range electrostatic interactions were evaluated using PME[109] with a cutoff for real-space calculations $r_{\text{cut}} = 12$ Å.

Matlab R2016a[190] was used to find best-fit ($\varepsilon_{ij}, r_{ij}^{\min}$) pair. This was accomplished with the scatteredInterpolant function, which linearly interpolates interaction energies by

triangulating between results from tested $(\varepsilon_{ij}, r_{ij}^{\min})$ pairs using Delaunay triangulation. The resulting mesh was queried along a grid of $(\varepsilon_{ij}, r_{ij}^{\min})$ values to predict the pair that yielded the least mean squared error from the QM results at tested values of r.

4.4. Results for Be^{2+} Interactions with PS

4.4.1. ITC results

Two possible coordinating atoms for Be^{2+} in the surface-exposed headgroup of PS are the phosphoryl oxygen (above the glycerol-ester linkage) and the carboxylate oxygen (headgroup terminal). Acetate and DMP, shown in Figure 29, were chosen as model compounds as they carry the same types of cation-coordinating oxygen atoms. DOPS, used in monolayer simulations, is also shown in Figure 29.

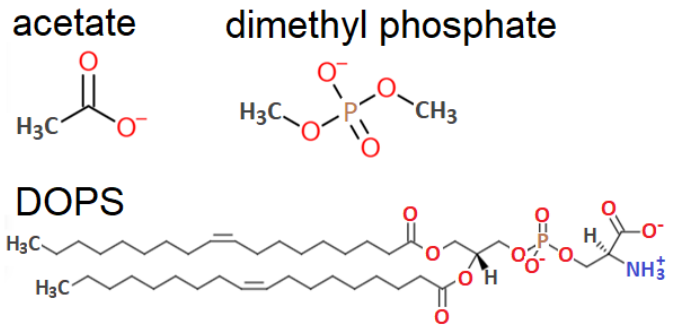

Figure 29. Structures of acetate, dimethyl phosphate, and DOPS. DOPS with denoted positions of electronegative ion-binding atoms; and structures of small molecules, acetate and dimethyl phosphate, carrying similar types of oxygens and representing separate ion-binding components of PS.

Be^{2+} is known to interact strongly with phosphate oxygen,[241] which is here assumed to prevent Be^{2+} from penetrating to the carbonyl oxygens located deeper along the bilayer normal. Monolayer simulation results (discussed in Sec. 4.4.4) corroborate this assumption; Be^{2+} was not seen to interact with ester carbonyls due to strong coordination by phosphate oxygens.

Results in Table 16 indicate that Be^{2+} binds to DMP with moderate affinity (K_d~2 uM), and with much weaker affinity to acetate (K_d~3 mM). ΔG is negative and ΔH positive, indicating entropically-driven reactions, likely due to liberation of water when ions are dehydrated. The control titrations shown in Figure 30A and C indicate a large heat of dilution for aqueous DMP, but not for acetate. Subtracting the heat of dilution of DMP reverses the sign of ΔH for DMP + Be^{2+} from negative to positive at the experimental pH, temperature, and concentration levels (Figure 30B). Strong association with phosphate comports with a known property of Be^{2+}; above pH 3, Be^{2+} precipitates in phosphate buffer, even in the presence of chelating ligands such as DHBA.[241]

Table 16. Thermodynamic parameters of binding obtained from ITC experiments.

Reaction	K_r^{eq} (1/M)	ΔH (cal/mol)	N	S (cal/mol/°C)
Be^{2+} + DMP	48050 ± 8800	4530 ± 193	0.19 ± 0.03	36.43 ± 0.26
Be^{2+} + Acetate	320 ± 15	5946 ± 130	0.82 ± 0.02	31.03 ± 0.32

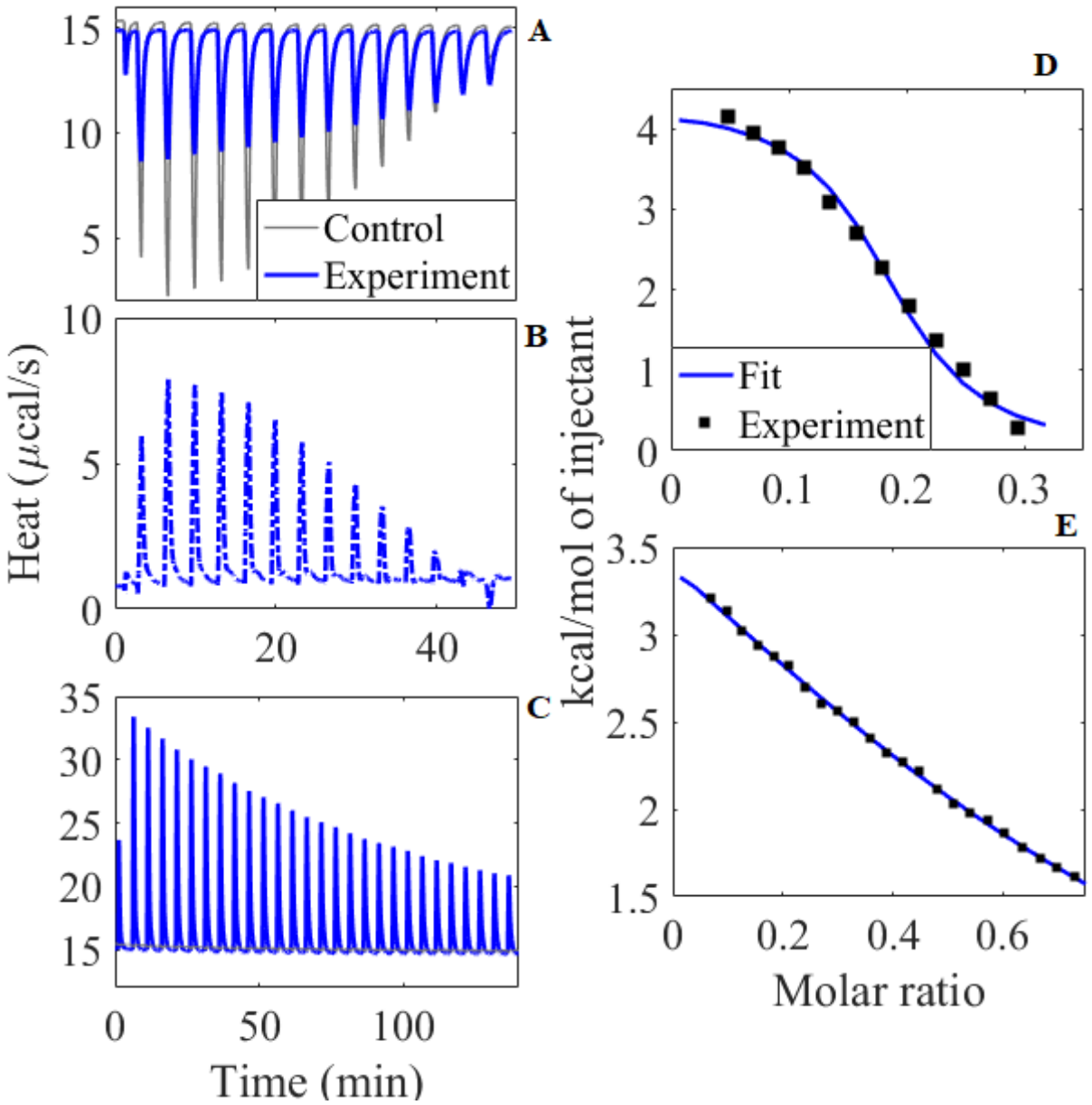

Figure 30. Titration results.. Raw titration data for Be^{2+} into DMP solution (A), with control subtracted (B), and into acetate solution (C); integrated heat for Be^{2+} into DMP solution (D) and acetate solution (E). In integrated heat plots, molar ratio is shown for small molecule/Be^{2+} in cell, and control was subtracted from integrated heat. Control in (C) is present but not visible at around 15 kcal/mol.

Figure 30D and E show the fit to the integrated heat of a single trial each of DMP and acetate titration. It is likely that full saturation was not reached in these experiments due to limitations inherent in the systems. This may cause systematic errors in estimates of ΔH or n not reflected in the standard errors in these measurements. The slopes of each fit

are clearly defined indicating accurate measure of the rate of change of heat with respect to relative concentration. To assure accurate calculation of K_r^{eq}, neither ΔH nor n were fixed during fitting. From these reliably converging fits the K_r^{eq} parameter is extracted.[218]

4.4.2. CHARMM LJ parameters for Be^{2+} interactions with water.

Following the iterative procedure described in Sec. 2.4, in which Be^{2+} with various values of the LJ parameters $r_i^{\min}$ and ε_i was evaluated for energetic and structural interactions with water, LJ parameters were chosen which yielded satisfactory agreement with all observables. Final LJ parameters for Be^{2+} are: $\frac{1}{2}r_i^{\min} = 0.8085$ Å; $\varepsilon_i =$ -0.000825 kcal/mol. The binding radius is lower in magnitude than other ions[242] in the CHARMM FF, reflecting the great binding capacity of this small divalent ion. The next-smallest binding radius of 1.18 belongs to Mg^{2+}. The energy well is shallower than that of Li^+, which has $\varepsilon_i =$ -0.0023 kcaol/mol,[224, 243] and considerably shallower than that of the larger Ca^{2+} ($\varepsilon_i =$ -0.12 kcal/mol).[244] The shallower LJ energy well contributes to beryllium's low coordination number (n=4).

Be^{2+} solution and monohydrate results are listed in Table 17. Final Be^{2+} LJ parameters yield improved agreement with experimental properties of 5.3-molal $BeCl_2$ solutions, with a $g(r)$ peak position of 1.55 Å and a coordination of 3.94, both within 10 % of experimental values (1.66 Å and 4, respectively[211, 219]). ΔG_{hyd} underestimates experiment by 9 % at 298.15 K (in magnitude). This is because energetic and structural properties were found to be at odds. For example, use of a lower $r_{\min}$ parameter for Be^{2+} would bring ΔG_{hyd} in closer agreement with experiment, but also decrease the $g(r)$ peak position.

Table 17. Be^{2+} interactions with bulk water.

	Simulation	Target Result from Exp. or QM	Difference
		Exp.[211, 219, 227]	
ΔG_{hyd} (kcal/mol)	-522.0 ± 0.3	-572	8.7 %
$g(r)$ Peak Position* (Å)	1.55	1.66 – 1.67	-6.60 %
Coordination Number*	3.94 ± 0.08	4	-1.6 %
		QM model results[228]	
Monohydrate Energy (kcal/mol)	-131.9	-139.4, -146.1	9.3 %
Monohydrate Separation (Å)	1.37	1.51 Å	-9.27 %

*5.3 molal aqueous $BeCl_2$ at 298.15 K.

Figure 31 plots $g(r)$ for Be^{2+} in a 5.3-molal solution of $BeCl_2$. The pair correlation function between Be^{2+} and water differs from the total $g(r)$ (between Be^{2+} and water/Cl^-)in that it has a distinct secondary peak attributable to Be^{2+}- Cl^- interactions. In the experimental study by Yamaguchi et al,[219] $g(r)$ between Be^{2+} and Cl^- is not deduced from experiment, but the authors note a decrease in Cl^- coordination by water oxygen in the presence of Be^{2+}, indicating association of the two ionic species at this concentration.

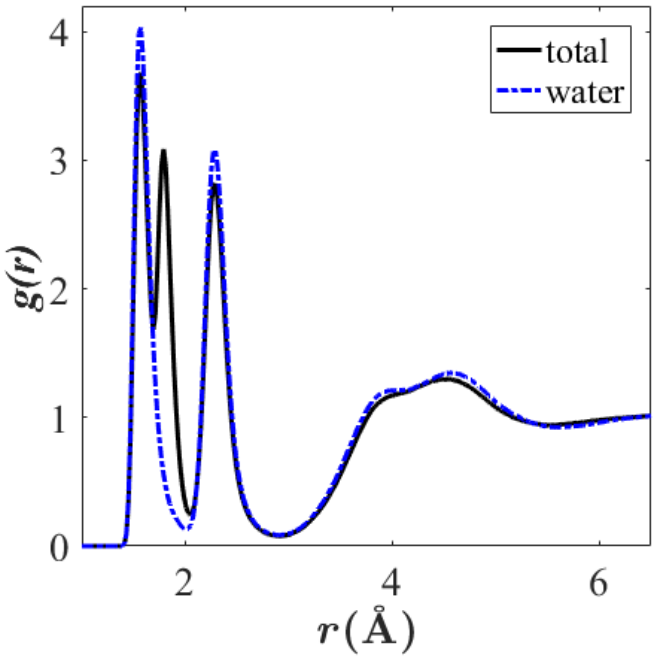

Figure 31. Radial distribution functions for 5.3-molal BeCl solution. Total radial distribution function for Be^{2+} (black; Be^{2+} with water and Cl^{-}) and pair correlation function for Be^{2+} with water (blue).

QM results for ion-monohydrate interaction energy and separation distance listed in Table 17 are borrowed from a study by Yang et al.[228] The ion-monohydrate separation distance was computed with the atom bond electronegativity equalization method fused with molecular mechanics (ABEEM/MM). ABEEM and van der Waals parameters were fit to the interaction energies. As with solution properties, simulation results from the present study are within 10 % deviation from expected values. Final LJ parameters represent a compromise between accurate interaction energy and separation distance.

4.4.3. Divalent ion/small molecule interactions and simulation parameters.

With the LJ parameters fit to water interactions, Be^{2+} showed significant overbinding to both DMP and acetate. This is an expected result from a nonpolarizable FF in which close-range ionic interactions are not modulated by adjustment of effective atomic dipole moments.

Increasing the $r_{ij}^{\min}$ interaction parameter between Be^{2+} and interacting oxygens was sufficient to decrease binding probability and bring ΔG_{r} within 10 % deviation from ITC results. Table 18 lists the adjusted interaction parameters. For all atom type pairs, the default value was 2.51 ($\varepsilon = -0.12$ kcal/mol and $\frac{1}{2}r_i^{\min} = 1.7$ Å for all three oxygen types). The lipid FF required a lesser increase in $r_{ij}^{\min}$ with acetate than the CGEN FF, likely due to the reduced magnitude of charge assigned to OCL relative to OG2D2 (-0.67 and -0.76, respectively).

Table 18. Final $r_{ij}^{\min}$ [Å] interaction parameters with Be^{2+}.

Atom Type	**Small Molecule**	$\boldsymbol{r_{ij}^{\min}}$
O2L	phosphoryl, DMP	2.92
OG2D2	carboxylate, CGEN FF	3.20
OCL	carboxylate, Lipid FF	3.07

Table 19 compares configuration states and probabilities calculated from solution simulations before and after adjustment of $r_{ij}^{\min}$. It also gives the integration of the pair correlation function $N_{\mathrm{Be^{2+}-O_{dp}}}$, from which the numbers of associated molecules, N_{SM}, are computed. Because configurations are counted by the number of DMP or acetate ions bound to a single Be^{2+} atom, clustering is not reflected. Solution simulations with the original LJ parameters did exhibit clustering, but simulations with the adjusted parameters did not.

Table 19. Configuration states and probabilities**.**

Small Molecule		$N_{\mathrm{Be^{2+}-O_{dp}}}$	N_{SM}	p_i
DMP	Lipid FF	3.1	4, 3	0.10, 0.90
	Adjusted	1.31	2, 1	0.31, 0.69
Acetate	CGEN FF	3.5	4, 3	0.50, 0.50
	Adjusted	0.53	1, 0	0.53, 0.47
	Lipid FF*	2.93	3, 2	0.93, 0.07
	Adjusted	0.37	1, 0	0.37, 0.63

*New soluble acetate model for Lipid FF.

Error! Not a valid bookmark self-reference. compares resulting ΔG_{r} computed with eq. 31 with experiment and shows the extent of overbinding when parameters fit to water interactions are used. Interestingly, binding energies were nearly equivalent for all oxygen species before adjustment. This is significant because, in DOPS bilayers and monolayers, carboxylate sits at the water-lipid interface and encounters solvated Be^{2+} before phosphate. Overbinding to carboxylates could prevent Be^{2+} from penetrating deep enough into the headgroup region to bind with phosphate. Final $r_{ij}^{\min}$ parameters yield ΔG_{r} that agrees with experiment for all 3 reaction types.

Table 20. ΔG_r from experiment and simulation. Simulation values use the FEP method described in Sec. 4.2.4 and eqs. 31 and 33 - 34.

Small Molecule	Original $r_{ij}^{min}/\Delta G_r$ (kcal/mol)	Final Fit $r_{ij}^{min}/\Delta G_r$ (kcal/mol)	Exp. ΔG_r (kcal/mol)	Error, Fit/Exp.
DMP				
Lipid FF	2.51/ -18.87 ± 0.27	2.92/ -6.32 ± 0.23	-6.49 ± 0.12	-2.6 %
Acetate	2.51/	3.20/		
CGEN FF	-18.22 ± 0.37	-3.38 ± 0.31	-3.47 ± 0.03	-2.6 %
Lipid FF*	2.51/ -18.10 ± 0.27	3.07/ -3.76 ± 0.44	-3.47 ± 0.03	-7.8 %

*New soluble acetate model for Lipid FF.

To illustrate the difference between calculating $\Delta \boldsymbol{G_r}$ using eq. 31 (FEP only method) or eq. 39 (solution probabilities as published in [204]), Table 21 provides $\Delta \boldsymbol{G_c^i}$ from FEP (needed for both methods), and $\boldsymbol{p_{rel}}$ and $\boldsymbol{p_i}$ computed from these values (needed to use eq. 31), $\boldsymbol{p_i}$ found from solution counting method, resulting reduction factors for each method, and final $\Delta \boldsymbol{G_r}$ found using each method. Most of these values are also reported elsewhere; the table is intended for comparison of the two methods. Full comparison is only possible with adjusted DMP parameters because in unadjusted systems, clustering was seen and is not reflected in FEP values, which are only reported for associations with 3 PS components (requiring no addition method), and adjusted acetate parameters exhibit only a single elevated state which can be sampled in one series of FEP simulations, again requiring no addition method. (However, reduction by coordination number was necessary for the unadjusted systems.)

Table 21. Comparison of parameters used to find $\Delta \boldsymbol{G_r}$ of Be^{2+}/DMP using two methods (adjusted parameters only).

		FEP only (eq. 31)				Sol. counting (eq. 39)		
Configuration	ΔG_c^i **kcal/mol**	p_{rel}	p_i	**reduction factor**	ΔG_r **kcal/mol**	p_i	**reduction factor**	ΔG_r **kcal/mol**
2	-12.63	6E5	1	2	-6.32	0.31	1.31	-5.45
1	-4.59		0			0.69		

While solution simulations were seen to reach equilibration of Be^{2+} coordination, configuration probabilities for adjusted DMP (computed from solution simulations using systems of equations in Table 15) did not match the theoretical prediction from the free energies alone (computed with eqs. 31 and 33 – 34). Figure 32 shows the equilibration of Be^{2+} coordination by DMP in the bulk solution simulation with final adjusted LJ interaction parameters to be 1.3, whereas FEP results indicate nearly exclusive coordination by 2 DMP molecules.

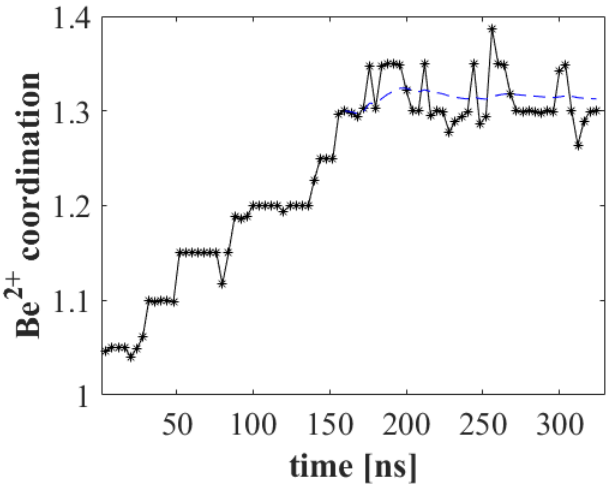

Figure 32. Be^{2+} coordination by DMP with adjusted LJ parameters.

In Figure 32, equilibration is seen around 160 ns. The discrepancy between the two methods of calculating Be^{2+} coordination my reflect the need for a longer solution simulation if the plateau seen at 160 ns does not represent true equilibration. Alternately, it may indicate the need to explore different methods of FEP to accurately reflect the solution environment and nature of the interaction. If ΔG_{r} is computed assuming a coordination of 1.3 DMP and additivity of the extrinsic Gibbs free energy as in eq. 39, one obtains ΔG_{r} = -5.45 kcal/mol (reported in Table 21), a difference of only 0.85 kcal/mol from the value reported in Table 20 from FEP energies only.

Figure 33 compares $g(r)_{\mathrm{Be^{2+}-O_{dp}}}$ before and after adjustment of lipid FF parameters. Note the adjustment of the LJ interaction parameters increased the separation distance between bound Be^{2+} and O_{dp}, and decreased the height of the first peak of $g(r)_{\mathrm{Be^{2+}-O_{dp}}}$, both indicating weaker binding after adjustment of the LJ interaction parameters. Additionally, $g(r)_{\mathrm{Be^{2+}-O_{dp}}}$ are very similar before parameter adjustment; the curves overlap but DMP peak is slightly higher. Coordination number, determined by integration of the first peak of $g(r)$, is greater for DMP than acetate after adjustment, and coordination is tighter, as can be seen from the closer $g(r)$ peak position.

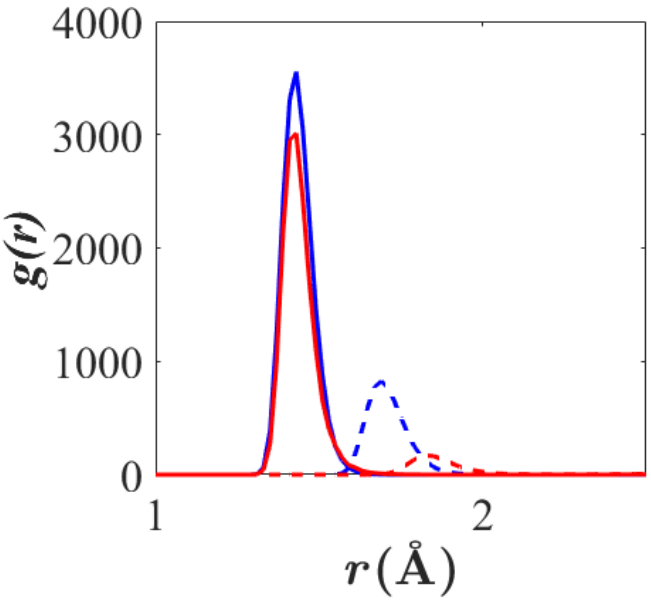

Figure 33. $g(r)_{Be^{2+}-O_{dp}}$ between Be^{2+} and free deprotonated oxygens. Blue: DMP. Red: acetate. Solid: initial $r_{ij}^{\min}$. Dashed: final $r_{ij}^{\min}$. Lipid FF parameters used.

Figure 34 shows sample configurations of Be^{2+} in solution with DMP (lipid FF). Water and Na^{+} ions are present but not shown. Default parameters show extensive clustering with DMP, but the resulting ΔG_r is too favorable, indicating these configurations are not realistic. Less clustering is seen with default acetate interaction parameters. In both DMP and acetate systems, adjustment of $r_{ij}^{\min}$ reduces clustering.

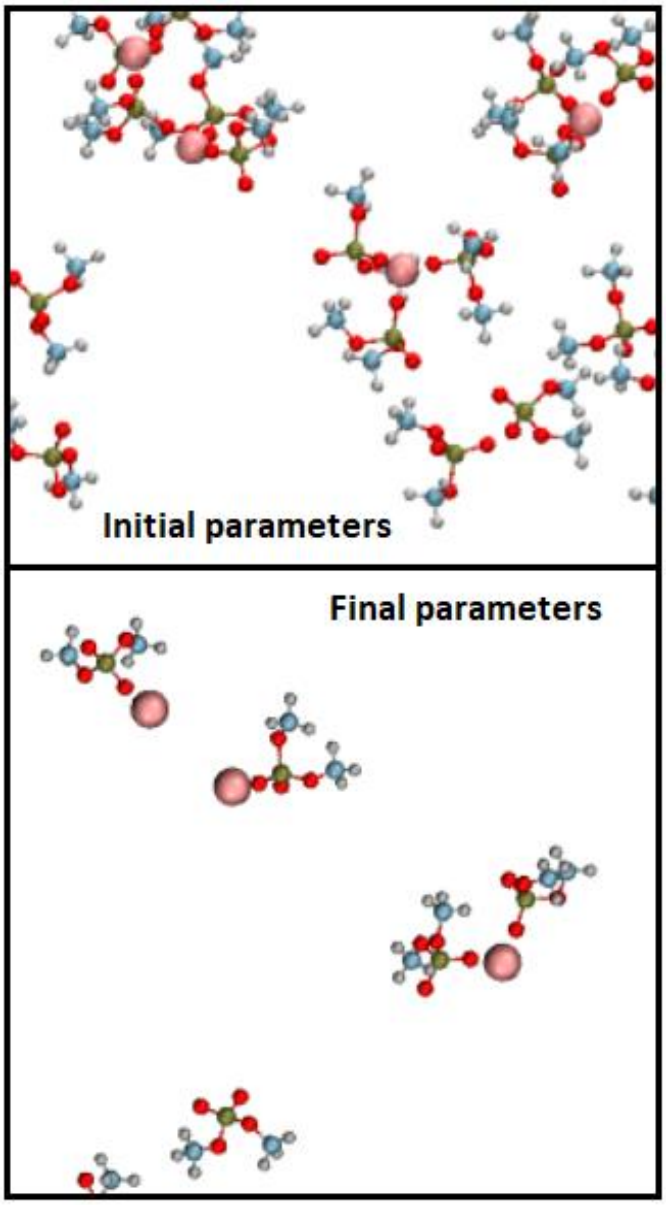

Figure 34. Be^{2+} in solution with DMP Default (top) and adjusted (bottom) LJ interaction parameters. Colors: Be^{2+}, pink; O, red; C, blue; H, gray; P, gold. Water and Na^{+} ions not shown.

4.4.4. DOPS monolayer surface tensions and Be^{2+} coordination.

Surface tensions of DOPS monolayers (γ_{m}) calculated from simulation agree with experiment for both Be^{2+} with adjusted interaction parameters and K^{+}. $A_l = 65.3$ Å^2/lipid is of interest because it is the experimental A_l for DOPS membranes at 303.15 K.[245] γ_{m}

for the sample trajectory fluctuates between 40 and 70 dyn/cm, with a mean of 52.8 dyn/cm calculated from 30 to 150 ns.

As has been demonstrated experimentally,[23] γ_{m} and A_l are directly related along a pressure-area isotherm; γ_{m} is higher at greater A_l. Figure 35 plots the experimental data (provided by Ermakov et al.[23]) for DOPS monolayers in solutions of 1 mM Be^{2+} or K^+. In the Langmuir experiments, the subphase solution contained 10 mM KCl as a background electrolyte and buffered with 2 mM Tris-HCl (pH 7.3). DOPS monolayers with Be^{2+} exhibit a greater γ_{m} than with K^+. At equal γ_{m}, DOPS monolayers in the presence of Be^{2+} have a lesser A_l, indicating that Be^{2+} has a compacting effect on the monolayer. This can be attributed to both strong ionic interactions with the divalent ion and the smaller radius of Be^{2+} relative to K^+. While not as strong as direct ion-oxygen associations, our findings also indicate that Be^{2+} is able to associate with phosphoryl and carboxylate oxygens through water bridging (see below).

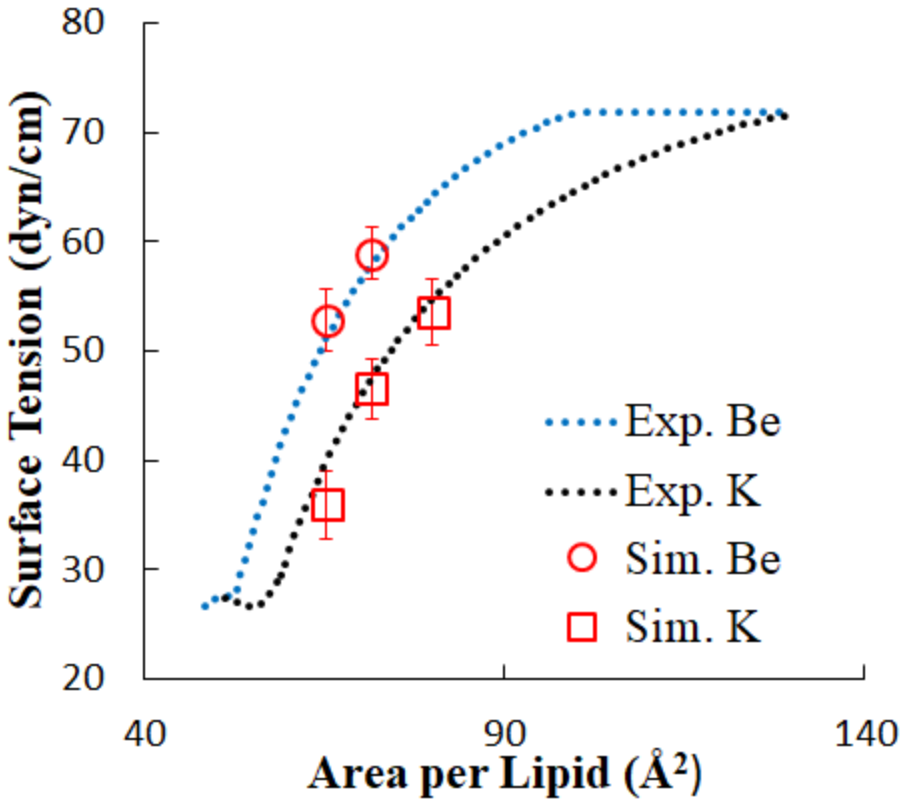

Figure 35. DOPS surface tension from Langmuir experiments and simulation. Bulk ion concentration in experiment: 1mM.[23]

Table 22 compares simulation results for γ_m, calculated using eq. (40), with experimental results.[23] Because experimental concentrations were too low to match with the simulation box size used, enough ions were added to equilibrate the system (40 Be^{2+} and 80 K^+). In Be^{2+}-DOPS systems, Be^{2+} saturated the monolayer and, due to long residence times, dissociated infrequently. The bulk concentration of Be^{2+} in these simulations therefore accurately represents the experimental concentration, in which Be^{2+} freely saturated the DOPS monolayers and existed in solution in concentrations too low to simulate. Experimental values for γ_m at 65.3 and 71.6 $Å^2$/lipid are reproduced in simulation using the adjusted interaction parameters. A snapshot for the distribution of Be^{2+} in an equilibrated monolayer simulation can be seen in Figure 36.

Table 22. DOPS monolayer surface tensions. Units of dyn/cm.

	65.3 Å^2/lipid	71.6 Å^2/lipid	80 Å^2/lipid
Be^{2+}			
Sim.	52.8 ± 5.8	58.9 ± 4.7	-
Exp.[23]	51.2	57.9	-
K^+			
Sim.	35.9 ± 6.3	46.6 ± 5.4	53.5 ± 6.1
Exp.[23]	41.3	47.5	54.7

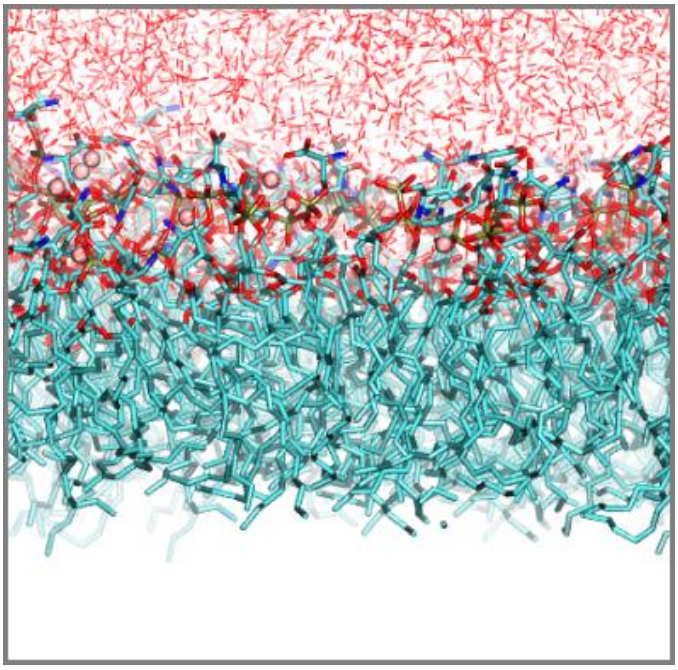

Figure 36. DOPS monolayer with bound Be^{2+}. A_l = 65.3 Å^2. Be^{2+}: pink sphere, C: teal licorice, O, red licorice, P:, gold licorice, N: blue licorice, water: blue dashed.

Figure 37 compares pair correlation functions $g(r)$ for Be^{2+} with various oxygens in DOPS monolayer simulations at 65.3 Å^2/lipid. The carboxylate peak below 2 Å is too small to be visible in $g(r)$ for all oxygens (black line), but the phosphate peak is clearly visible. From $g(r)$ for all oxygens, it is evident that more associations occur with water oxygens than with phosphate oxygens (the integral of this peak is greater).

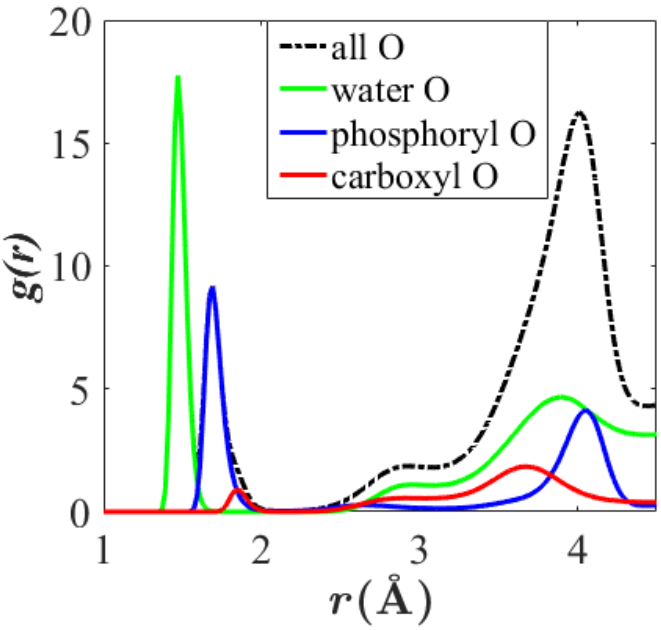

Figure 37. Pair correlation functions of Be^{2+} with various oxygens. $A_l = 65.3$ Å^2/lipid. For comparison, $g(r)$ are not normalized.

Preferential association with phosphate relative to acetate is not seen in K^+ simulations, although K^+ has not been specifically parameterized for these interactions. Solubility data of acetate and phosphate salts indicate that phosphate associates more strongly with ions in general, and with potassium in particular: Potassium acetate is about 17 times as soluble as potassium dihydrogen phosphate at standard temperature and pressure.[246] Additionally, the bond dissociation energy of potassium from trimethyl phosphate as determined by threshold collision-induced dissociation (CID) is similar to that of potassium with acetone and greater than with methanol (135, 140, and 92 kcal/mol, respectively).[247] Dissociation energies reveal that sodium binds more favorably to trimethyl phosphate than both acetone and methanol (171, 145, and 111 kcal/mol, respectively). Therefore, even fully methylated phosphate associates strongly with ions in solution, with equal or greater affinity than acetate binding sites. However, specific binding affinities of potassium with acetate and dimethyl phosphate are not known.

While $g(r)$ for Be^{2+} with lipid and water oxygens is similar at 71.6 and 65.3 Å^2/lipid, there is one notable difference: The more condensed monolayer shows close association with carboxylates, as can be seen from the pair correlation function of Be^{2+} with carboxylate oxygens in Figure 38. The $g(r)$ for the condensed monolayer has a sharp first peak at 1.85 Å, which is lacking in the monolayer with 71.6 Å^2/lipid. Both monolayers have secondary peak around 3.5 Å due to the proximity of the carboxylate oxygens to phosphate oxygens, which sit an average of 3.5 Å apart in these simulations.

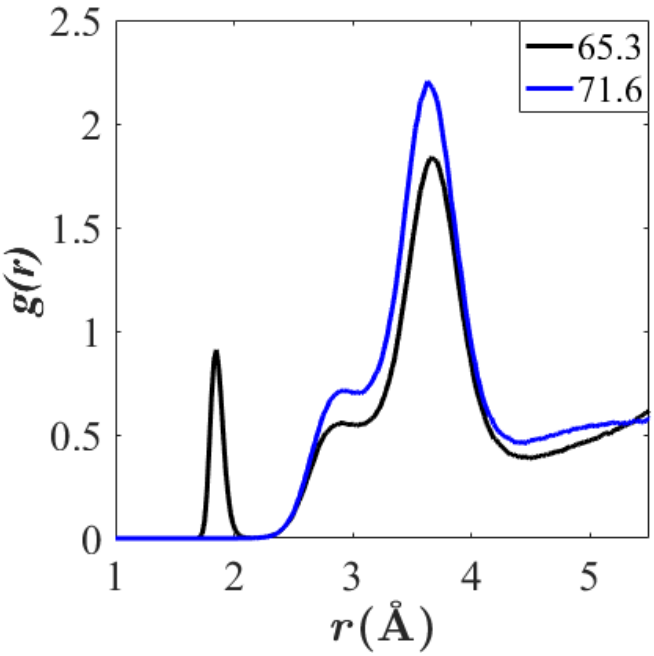

Figure 38. Pair correlation functions of Be^{2+} with DOPS carboxylate oxygens. Averaged over last 60 ns of trajectory for DOPS monolayer simulations with 65.3 and 71.6 Å^2/lipid. $A_l = 65.3$ Å^2/lipid. For consistency with Figure 37, $g(r)$ are not normalized.

Table 23 and

Table **24** quantify the associations between Be^{2+} or K^{+} and various oxygens in DOPS monolayer simulations. Ion-oxygen associations in

Table ***23***, computed from pair correlation functions, confirm that Be^{2+} only associates with carboxylate oxygen in the more condensed monolayer (65.3 $Å^2$/lipid). As would be expected, Be^{2+} associated with more lipid oxygens overall at 65.3 than at 71.6 $Å^2$/lipid; 1.84 and 1.64 associations, respectively. Each K^{+} ion associates with about 1 lipid oxygen, and some K^{+} is solvated.

Table **24** lists the average oxygen-ion residence times and occupancies computed from time series of bond distances. For example, the 0.42 expected occupancy for phosphoryl oxygen and Be^{2+} signifies that a given phosphoryl oxygen will coordinate an average of 0.42 Be^{2+} ions at a given time. While the residence time for Be^{2+} associations with phosphoryl oxygens in DOPS monolayers is significant (about 1/4 of the trajectory length used in the calculation), dissociations do occur. The residence time for associations with carboxylate oxygens, which only occur at higher A_l, is much shorter. This is expected given the greater magnitude of ΔG_r between Be^{2+} and phosphoryl oxygen found from ITC experiments. Residence times for K^+ associations are three orders of magnitude smaller than those for Be^{2+}-phosphate interactions and are similar for phosphoryl and carboxylate oxygens. K^+ expected occupancies are higher with carboxylate than phosphoryl oxygen, but parameterization of the relevant interaction parameters for potassium is needed to infer physical significance of this difference.

Table 23. Ion-oxygen associations in DOPS monolayer simulations.

	Phosphate	**Carboxylate**	**Water**	**Total**
Be^{2+}				
65.3 Å²/lipid	1.69	0.15	2.22	4.05
71.6 Å²/lipid	1.64	0.00	2.35	4.00
K^+				
65.3 Å²/lipid	0.34	0.75	5.67	6.76
71.6 Å²/lipid	0.27	0.70	5.89	6.86

Table 24. Residence times and expected occupancy for various oxygen-ion associations in DOPS monolayer simulations. Computed from 30 – 120 ns. Associations through water bridging included only for Be^{2+}. (Residence times are given in ps or ns timescale.)

	65.3 Å²/lipid				**71.6 Å²/lipid**			
	Phosphoryl	Phosphoryl + water	Carboxyl	Carboxyl + water	Phosphoryl	Phosphoryl + water	Carboxyl	Carboxyl + water
Be^{2+} Residence time	23.7 ± 1.2 ns	14.3 ± 0.4 ps	4.4 ± 0.5 ns	21.7 ± 0.7 ps	18.2 ± 1.0 ns	14.7 ± 0.3 ps	None	21.0 ± 0.8 ps
Occupancy	0.42	0.14	0.04	0.53	0.40	0.13	None	0.55
K^+ Residence time	22.8 ± 0.6 ps	-	30.5 ± 0.1 ps	-	21.0 ± 0.4 ps	-	27.7 ± 0.2 ps	-
Occupancy	0.18	-	0.39	-	0.14	-	0.36	-

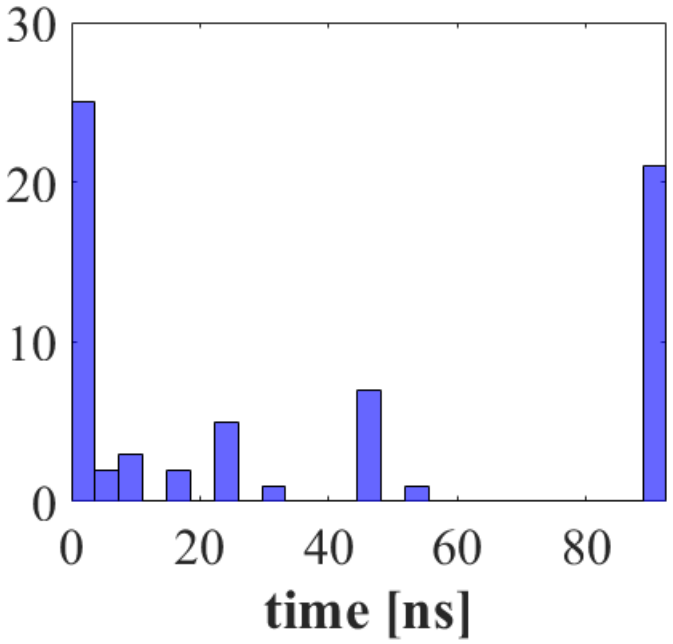

Figure 39. Histogram of Be^{2+}-phosphate association times. A_l = 65.3 Å^2, computed from 30 – 120 ns. Associations < 20 ps not shown.

Figure 39 is a histogram of residence times for Be^{2+}-phosphate associations with A_l = 65.3 Å, disregarding association times < 20 ps. Binding events can be separated into three regimes by duration of association. Twenty-one associations endured for the length of trajectory analyzed (90 ns), and another large group dissociated in less than 20 ns. A third regime of 15 associations were stable, but not as long, lasting between 20 and 60 ns.

The total number of associations is 67, 1.67 times the number of Be^{2+} ions in the simulation. Adding associations in the middle regime and the group that did not dissociate yields 21 + 15 = 36, nearly the number of Be^{2+} ions in the simulation. Thus, each Be^{2+} ion is coordinating an average of one or two lipids, and while some of these associations are weak, most Be^{2+} ions tightly coordinate a single phosphoryl oxygen. Figure 40 shows sample Be^{2+}-ion coordination by DOPS headgroups and snapshot bond distances.

Where Be^{2+} associates with water, it can form water bridges with both phosphoryl and carboxylate oxygens.

Table **24** reports bridging residence times and expected occupancies ("+ water" columns). Decreased association times (ps rather than ns scale) for bridging events indicate the expected weakness of bridged hydrogen bonding relative to direct associations. Bridging between Be^{2+} and carboxylate oxygens was more common than with phosphoryl oxygens. This is because direct association between Be^{2+} and phosphoryl oxygen positions carboxylate oxygen at an appropriate distance for a bridging event. Figure 40D. shows an example configuration of Be^{2+} directly coordinating phosphoryl oxygen and coordinating carboxylate oxygen through a water bridge. Bridging events were not significantly influenced by A_l.

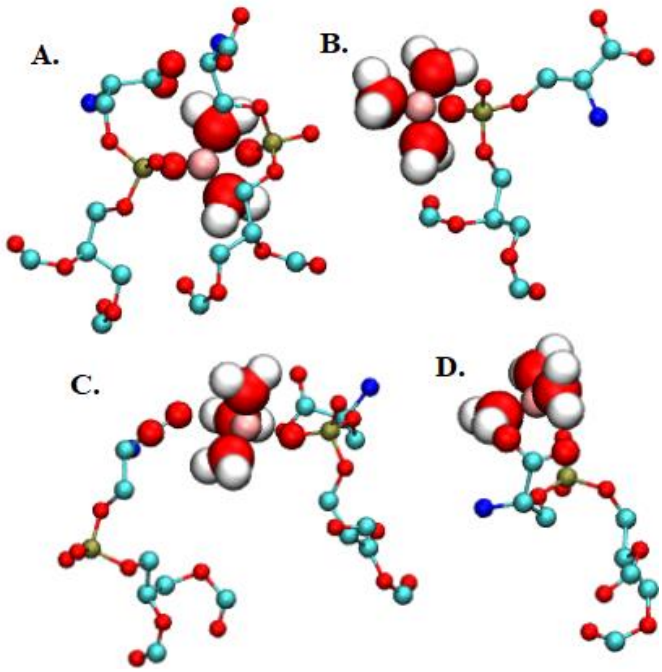

Figure 40. Common Be^{2+} binding configurations in DOPS monolayers. DOPS headgroups and Be^{2+} shown. Snapshot bond lengths (Å) in parentheses. A. Be^{2+} (pink sphere) coordinating 2 phosphate oxygens (1.68 and 2.7) and 2 water oxygens (avg. 1.48). B. Coordinating 1 phosphate oxygen (1.75) and 3 waters (avg. 1.51). C. Coordinating 1 acetate oxygen (2.5), 1 phosphate oxygen (1.77), and 3 waters (avg. 1.78). D. Water bridge with acetate (3.4 between Be^{2+} and acetate O; 2.0 between acetate O and water H; 1.5 between Be^{2+} and water O). Colors: C: teal licorice, O, red licorice, P:, gold licorice, N: blue licorice, water: red dashed interior. $A_l = 65.3$ Å^2.

4.5. Results for K^+ Interactions with PEG

4.5.1. QM and MD interaction energies between K^+ and ether oxygens.

It is well-known that default LJ interaction parameters computed using combining rules (eqs. 30 and 31) result in poor representation of ionic interactions in solution.[248] The simplest explanation for this is that combining rules are "filler" for missing pair-specific parameters and, in an empirically derived FF, accurate represent of pair-specific interactions is not likely to follow. In addition to the previously mentioned deficiency of using a single experimental observable, osmotic pressure, to fit NBFIX parameters for ion-ion interactions, the CHARMM community has historically fit only $r_{ij}^{\min}$ and not ε_{ij} for ionic interactions,[212, 249] although from U_{LJ} in eq. (2) it is clear that these parameters affect the potential in different ways. This has been justified as follows: Increasing $r_{ij}^{\min}$ as little as 0.1 Å results in a decrease of the favorability of ionic interactions in solution at separation distances r greater than the energy minimum, while ε_{ij} affects the depth of the LJ potential well.[248] Thus, the longer-range ionic interactions were treated by changing only $r_{ij}^{\min}$.

In one study,[249] Na^+/Cl^- interaction parameters for the Drude polarizable FF were fit to experimental osmotic pressures by changing $r_{ij}^{\min}$, and the *ab initio* Na^+/Cl^- potential energies in a vacuum as a function of r were compared with simulation results using both the new parameter set and the default parameters. While improvement was seen with the parameter set fit to osmotic pressure, the resulting energy well remains too deep relative to the QM results and the repulsion barrier is too steep, issues that could possibly be solved by fitting both ε_{ij} and $r_{ij}^{\min}$ to the interaction energy landscape. The authors note that *ab*

initio net energies computed in a vacuum are a poor representation of the energy landscape in solution.

To investigate the effects of ε_{ij} and $r_{ij}^{\min}$ on the interaction energy landscape in solution, QM interaction energies between and K^+/DEOE were computed in implicit solvent and compared with MD results in explicit water using various $(\varepsilon_{ij}, r_{ij}^{\min})$ sets. Interaction energy rather than absolute energy was chosen because relative energy allows for more direct comparison to MD.

Figure 41 plots results for K^+ interactions with DEOE. Values for $(\varepsilon_{ij}, r_{ij}^{\min})$ are: default C36e and C36 = -0.09327, 3.41365;[72] fit = -0.2474, 3.341. I will discuss C36 results last, as these have different electrostatic parameters and cannot be used to compare LJ parameters.

The default C36e interactions are too favorable at short range; the interaction energy well is too deep and the close-range repulsion is shifted to the left and not as steep as the QM curve. Interactions at higher values of separation distance are dominated by electrostatics and not affected by changes in LJ parameters. The parameter ε_{ij} is very different in the two parameter sets, and as one would expect analytically, the larger absolute value of ε_{ij} used in the fit (~-0.25 fit vs. -0.093 default) increases short-range repulsion. While this would also result in a deeper LJ potential well, the interaction energy well is shallower for the fit compared to the default parameter set. The discrepancy can be explained by the fact that the interaction energies in Figure 41 are total interaction energies, not only LJ contributions. Except at very close range, electrostatic interactions are a greater contribution to the total energy than LJ interactions. Additionally, the supplied $r_{ij}^{\min}$ values do not correspond to the position of the well minimum. This is again because electrostatic

interactions dominate except at very short separation distances. While the fit shows much improvement, perhaps more would be seen with a more negative value of ε_{ij}; the lowest value tested was -0.25, near the final fit value.

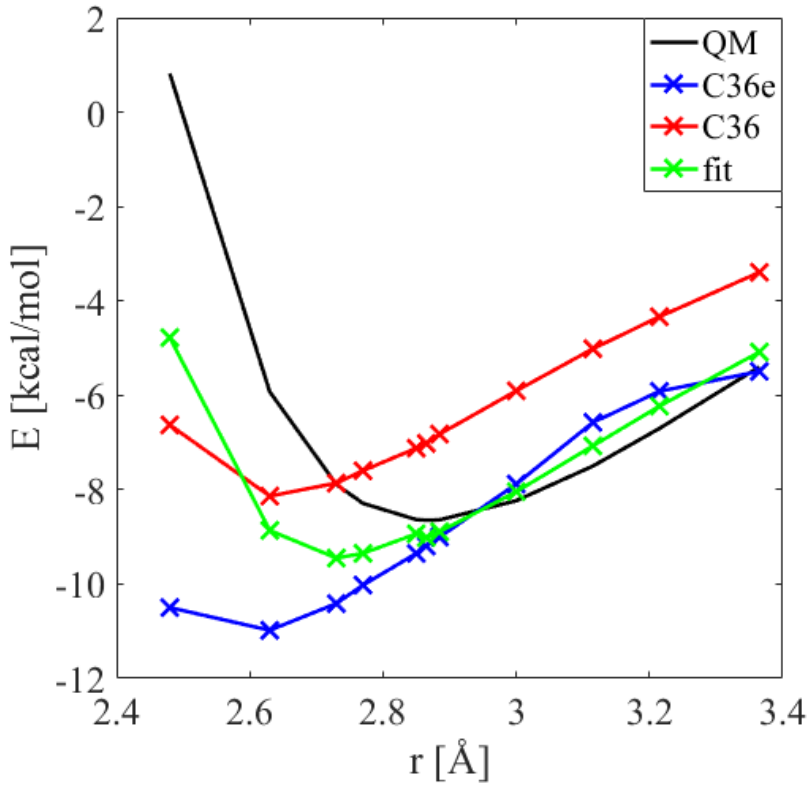

Figure 41. DEOE/K⁺ interaction energies as a function of separation distance.QM energies computed at MP2/def2TZVPP//MP2/def2QVZPP level using SMD implicit solvent model. MD energies represent an average over an ensemble of 100 minimized snapshots. Values for ($\varepsilon_{ij}, r_{ij}^{\min}$) are: default C36e and C36 = -0.09327, 3.41365;[72] fit = -0.2474, 3.341.

Interestingly, C36 parameters show poor long-range agreement with QM interaction energies (Figure 41, red), and because the LJ interaction energies are the same as with C36e, this difference is attributable to different partial charge assignments. It would not be possible to fit the QM interaction energy landscape with C36 partial charge parameters because electrostatic interactions dominate at large separation distances.

4.5.2. PEG radius of gyration from SANS experiments and MD simulations.

Theoretical dependence of solution conformations on salt concentration has been developed for polyelectrolytes[250, 251] and applied successfully to the interpretation of SAXS results for short nucleic acids in NaCl solutions from 12.5 mM to 1 M,[252] and to study the charge and salt dependence of dynamics of the charged polymer polyethylenimine (PEI).[253] The wormlike chain model predicts a decrease in R_g as a function of salt concentration at all protonation states for PEI caused by screening of the charges in the backbone as salt concentration increases, allowing the charged amines to be closer together and the polymer to exhibit more *gauche* character. This is quantified by a reduced electrostatic persistence length in the presence of electrolyte. Increase in the protonation state of PEI augments this effect.

Because PEG has zero net charge, this theory is not directly applicable to PEG in KCl solutions. However, recent QM results for linear ethers indicate significant polarity of the ether oxygens in PEG,[72] and one can conjecture that charge screening in concentrated salt solutions would result in a less pronounced decrease in PEG R_g. Indeed, R_g computed from SANS curves decreases from 12.7 to 11.3 Å in pure D_2O vs. 3 M KCl. SANS $I(q)$ curves are shown in Figure 42 along with the log curves used to compute R_g, which corresponds to the slope the best-fit line to the log curves.

Scattering curves computed from MD simulations with the C36e FF[72] are also shown in Figure 42. While the scattering curves do not agree quantitatively with experiment, the correct trend is seen: the slope of the curve for $q < 0.1$ Å is steeper in pure D_2O, indicating a larger R_g. Experimental curves in Figure 42 are for 0.05 w/vol. of PEG, and R_g was shown to decrease with increasing PEG concentration. Thus, the MD curve in

Figure 42 (top) is steeper than the experimental curve because PEG concentration is lower (yielding a more precise estimate of R_g). The MD curve in 3 M KCl is not steep enough, indicating underestimation of R_g.

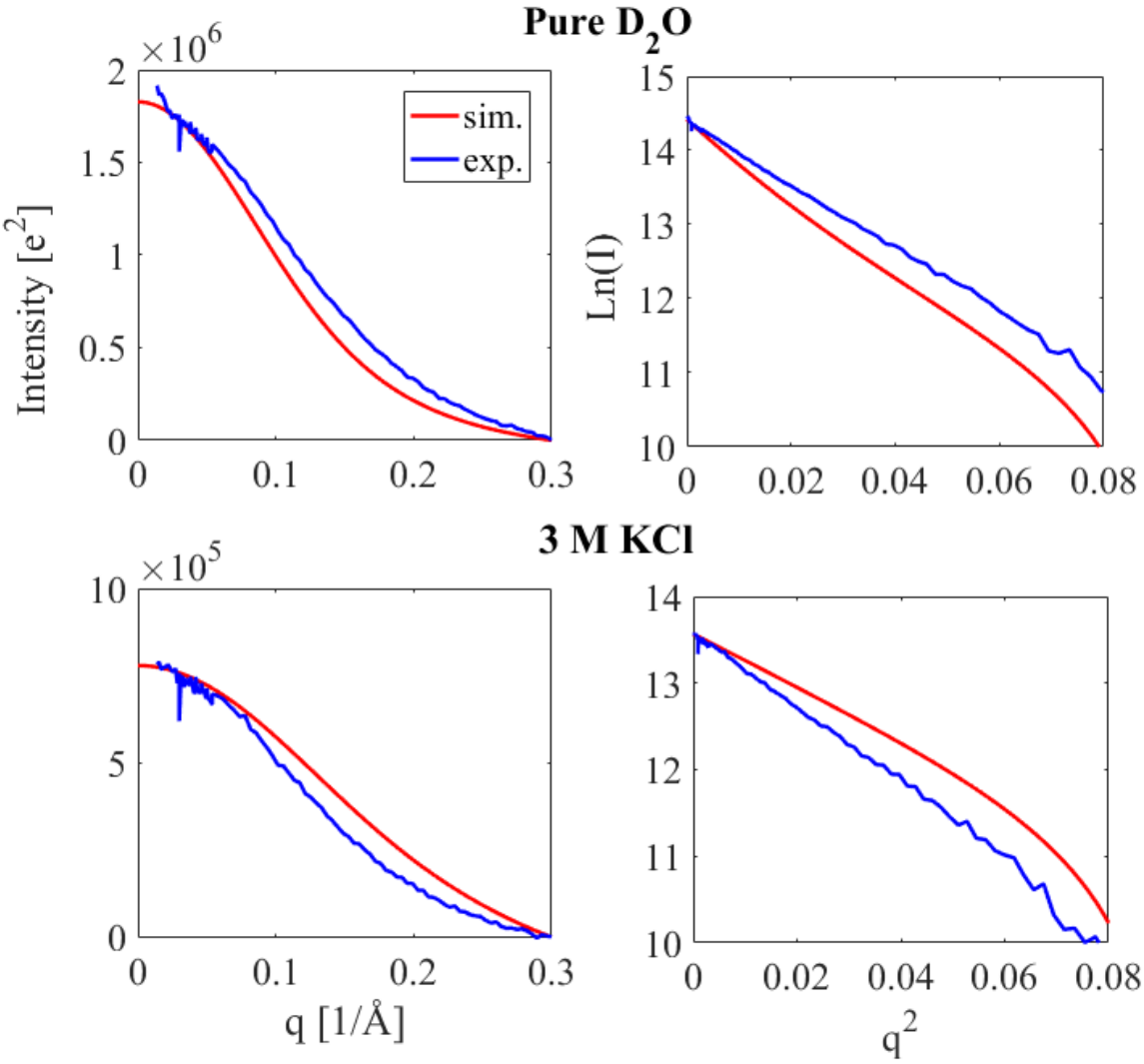

Figure 42. SANS intensity as a function of wave vector and $ln(I)$ vs. q^2. Experimental curves are at 0.05 w/vol. of PEG, whereas simulation curves represent infinite dilution. Curves are an average of three replicates. Simulations used C36e FF[72] and default LJ interaction parameters.

Figure 43 illustrates the geometry of PEG in pure water and 3 M KCl by comparing images formed from the superposition of 20 frames (snapshots collected over 40 ns). The 29-mer PEG is shown aligned along its short and long axes. Consistent with the larger R_g,

PEG has a longer end-to-end distance in pure water (22.56 Å) than in 3 M KCl (16.94 Å). As these measurements are of the polymer, not the polymer + water envelope, it is clear that KCl reduces the radius of gyration by changing PEG conformation. Indeed, in the "long axis" images, the polymer exhibits less density at each extremity in 3 M KCl than in pure water, and the "short axis" 3 M image is more spherical than the pure water image consistent with compaction of PEG in the presence of KCl.

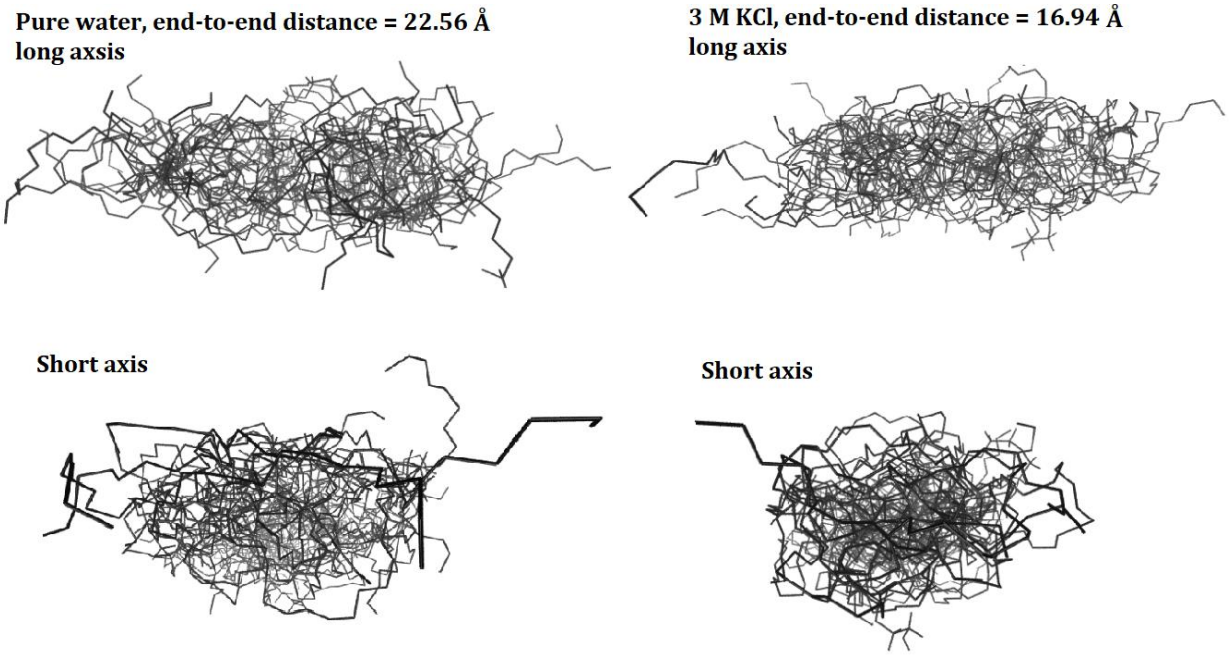

Figure 43. Configurations of a 29-mer PEG along its long and short axes. 20 superimposed frames in water and 3 M KCl, snapshots collected over 40 ns. End-to-end distances are listed. Axes determined by geometric distribution of atoms.

Figure 44 plots the experimental and MD R_g of a 29-mer PEG as a function of KCl concentration. Experimental values are linearly extrapolated to infinite dilution of PEG. R_g decreases slightly as KCl concentration increases. While the C36[81] and newer, QM-based C36e FF[72] both agree with experiment in pure D_2O, both FFs underestimate R_g in the presence of KCl with no statistical difference. Accounting for the hydration shell of PEG significantly increases the calculated R_g in the pure D_2O simulation, and based on PEG

O/water $g(r)$ in Figure 28, can be expected to increase R_g in simulations with KCl as well. This would bring simulation R_g in 1 M KCl very near the experimental value; however, R_g at 3 M KCl will likely be underestimated even with the hydration envelope included.

As indicated in Sec. 4.3.2, further analysis is needed to calculate R_g with inclusion of the hydration shell in simulations with KCl.

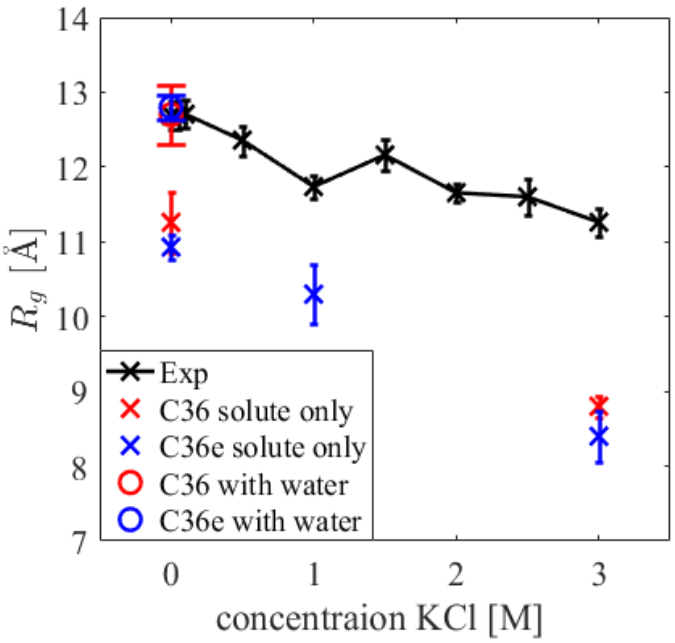

Figure 44. PEG R_g from simulation and experiment.

Table 25 compares results for different ether oxygen/K^+ LJ parameter sets. R_g is underestimated in all cases, and no clear trend in R_g results from changing either ε_{ij} or $r_{ij}^{\min}$. Rather, R_g for the solute only ranges from 9.68 – 10.2 Å in 1 M KCl and from 8.06 – 8.49 Å in 3 M KCl with nearly overlapping error bars. However, in all cases, the fraction of COCC *gauche* dihedrals is greater in 3 M than in 1 M KCl, and R_g is consequentially lower in 3 M KCl. The OCCO dihedrals strongly exhibit *gauche* conformation regardless of parameter set or salt concentration. Changing ether oxygen/K^+ parameters does not have a discernable effect on R_g. This can be explained by the low coordination of ether oxygens

with K^+ ions, indicated by the integral of the first peak of the ether oxygen/K^+ $g(r)$. For example, using the C36e default parameters (one of the most highly interacting sets), each ether oxygen coordinates only 0.002 nearest-neighbor K^+ ions on average in 1 M KCl. Direct binding between ether oxygen and potassium, which has a large atomic radius, is not common in solution.

Table 25. Structure of PEG and K^+; ether oxygen/ K^+ interaction parameters varied. Each entry contains results for 1 M KCl (top) and 3 M (bottom). Columns from left to right: 1) LJ interaction parameters; 2) R_g (Å) including water envelope; 3) R_g (Å) including only PEG; 4) fraction of OCCO and 5) COCC dihedrals in PEG presenting *gauche* conformation. Dihedrals were assigned to be *gauche* if they were greater than 125°, the position of the transition barriers in DEOE. 6) $g(r)$ peak positions (Å) and integrals for ether oxygen/ K^+ interactions.

$(\varepsilon_{ij}, r_{ij}^{\min})$	R_g		R_g, Solute only	Fraction OCCO *gauche**	Fraction COCC *gauche**	$g(r)$, ether oxygen/ K^+
-0.0932, 3.413	*1M KCl:*	9.9 ± 0.40	10.20 ± 0.31	0.949	0.320	2.87; .002
C36e default	*3M KCl:*	7.80 ± 0.34	8.38 ± 0.34	0.956	0.338	2.67; .012
-0.2474, 3.341			9.68 ± 0.21	0.957	0.318	2.81; .002
			8.49 ± 0.08	0.956	0.339	2.85; .007
-0.2474, 3.9			9.76 ± 0.09	0.957	0.328	3.37; .0002
			8.38 ± 0.10	0.957	0.333	3.37; .0006
-0.17, 3.341			10.01 ± 0.21	0.958	0.319	2.75; .0040
			8.46 ± 0.05	0.956	0.326	2.73; .0099
-0.17, 3.9			9.82 ± 0.12	0.954	0.329	3.37; .0002
			8.06 ± 0.07	0.955	0.339	3.37; .0009
Experiment		12.69 ± 0.19 11.26 ± 0.18				

The experimental decrease of R_g as a function of KCl concentration can therefore best be explained by charge shielding, not by the formation of crown-ether like structures or folding induced by ionic bonding. As KCl crowds PEG, which has highly polar oxygens carrying a partial charge of around -0.60e in vacuum *ab initio* calculations,[72] it shields these partial charges, allowing for shorter distances between ether oxygens accomplished by increased folding of PEG, exhibited by a greater fraction of COCC *gauche* dihedrals.

The water-water $g(r)$ peak position was found to be 2.79 Å for waters inside the solvation envelope of all simulations regardless of KCl concentration or the parameter set

used, identical to the peak position for modified TIP3P water in bulk.[254] Additionally, the PEG O/water $g(r)$ in Figure 28 show similar water structure in all simulations regardless of KCl concentration or parameter set. This indicates that changes in the local water shell in the presence of KCl do not contribute to the decrease in R_g.

4.6. Discussion

Previous attempts to parametrize ionic interactions for MD simulations focused primarily on ion solvation by water.[242, 255] More recently, a study by Lou and Roux[212] used osmotic pressure results for sodium and potassium chloride solutions at concentrations from 1 to 5 M to obtain the relevant $r_{ij}^{\min}$ parameters. This range of concentrations is a factor of 10 greater than physiologically-relevant concentrations and the question of how well these parameters represent dilute solutions remains. Additionally, such atom pair-specific adjustments were applied only to the CHARMM parameter $r_{ij}^{\min}$ and not to ε_{ij}.

Results reported by Venable et al.[213] indicate that $r_{ij}^{\min}$ interaction parameters for Na^+ and K^+ ions with lipid oxygens based on osmotic pressure data are reasonably transferable to simulations of anionic lipid bilayers. They found that use of osmotic pressure data to correct sodium and potassium overbinding to carboxylates in palmitoyloleoyl phosphatidylserine (POPS) membranes reduced deuterium order parameters of the palmitate chains, brining MD results in closer agreement with NMR results. However, they consider interactions of lower affinity. Experimental affinities of Be^{2+} with anionic phospholipids are in the micromolar range, which is most suitable for ITC.[256]

New LJ parameters for Be^{2+} improve agreement with solution and monohydrate properties obtained from experiment and QM, including free energy of hydration,

coordination number, and ion-monohydrate separation distance and interaction energy. While agreement in all measurements is within 10%, structural and energetic results are at odds, indicating the need for a more complex force field to describe solubility of this strongly-interacting ion. A study by Yang and Li[228] used QM calculations of ionic interactions with 1 – 7 water molecules to develop LJ parameters for Be^{2+}, Mg^{2+}, and Ca^{2+} to accompany their seven-site flexible water model with fluctuating charges. While results for Be^{2+} interaction energies and separation distances agreed well with QM results, the hydration shell for Be^{2+} was larger than expected in solution (5.8 water molecules), causing the authors to echo the conclusion that Be^{2+} requires a more complex treatment of nonbonded potential. Azam et al.[257] obtain accurate first hydration shell bond averages and coordination numbers using QM charge field molecular dynamics (QMCF/MD) to model a single hydrated Be^{2+} ion. QMCF/MD utilizes a partitioning scheme in which the system is divided into two parts. The chemically most relevant region, in this case the ion and first and second hydration shells, are treated by *ab initio* quantum mechanics. The remaining part of the system evolves under an empirical potential. This is computationally expensive relative to all-atom MD and restricts the focus of the simulation to the immediate vicinity of a particular reaction. The authors do not report solution energetics.

Use of the new Be^{2+} LJ parameters (given in Sec. 3.2) in solution simulations with components of PS result in initial overbinding to both acetate and dimethyl phosphate, causing clustering. The CGEN FF model for soluble acetate[135] exhibits the most overbinding to Be^{2+} before parameter adjustment, binding even more tightly than to DMP. The carboxylate model based on the lipid FF, which carries a lesser partial charge on the

free oxygen (-0.67 rather than -0.76), still exhibits overbinding. Adjustment of the LJ interaction parameter $r_{ij}^{\min}$ sufficiently reduces binding to all small molecules in solution.

Pair correlation functions directly reflect association probabilities and together with free energy calculations provide a statistical accounting for the free energy of binding in solution. The free energies of Be^{2+} interaction with water and dimethyl phosphate in solution are similar; free energy of hydration is -572 kcal/mol,[227] and binding to dimethyl phosphate is -6.49 kcal/mol more favorable. Parameterization of Be^{2+}-oxygen interactions is therefore a fine-tuning of two reactions with similar affinities, hydration and binding in solution. We found that even in a saturated solution, a single Be^{2+} ion associates with only one or two dimethyl phosphate molecules and maintains associations with water. Associations with acetate in solution are considerably weaker. A Be^{2+} ion may associate with a single acetate molecule, and dissociations are frequent. Final LJ interaction parameters describing Be^{2+}-phosphate and -acetate binding agree well with the equilibrium constants for these reactions found from ITC experiments.

Surface tensions of DOPS monolayers, recorded in Langmuir experiments, depend on salt species and concentration in the subphase. Relative to Ca^{2+}, which has a larger atomic radius, and to monovalent K^+, Be^{2+} has a compacting effect on DOPS monolayers in these experiments.[23] Revised interaction parameters for Be^{2+} with phosphate and carboxylate oxygens reproduce experimental surface tensions for DOPS monolayers and show compaction relative to monolayers equilibrated with K^+. In these simulations, Be^{2+} preferentially associates with phosphate oxygens and maintains associations with water, which penetrates the monolayer. While some associations between Be^{2+} and carboxylates

are present in simulations with 65.3 Å^2/lipid (equivalent to experimental A_l at 303.15 K),[245] less condensed monolayers (71.6 Å^2/lipid) show no associations with carboxylates.

The new parameters for Be^{2+} developed in this chapter open possibilities of realistic modeling of multiple biochemical processes where we expect interference of this small dication underlying its toxicity. This includes competition between Ca^{2+} and Be^{2+} at the surface of phosphatidylserine-containing membranes and domains, Be^{2+} interference with phosphatidylserine recognition by its receptors on macrophages, components of coagulation cascade, and Ca^{2+}-dependent membrane fusion machinery. A few more steps will be required for full parametrization of this cation for simulations with proteins.

Continuing investigation into pair-specific interaction parameters, we found QM interaction energies for K^+ with ether oxygens of DEOE. Comparison with interaction energies from MD simulations using the default LJ interaction parameters indicate that the shape of the energy landscape is poorly represented if only $r_{ij}^{\min}$ is adjusted; perhaps quantities like binding energies or osmotic pressures can be reproduced in this manner, but specific balance of near and far field interaction energies can be accomplished by fitting both ($\varepsilon_{ij}, r_{ij}^{\min}$) LJ interaction parameters simultaneously.

The R_g of 29-mer PEG in varying concentrations of KCl was found from SANS experiments. The new C36e parameter set for linear ethers introduced in Chapter 3[72] shows quantitative agreement with experimental R_g in pure D_2O if the hydration envelope is considered. Inclusion of the hydration envelope is expected to bring estimates of R_g near to experimental values in KCl solutions up to 1 M. Examination of water-water $g(r)$ peak position in the vicinity of PEG and the *gauche* character and end-to-end distances of the polymer indicate that KCl dependence of R_g is caused by increased folding, not by altered

water structure in the presence of KCl. R_g in KCl solutions is not directly affected by changing K^+/ether oxygen interaction parameters; no significant change was found in R_g in simulations with different ($\varepsilon_{ij}, r_{ij}^{\min}$) parameters for K^+/ether oxygen, perhaps because this interaction is weak.

Future analysis will include the quantification of the contribution of bound water to the computed scattering intensity $I(q)$ in MD simulations at 1 and 3 M KCl; calculation of the electrostatic persistence length of the PEG in water, 1, and 3 M KCl to determine whether persistence length is reduced by KCl; and application of new C36e ether parameters to the Drude polarizable FF to see if treatment of atomic polarizability improves PEG/ion interactions.

Chapter 5. Conclusions and Impact

This dissertation addresses three impactful issues in current lipid FF development: lipid diversity, lipid-ion interactions, and treatment of long-range LJ forces. Current lipid FF development aims to increase lipid diversity so that membrane simulations can model biological compositions. Accurate representation of lipid-ion interactions is essential to capture biological processes, such as ion-mediated signaling pathways and cell adhesion. The presence of ions also affects bilayer properties such as the bilayer dipole potential, which in turn affects protein folding. Long-range LJ interactions significantly impact the surface tension and compressibility of apolar liquids and can therefore be assumed to affect structure and dynamics of hydrophobic lipid tails; however, inclusion of long-range LJ interactions has been theoretically difficult because of bilayer anisotropy. Each of these FF development issues presents a parameterization challenge arising from the unique chemical properties of phospholipids, which contain polar headgroups and apolar, highly flexible tails.

The body of research contained in this dissertation therefore addresses each issue with chemical specificity. Accurate representation of the dihedral energy landscape of DEOE from QM calculations, for example, increases the transferability of the dihedral parameters compared to parameters derived from a limited set of experimental results (although FF validation is obtained by reproducing experimental results). QM interaction energies were considered in fitting Be^{2+} LJ parameters, and the effects of atomic polarizability on properties of hexadecane were investigated in the validation of LJ-PME for Drude vs. the C36 additive FF.

The availability of LJ-PME to the CHARMM community and the validation of this method presented in Chapter 2 is an initial step in the reparameterization of the C36 and Drude lipid FFs to include long-range LJ interactions. The current C36 FF achieves accurate properties with zero surface tension for symmetric bilayers, but consistently underestimates surface tensions of monolayers. For example, at a monolayer coverage of 64 $Å^2$/lipid C36 predicts 26.4±1.0 dyn/cm for DPPC, whereas experiment is 40.9 dyn/cm.[34] Including long-range LJ interactions, the agreement with experiment is within statistical error. This result is not satisfactory because one should not require different methods to represent long-range LJ forces when simulating a bilayer versus a monolayer. This suggests there is an inherent dependence on cutoff with the C36 lipid FF (and other FFs similarly parameterized). Reparameterization of lipids with LJ-PME would eliminate this dependence. Data from MD simulations presented in Chapter 2 validate the use of LJ-PME in systems of pure alkanes, but preliminary results indicate the bilayers condense when long-range LJ interactions are included. Reparameterization with LJ-PME is needed to achieve consistency in modeling monolayers and bilayers.

LJ-PME brings the dynamical properties of viscosity and diffusion closer to experiment, as consistent with an increase in density. Without LJ-PME, both C36 and the polarizable Drude FF underestimate viscosity and overestimate diffusion. Inclusion of long-range LJ forces also improves the temperature dependence of molar volume and area compressibility of alkanes, achieving better agreement with experiment at and above 330 K, important for simulations using enhanced sampling at higher temperatures such as replica exchange. Use of the polarizable Drude FF further increases agreement at higher temperatures. This advantage in temperature dependence is consistent with previous

results: polarizable FF generally perform better than additive FF at elevated temperatures in systems of pure water,[138] water/salt solutions,[139] and polypeptides.[140] A likely explanation for this is the increase in degrees of freedom, allowing greater responsiveness of the polarizable systems to temperature fluctuations.

In addition to improving agreement with the experimental properties evaluated for alkanes, LJ-PME robustly calculates long-range LJ interactions for anisotropic systems such as an alkane-air interface. Figure 6 shows that increasing r_{cut} causes ρ to converge to the value obtained using LJ-PME, indicating that LJ-PME treats the long-range dispersion forces accurately.

The new FF for linear ethers and ether lipids resulting from research presented in Chapter 3, called C36e, expands the lipid repertoire of the C36 FF to include the biologically prevalent ether linkage. Ether-linked lipids in the human body are typically plasmalogens, characterized by an ether bond in position *sn*-1 to an alkenyl group. Ethanolamine plasmalogens such as PLAPE (also introduced in Chapter 3) present in high concentrations in brain, retina and other neural tissues.[158-161]

Recent experimental findings verify that the ether linkage alters bilayer structure, water permeability,[150] and water organization in the bilayer.[151] For example, ether-linked DHPC has a higher A_l than its ester-linked counterpart, DPPC. However, previous attempts to model the glycerol-ether linkage resulted in underestimation of A_l and otherwise inaccurate representation of the scattering density profile.[258, 259] The new C36e FF appropriately yields a higher A_l for DHPC than for DPPC and improved agreement with the experimental scattering density profile.

An interesting result from QM calculations of linear ethers in the same study is that in longer chained polyethers such as PEG, the ether oxygen carries substantial negative partial charge (~-0.6*e*) and bonded carbons carry notable positive charge (~0.4*e*). It is the polar nature of the ether oxygen that enables PEG's many uses in industry and medicine. C36e accurately models the partial charges and dihedral landscape of linear ethers, a distinct improvement over C36. An important next step is to apply these parameters to the Drude polarizable FF, which ascribes nearly neutral partial charges to linear ethers such as DMOE (originally parameterized with purely empirical targets).[81]

While the C36e FF improves agreement with experimental structural properties for a pure DHPC bilayer, it does not reproduce the experimental trend of reduced dipole potential across the ether bilayer relative to a DPPC bilayer. Arguably the only way to reproduce this sensitive value is to include atomic polarization. FF models based on a nonpolarizable energy function, such as fixed-charge models, have the inherent limitation of underestimating the dielectric constants of nonpolar systems. For example, using the C27r FF, the dielectric constant of decane at its boiling point is 1.02, whereas with the Drude polarizable force field it is 2.06, very near to the experimental value of 1.97. A likely result of the improved dielectric constant of alkanes, the original Drude model for DPPC showed a reduction in membrane dipole potential to a value of 380 mV (relative to ~800 mV in C36 vs. experimental estimates of 220 – 280 mV[200]). The primary contribution to the decrease in dipole potential can be attributed to improved representation of interfacial electrostatic interactions modulated by the dielectric constant of the hydrophobic tails. However, the improvement seen in the dipole potential of the original Drude DPPC model[73] is lost with the updated lipid Drude model, which yields a potential drop of 560

mV.[76] While the Drude FF for lipids may in the future be able to more accurately represent electrostatic potential, further parametrization is needed to bring this FF in closer agreement with experimental values for these properties.

Chapter 4 uses various experimental and QM techniques to characterize lipid-ion interactions. Lipid-ion interactions are thought to affect many properties of bilayers, including dipole potential drop, water dipole orientation, and charge distribution.[203] In addition to ion-water interactions, which are optimized in selection of atom-type LJ parameters to reproduce interactions with water, specific ion-lipid interactions should be considered. The CHARMM community has used osmotic pressure data to prescribe interaction parameters.[212] This method has been successful in parameterizing nonbonded ionic interactions in bulk. While the application of osmotic pressure data to Na^+ interactions with lipids resulted in improvement of deuterium order parameters for DMPG membranes, in the case of the POPS membrane, which presents two binding sites to Na^+ (phosphate and acetate oxygen), resulting order parameters leave room for improvement.[213] This suggests the need for further investigation in ion-lipid parameterization.

One approach is to include more experimental data as parameterization targets. The use of isothermal titration calorimetry to find binding affinities of Be^{2+} with PS component molecules introduces a novel method to characterize nearest-neighbor interactions as would be expected between this highly interacting divalent ion and PS binding sites. Theoretical advances in ITC data interpretation enable the extension of this method to competition[260] and low-affinity reactions.[261] While the fitting procedure used in Chapter 4 to develop LJ interaction parameters involves accounting for the ensemble of binding configurations in simulation and can require many iterations, use of model compounds with

a single binding site simplifies fitting. While not investigated here, other experimental data exhibiting ion dependence or ion binding could potentially be used as target data for fitting LJ interaction parameters, such as partial molar volumes of interacting species in solution.

Results for Be^{2+} LJ parameters presented in Chapter 4 agree well with both QM and experimental results for interactions with water (Table 17). Additionally, LJ interaction parameters between Be^{2+} and PS components reproduce experimental binding constants. ITC results show overwhelming preference of Be^{2+} to bind with dimethyl phosphate relative to acetate. Use of the new interaction parameters in DOPS monolayer simulations reproduce Be^{2+} concentration dependence of monolayer surface tensions and experimental compaction of DOPS monolayers in solution with $BeSO_4$ relative to KCl.

Sections 4.3 and 4.5, investigation of PEG interactions with K^+ in solution, make use of the new ether FF introduced in Chapter 3. Experimental SANS data for a 29-mer PEG in KCl solution show that, while the C36e FF agrees with experiment for the R_g of PEG in pure D_2O including the water envelop, R_g is underestimated in 3 M KCl. Local water structure is unaffected by KCl, and K^+ does not associate closely enough with the ether oxygen to form crown-ether like structures. The dependence of R_g on KCl concentration can be attributed to increased *gauche* character of the COCC dihedral (whereas the OCCO dihedral exhibited overwhelming *gauche* character regardless of KCl concentration). A possible explanation for the KCl dependence of PEG R_g is charge shielding. The polar nature of the ether oxygen may maintain more COCC *trans* configurations unless shielded by K^+ ions in solution.

Due to the polar nature of PEG and the importance of electron density distributions in ionic interactions, this problem could be treated with a polarizable FF. Future efforts

will include introducing a Drude model for PEG adapted from the C36e FF and quantitatively accounting for the effect of the hydration shell around PEG in simulations with KCl.

The anisotropic nature of phospholipids presents many challenges to FF development. Achieving chemical specificity consistent with both polar and hydrophobic interactions requires a balance of electrostatic and entropic forces. For best transferability, parameterization should be as chemically specific as possible, incorporating QM results for close interactions and torsions when possible and multiple experimental observables to characterize solution and bilayer properties. Accurate calculation of long-range LJ interactions not only improves thermodynamic properties such as compressibility and surface tension of alkanes, but also increases transferability: much improvement is seen in temperature dependence of molar volumes and isothermal compressibilities of hexadecane. The Drude FF, which accounts for atomic polarizability and thereby increases a system's degrees of freedom, also improves temperature dependence of these quantities for alkanes and shows promise of improving agreement with experimental estimates of bilayer dipole potential drop.

Bilayers have both polar and apolar regions requiring accurate treatment of LJ interactions to ensure proper force balance (electrostatic vs. hydrophobic) and inclusion of atomic polarizability to achieve proper energetics of transfer between polar and apolar regions. Research in this dissertation demonstrates the need for a careful reparameterization of the Drude lipid FF to include LJ-PME. Chemical specificity in both parameterization and treatment of forces improves FF accuracy and transferability. While ever-increasing FF diversity and time and length scales of simulations enable MD

simulations to model biological membranes, chemical specificity becomes increasingly important to ensure these complex systems accurately represent molecular interactions.

Funding and Computational Resources

This research was supported by the Intramural Research Program of the NIH, National Heart, Lung and Blood Institute, NSF Grant MCB-1149187, and the use of the high-performance computational capabilities at the National Institutes of Health, Bethesda, MD (NHLBI LoBoS and Biowulf clusters), the Maryland Advanced Research Computing Center (MARCC), and the University of Maryland (Deepthought2, http://hpcc.umd.edu).

References

1. Arai, Y.; Shibata, T.; Matsuoka, S.; Sato, M.J.; Yanagida, T.; Ueda, M. Self-Organization of the Phosphatidylinositol Lipids Signaling System for Random Cell Migration. *Proc. Natl. Acad. Sci.* **2010**, *107*, 12399 12404.
2. Cevc, G. How Membrane Chain-Melting Phase-Transition Temperature Is Affected by the Lipid Chain Asymmetry and Degree of Unsaturation: An Effective Chain-Length Model. *Biochemistry*. **1991**, *30*, 7186-7193.
3. Marsh, D. Structural and Thermodynamic Determinants of Chain-Melting Transition Temperatures for Phospholipid and Glycolipids Membranes. *Biochim. Biophys. Acta, Biomembr.* **2010**, *1798*, 40-51.
4. Baenziger, J.E.; Jarrell, H.C.; Hill, R.J.; Smith, I.C. Average Structural and Motional Properties of a Diunsaturated Acyl Chain in a Lipid Bilayer: Effects of Two Cis-Unsaturated Double Bonds. *Biochemistry*. **1991**, *30*, 894-903.
5. Seelig, A.; Seelig, J. The Dynamic Structure of Fatty Acyl Chains in a Phospholipid Bilayer Measured by Deuterium Magnetic Resonance. *Biochemistry*. **1974**, *13*, 4839-4845.
6. Rawicz, W.; Olbrich, K.C.; McIntosh, T.; Needham, D.; Evans, E. Effect of Chain Length and Unsaturation on Elasticity of Lipid Bilayers. *Biophys. J.* **2000**, *79*, 328-339.
7. Sodt, A.J.; Pastor, R.W. Bending Free Energy from Simulation: Correspondence of Planar and Inverse Hexagonal Lipid Phases. *Biophys. J.* **2013**, *104*, 2202-2211.
8. Sodt, Alexander J.; Pastor, Richard W. Molecular Modeling of Lipid Membrane Curvature Induction by a Peptide: More Than Simply Shape. *Biophys. J.* **2014**, *106*, 1958-1969.
9. Hofsäß, C.; Lindahl, E.; Edholm, O. Molecular Dynamics Simulations of Phospholipid Bilayers with Cholesterol. *Biophys. J.* **2003**, *84*, 2192-2206.
10. de Almeida, R.F.; Fedorov, A.; Prieto, M. Sphingomyelin/Phosphatidylcholine/Cholesterol Phase Diagram: Boundaries and Composition of Lipid Rafts. *Biophys. J.* **2003**, *85*, 2406-2416.
11. Sodt, A.J.; Pastor, R.W.; Lyman, E. Hexagonal Substructure and Hydrogen Bonding in Liquid-Ordered Phases Containing Palmitoyl Sphingomyelin. *Biophys. J.* **2015**, *109*, 948-955.
12. Holthuis, J.C.M.; Menon, A.K. Lipid Landscapes and Pipelines in Membrane Homeostasis. *Nature*. **2014**, *510*, 48-57.
13. van Meer, G.; Voelker, D.R.; Feigenson, G.W. Membrane Lipids: Where They Are and How They Behave. *Nat. Rev. Mol. Cell Biol.* **2008**, *9*, 112-124.
14. Lee, T.-c. Biosynthesis and Possible Biological Functions of Plasmalogens. *Biochim. Biophys. Acta, Lipid Metab.* **1998**, *1394*, 129-145.
15. Obrien, J.S.; Sampson, E.L. Lipid Composition of Normal Human Brain - Gray Matter White Matter and Myelin. *J. Lipid Res.* **1965**, *6*, 537-&.
16. Manno, S.; Takakuwa, Y.; Mohandas, N. Identification of a Functional Role for Lipid Asymmetry in Biological Membranes: Phosphatidylserine-Skeletal Protein Interactions Modulate Membrane Stability. *Proc. Natl. Acad. Sci. U.S.A.* **2002**, *99*, 1943-1948.
17. Tang, X.; Halleck, M.S.; Schlegel, R.A.; Williamson, P. A Subfamily of P-Type Atpases with Aminophospholipid Transporting Activity. *Science (NY)*. **1996**, *272*, 1495 - 1497.
18. Paila, Y.D.; Chattopadhyay, A., *Membrane Cholesterol in the Function and Organization of G-Protein Coupled Receptors*, in *Cholesterol Binding and Cholesterol Transport Proteins:*. 2010, Springer Netherlands : Dordrecht, 439-466.

19. Vanni, S.; Vamparys, L.; Gautier, R.; Drin, G.; Etchebest, C.; Fuchs, P.F.; Antonny, B. Amphipathic Lipid Packing Sensor Motifs: Probing Bilayer Defects with Hydrophobic Residues. *Biophys. J.* **2013**, *104*, 575-584.
20. Trauble, H.; Eibl, H. Electrostatic Effects on Lipid Phase Transitions: Membrane Structure and Ionic Environment. *Proc. Natl. Acad. Sci. U.S.A.* **1974**, *71*, 214-219.
21. Hodgkin, A.L.; Horowicz, P. The Influence of Potassium and Chloride Ions on the Membrane Potential of Single Muscle Fibres. *J. Physiol.* **1959**, *148*, 127-160.
22. Song, J.; Franck, J.; Pincus, P.; Kim, M.W.; Han, S. Specific Ions Modulate Diffusion Dynamics of Hydration Water on Lipid Membrane Surfaces. *J. Am. Chem. Soc.* **2014**, *136*, 2642-2649.
23. Ermakov, Y.A.; Kamaraju, K.; Dunina-Brkovskaya, A.; Vishnyakova, K.S.; Yegorov, Y.E.; Anishkin, A.; Sukharev, S. High-Affinity Interactions of Beryllium(2+) with Phosphatidylserine Result in a Cross-Linking Effect Reducing Surface Recognition of the Lipid. *Biophys. J.* **2017**, *56*, 5457 - 5470.
24. Bhattacharya, S.; Vaidehi, N. Differences in Allosteric Communication Pipelines in the Inactive and Active States of a Gpcr. *Biophys. J.* **2014**, *107*, 422-434.
25. Safran, S.A. *Statistical Thermodynamics of Surfaces, Interfaces, and Membranes*. Frontiers in Physics Vol. 90. Addison-Wesley Pub.: Reading, Mass. 1994; 270.
26. Nagle, J.F.; Tristram-Nagle, S. Structure of Lipid Bilayers. *Biochim. Biophys. Acta-Rev. Biomembr.* **2000**, *1469*, 159-195.
27. Boughter, C.T.; Monje-Galvan, V.; Im, W.; Klauda, J.B. Influence of Cholesterol on Phospholipid Bilayer Structure and Dynamics. *J. Phys. Chem. B.* **2016**, *120*, 11761-11772.
28. Zhuang, X.; Makover, J.; Im, W.; Klauda, J.B. A Systematic Molecular Dynamics Simulation Study of Temperature Dependent Bilayer Structural Properties. *Biochim. Biophys. Acta, Biomembr.* **2014**, *1838*, 2520-2529.
29. Zhuang, X.; Davila-Contreras, E.M.; Beaven, A.H.; Im, W.; Klauda, J.B. An Extensive Simulation Study of Lipid Bilayer Properties with Different Head Groups, Acyl Chain Lengths, and Chain Saturations. *Biochim. Biophys. Acta-Biomembr.* **2016**, *1858*, 3093-3104.
30. Ghysels, A.; Venable, R.M.; Pastor, R.W.; Hummer, G. Position-Dependent Diffusion Tensors in Anisotropic Media from Simulation: Oxygen Transport in and through Membranes. *J. Chem. Theory Comput.* **2017**, *13*, 2962-2976.
31. Venable, R.M.; Sodt, A.J.; Rogaski, B.; Rui, H.; Hatcher, E.; MacKerell, A.D.; Pastor, R.W.; Klauda, J.B. CHARMM All-Atom Additive Force Field for Sphingomyelin: Elucidation of Hydrogen Bonding and of Positive Curvature. *Biophys. J.* **2014**, *107*, 134-145.
32. Brooks, B.R.; Bruccoleri, R.E.; Olafson, B.D.; States, D.J.; Swaminathan, S.; Karplus, M. CHARMM - a Program for Macromolecular Energy, Minimization, and Dynamics Calculations. *J. Comput. Chem.* **1983**, *4*, 187-217.
33. Brooks, B.R.; Brooks, C.L.; Mackerell, A.D.; Nilsson, L.; Petrella, R.J.; Roux, B.; Won, Y.; Archontis, G.; Bartels, C.; Boresch, S.; Caflisch, A.; Caves, L.; Cui, Q.; Dinner, A.R.; Feig, M.; Fischer, S.; Gao, J.; Hodoscek, M.; Im, W.; Kuczera, K.; Lazaridis, T.; Ma, J.; Ovchinnikov, V.; Paci, E.; Pastor, R.W.; Post, C.B.; Pu, J.Z.; Schaefer, M.; Tidor, B.; Venable, R.M.; Woodcock, H.L.; Wu, X.; Yang, W.; York, D.M.; Karplus, M. CHARMM: The Biomolecular Simulation Program. *J. Comput. Chem.* **2009**, *30*, 1545-1614.
34. Klauda, J.B.; Venable, R.M.; Freites, J.A.; O'Connor, J.W.; Mondragon-Ramirez, C.; Vorobyov, I.; Tobias, D.J.; MacKerell, A.D.; Pastor, R.W. Update of the CHARMM All-Atom Additive Force Field for Lipids: Validation on Six Lipid Types. *J. Phys. Chem. B.* **2010**, *114*, 7830-7843.

35. Guvench, O.; Mallajosyula, S.S.; Raman, E.P.; Hatcher, E.; Vanommeslaeghe, K.; Foster, T.J.; Jamison, F.W.; MacKerell, A.D. CHARMM Additive All-Atom Force Field for Carbohydrate Derivatives and Its Utility in Polysaccharide and Carbohydrate–Protein Modeling. *J. Chem. Theory Comput.* **2011**, *7*, 3162-3180.
36. Mallajosyula, S.S.; Guvench, O.; Hatcher, E.; MacKerell, A.D. CHARMM Additive All-Atom Force Field for Phosphate and Sulfate Linked to Carbohydrates. *J. Chem. Theory Comput.* **2012**, *8*, 759-776.
37. Raman, E.P.; Guvench, O.; MacKerell, A.D. CHARMM Additive All-Atom Force Field for Glycosidic Linkages in Carbohydrates Involving Furanoses. *J. Phys. Chem. B.* **2010**, *114*, 12981-12994.
38. Guvench, O.; Hatcher, E.; Venable, R.M.; Pastor, R.W.; MacKerell, A.D. CHARMM Additive All-Atom Force Field for Glycosidic Linkages between Hexopyranoses. *J. Chem. Theory Comput.* **2009**, *5*, 2353-2370.
39. Denning, E.J.; Priyakumar, U.D.; Nilsson, L.; Mackerell, A.D. Impact of 2′-Hydroxyl Sampling on the Conformational Properties of Rna: Update of the CHARMM All-Atom Additive Force Field for Rna. *J. Comput. Chem.* **2012**, *32*, 1929-1943.
40. Hart, K.; Foloppe, N.; Baker, C.M.; Denning, E.J.; Nilsson, L.; MacKerell, A.D. Optimization of the CHARMM Additive Force Field for DNA: Improved Treatment of the BI/BII Conformational Equilibrium. *J. Chem. Theory Comput.* **2012**, *8*, 348-362.
41. Huang, J.; Rauscher, S.; Nawrocki, G.; Ran, T.; Feig, M.; de Groot, B.L.; Grubmüller, H.; MacKerell Jr, A.D. Charmm36m: An Improved Force Field for Folded and Intrinsically Disordered Proteins. *Nat. Methods*. **2016**, *14*, 71-73.
42. Huang, J.; MacKerell, A.D. CHARMM36 All-Atom Additive Protein Force Field: Validation Based on Comparison to NMR Data. *J. Comput. Chem.* **2013**, *34*, 2135-2145.
43. Patel, S.; Brooks, C.L. CHARMM Fluctuating Charge Force Field for Proteins: I Parameterization and Application to Bulk Organic Liquid Simulations. *J. Comput. Chem.* **2004**, *25*, 1-15.
44. Patel, S.; Mackerell, A.D.; Brooks, C.L. CHARMM Fluctuating Charge Force Field for Proteins: Ii - Protein/Solvent Properties from Molecular Dynamics Simulations Using a Nonadditive Electrostatic Model. *J. Comput. Chem.* **2004**, *25*, 1504-1514.
45. Patel, S.A.; Brooks, C.L. Revisiting the Hexane-Water Interface via Molecular Dynamics Simulations Using Nonadditive Alkane-Water Potentials. *J. Chem. Phys.* **2006**, *124*, 204706.
46. Davis, J.E.; Warren, G.L.; Patel, S. Revised Charge Equilibration Potential for Liquid Alkanes. *J. Phys. Chem. B.* **2008**, *112*, 8298-8310.
47. Lamoureux, G.; Roux, B. Modeling Induced Polarization with Classical Drude Oscillators: Theory and Molecular Dynamics Simulation Algorithm. *J. Chem. Phys.* **2003**, *119*, 3025-3039.
48. Anisimov, V.M.; Lamoureux, G.; Vorobyov, I.V.; Huang, N.; Roux, B.; MacKerell, A.D. Determination of Electrostatic Parameters for a Polarizable Force Field Based on the Classical Drude Oscillator. *J. Chem. Theory Comput.* **2005**, *1*, 153-168.
49. Darden, T.; York, D.; Pedersen, L. Particle Mesh Ewald - an Nlog(N) Method for Ewald Sums in Large Systems. *J. Chem. Phys.* **1993**, *98*, 10089-10092.
50. Venable, R.M.; Zhang, Y.H.; Hardy, B.J.; Pastor, R.W. Molecular-Dynamics Simulations of a Lipid Bilayer and of Hexadecane - an Investigation of Membrane Fluidity. *Science (NY)*. **1993**, *262*, 223-226.
51. Schlenkrich, M.; Brickmann, J.; MacKerell, A.D.; Karplus, M., *An Empirical Potential Energy Function for Phospholipids: Criteria for Parameter Optimization and Applications*, in *Biological Membranes: A Molecular Perspective from Computation and Experiment*, K.M. Merz and B. Roux, Editors. 1996, Birkhäuser Boston: Boston, MA, 31-81.

52. Feller, S.E.; Yin, D.X.; Pastor, R.W.; MacKerell, A.D., Jr. Molecular Dynamics Simulation of Unsaturated Lipid Bilayers at Low Hydration: Parameterization and Comparison with Diffraction Studies. *Biophys. J.* **1997**, *73*, 2269-2279.
53. Feller, S.E.; MacKerell, A.D., Jr. An Improved Empirical Potential Energy Function for Molecular Simulations of Phospholipids. *J. Phys. Chem. B.* **2000**, *104*, 7510-7515.
54. Jorgensen, W.L.; Chandrasekhar, J.; Madura, J.D.; Impey, R.W.; Klein, M.L. Comparison of Simple Potential Functions for Simulating Liquid Water. *J. Chem. Phys.* **1983**, *79*, 926-935.
55. Durell, S.R.; Brooks, B.R.; Bennaim, A. Solvent-Induced Forces between Two Hydrophilic Groups. *J. Phys. Chem.* **1994**, *98*, 2198-2202.
56. Yin, D.X.; MacKerell, A.D. Ab Initio Calculations on the Use of Helium and Neon as Probes of the Van Der Waals Surfaces of Molecules. *J. Phys. Chem.* **1996**, *100*, 2588-2596.
57. Yin, D.X.; MacKerell, A.D., Jr. Combined ab Initio Empirical Approach for Optimization of Lennard-Jones Parameters. *J. Comput. Chem.* **1998**, *19*, 334-348.
58. Klauda, J.B.; Venable, R.M.; MacKerell, A.D.; Pastor, R.W., *Considerations for Lipid Force Field Development*, in *Computational Modeling of Membrane Bilayers*, E.F. Scott, Editor. 2008, Elsevier: London, UK, 1-48.
59. Klauda, J.B.; Brooks, B.R.; MacKerell, A.D.; Venable, R.M.; Pastor, R.W. An ab Initio Study on the Torsional Surface of Alkanes and Its Effect on Molecular Simulations of Alkanes and a DPPC Bilayer. *J. Phys. Chem. B.* **2005**, *109*, 5300-5311.
60. Kang, H.; Klauda, J.B. Molecular Dynamics Simulations of Palmitoyloleoylphosphatidylglycerol Bilayers. *Mol. Simul.* **2015**, *41*, 948-954.
61. Wu, Emilia L.; Fleming, Patrick J.; Yeom, Min S.; Widmalm, G.; Klauda, Jeffery B.; Fleming, Karen G.; Im, W. E. coli Outer Membrane and Interactions with OmpLA. *Biophys. J.* **2014**, *106*, 2493-2502.
62. Jo, S.; Wu, E.L.; Stuhlsatz, D.; Klauda, J.B.; MacKerell, A.D.; Widmalm, G.; Im, W., *Lipopolysaccharide Membrane Building and Simulation*, in *Glycoinformatics: Methods in Molecular Biology*, J.M. Walker, Editor. 2015, Springer Science: New York, 391-406.
63. Kim, S.; Patel, Dhilon S.; Park, S.; Slusky, J.; Klauda, Jeffery B.; Widmalm, G.; Im, W. Bilayer Properties of Lipid a from Various Gram-Negative Bacteria. *Biophys. J.* **2016**, *111*, 1750-1760.
64. Patel, Dhilon S.; Park, S.; Wu, Emilia L.; Yeom, Min S.; Widmalm, G.; Klauda, Jeffery B.; Im, W. Influence of Ganglioside GM1 Concentration on Lipid Clustering and Membrane Properties and Curvature. *Biophys. J.* **2016**, *111*, 1987-1999.
65. Wang, E.; Klauda, J.B. Molecular Dynamics Simulations of Ceramide and Ceramide-Phosphatidylcholine Bilayers. *J. Phys. Chem. B.* **2017**.
66. Klauda, J.B.; Monje, V.; Kim, T.; Im, W. Improving the CHARMM Force Field for Polyunsaturated Fatty Acid Chains. *J. Phys. Chem. B.* **2012**, *116*, 9424-9431.
67. Lim, J.B.; Klauda, J.B. Branching at the Iso- and Anteiso- Positions in Complex Chlamydia Membranes: A Molecular Dynamics Study. *Biochim. Biophys. Acta, Biomembr.* **2011**, *1808*, 323-331
68. Pandit, K.R.; Klauda, J.B. Membrane Models of *E. Coli* Containing Cyclic Moieties in the Aliphatic Lipid Chain. *Biochim. Biophys. Acta, Biomembr.* **2012**, *1818*, 1205-1210.
69. Lim, J.B.; Rogaski, B.; Klauda, J.B. Update of the Cholesterol Force Field Parameters in CHARMM. *J. Phys. Chem. B.* **2012**, *116*, 203-210.
70. Monje-Galvan, V.; Klauda, J.B. Modelling Yeast Organelle Membranes and How Lipid Diversity Influences Bilayer Properties. *Biochemistry*. **2015**, *54*, 6852-6861.
71. Zhuang, X.; Ou, A.; Klauda, J.B. Simulations of Simple Linoleic Acid-Containing Lipid Membranes and Models for the Soybean Plasma Membranes. *J. Chem. Phys.* **2017**, *146*, 215103.

72. Leonard, A.N.; Pastor, R.W.; Klauda, J.B. Parameterization of the CHARMM All-Atom Force Field for Ether Lipids and Model Linear Ethers. *J. Phys. Chem. B.* **2018**, *122*, 6744-6754.
73. Chowdhary, J.; Harder, E.; Lopes, P.E.M.; Huang, L.; MacKerell, A.D.; Roux, B. A Polarizable Force Field of Dipalmitoylphosphatidylcholine Based on the Classical Drude Model for Molecular Dynamics Simulations of Lipids. *J. Phys. Chem. B.* **2013**, *117*, 9142-9160.
74. Vorobyov, I.V.; Anisimov, V.M.; MacKerell, A.D., Jr. Polarizable Empirical Force Field for Alkanes Based on the Classical Drude Oscillator Model. *J. Phys. Chem. B.* **2005**, *109*, 18988-18999.
75. Vanommeslaeghe, K.; MacKerell, A.D., Jr. CHARMM Additive and Polarizable Force Fields for Biophysics and Computer-Aided Drug Design. *Biochim. Biophys. Acta*. **2015**, *1850*, 861-871.
76. Li, H.; Chowdhary, J.; Huang, L.; He, X.; MacKerell, A.D., Jr.; Roux, B. Drude Polarizable Force Field for Molecular Dynamics Simulations of Saturated and Unsaturated Zwitterionic Lipids. *J. Chem. Theory Comput.* **2017**, *13*, 4535-4552.
77. Lamoureux, G.; Roux, B.Ì.t. Modeling Induced Polarization with Classical Drude Oscillators: Theory and Molecular Dynamics Simulation Algorithm. *J. Chem. Phys.* **2003**, *119*, 3025-3039.
78. Miller, K.J. Additivity Methods in Molecular Polarizability. *J. Am. Chem. Soc.* **1990**, *112*, 8533-8542.
79. Anisimov, V.M.; Vorobyov, I.V.; Roux, B.; MacKerell, A.D. Polarizable Empirical Force Field for the Primary and Secondary Alcohol Series Based on the Classical Drude Model. *J. Chem. Theory Comput.* **2007**, *3*, 1927-1946.
80. Lopes, P.E.M.; Lamoureux, G.; Roux, B.; MacKerell, A.D., Jr. Polarizable Empirical Force Field for Aromatic Compounds Based on the Classical Drude Oscillator. *J. Phys. Chem. B.* **2007**, *111*, 2873-2885.
81. Vorobyov, I.; Anisimov, V.M.; Greene, S.; Venable, R.M.; Moser, A.; Pastor, R.W.; MacKerell, A.D. Additive and Classical Drude Polarizable Force Fields for Linear and Cyclic Ethers. *J. Chem. Theory Comput.* **2007**, *3*, 1120-1133.
82. Baker, C.M.; MacKerell, A.D. Polarizability Rescaling and Atom-Based Thole Scaling in the CHARMM Drude Polarizable Force Field for Ethers. *J. Mol. Model.* **2010**, *16*, 567-576.
83. Lopes, P.E.M.; Lamoureux, G.; Mackerell, A.D., Jr. Polarizable Empirical Force Field for Nitrogen-Containing Heteroaromatic Compounds Based on the Classical Drude Oscillator. *J. Comput. Chem.* **2009**, *30*, 1821-1838.
84. Lopes, P.E.M.; Huang, J.; Shim, J.; Luo, Y.; Li, H.; Roux, B.; MacKerell, A.D., Jr. Polarizable Force Field for Peptides and Proteins Based on the Classical Drude Oscillator. *J. Chem. Theory Comput.* **2013**, *9*, 5430-5449.
85. Savelyev, A.; MacKerell, A.D. All- Atom Polarizable Force Field for DNA Based on the Classical Drude Oscillator Model. *J. Comput. Chem.* **2014**, *35*, 1219-1239.
86. Thole, B.T. Molecular Polarizabilities Calculated with a Modified Dipole Interaction. *Chem. Phys.* **1981**, *59*, 341-350.
87. Harder, E.; Anisimov, V.M.; Whitfield, T.W.; MacKerell, A.D.; Roux, B. Understanding the Dielectric Properties of Liquid Amides from a Polarizable Force Field. *J. Phys. Chem. B.* **2008**, *112*, 3509-3521.
88. Lamoureux, G.; Harder, E.; Vorobyov, I.V.; Roux, B.; MacKerell, A.D. A Polarizable Model of Water for Molecular Dynamics Simulations of Biomolecules. *Chem. Phys. Lett.* **2006**, *418*, 245-249.

89. Wenbo, Y.; Pedro, E.M.L.; Benoit, R.; Alexander D. MacKerell, Jr. Six-Site Polarizable Model of Water Based on the Classical Drude Oscillator. *J. Chem. Phys.* **2013**, *138*, 034508.
90. Ollila, O.H.S.; Pabst, G. Atomistic Resolution Structure and Dynamics of Lipid Bilayers in Simulations and Experiments. *Biochim. Biophys. Acta-Biomembr.* **2016**, *1858*, 2512-2528.
91. Botan, A.; Favela-Rosales, F.; Fuchs, P.F.J.; Javanainen, M.; Kanduc, M.; Kulig, W.; Lamber, A.; Loison, C.; Lyubartsev, A.; Miettinen, M.S.; Monticelli, L.; Maatta, J.; Ollila, O.H.S.; Retegan, M.; Rog, T.; Santuz, H.; Tynkkynen, J. Toward Atomistic Resolution Structure of Phosphatidylcholine Headgroup and Glycerol Backbone at Different Ambient Conditions. *J. Phys. Chem. B.* **2015**, *119*, 15075-15088.
92. Venable, R.M.; Brown, F.L.H.; Pastor, R.W. Mechanical Properties of Lipid Bilayers from Molecular Dynamics Simulation. *Chem. Phys. Lipids*. **2015**, *192*, 60-74.
93. Sodt, A.J.; Sandar, M.L.; Gawrisch, K.; Pastor, R.W.; Lyman, E. The Molecular Structure of the Liquid-Ordered Phase of Lipid Bilayers. *J. Am. Chem. Soc.* **2014**, *136*, 725-732.
94. Wang, E.; Klauda, J.B. Examination of Mixtures Containing Sphingomyelin and Cholesterol by Molecular Dynamics Simulations. *J. Phys. Chem. B.* **2017**, *121*, 4833-4844.
95. Bera, I.; Klauda, J.B. Molecular Simulations of Mixed Lipid Bilayers with Sphingomyelin, Glycerophospholipids, and Cholesterol. *J. Phys. Chem. B.* **2017**, *121*, 5197-5208.
96. Camley, B.A.; Lerner, M.G.; Pastor, R.W.; Brown, F.L.H. Strong Influence of Periodic Boundary Conditions on Lateral Diffusion in Lipid Bilayer Membranes. *J. Chem. Phys.* **2015**, *143*, 12, 243113.
97. Venable, R.M.; Ingolfsson, H.I.; Lerner, M.G.; Perrin, B.S.; Camley, B.A.; Marrink, S.J.; Brown, F.L.H.; Pastor, R.W. Lipid and Peptide Diffusion in Bilayers: The Saffman-Delbruck Model and Periodic Boundary Conditions. *J. Phys. Chem. B.* **2017**, *121*, 3443-3457.
98. Oostenbrink, C.; Villa, A.; Mark, A.E.; Van Gunsteren, W.F. A Biomolecular Force Field Based on the Free Enthalpy of Hydration and Solvation: The GROMOS Force-Field Parameter Sets 53a5 and 53a6. *J. Comput. Chem.* **2004**, *25*, 1656-1676.
99. Madej, B.D.; Dickson, C.J.; Skjevik, A.A.; Betz, R.M.; Walker, R.C.; Teigen, K. Lipid14: The Amber Lipid Force Field. *Abstr. Pap. Am. Chem. Soc.* **2014**, *248*, 1.
100. Pastor, R.W.; MacKerell, A.D. Development of the CHARMM Force Field for Lipids. *J. Phys. Chem. Lett.* **2011**, *2*, 1526-1532.
101. Klauda, J.B.; Wu, X.W.; Pastor, R.W.; Brooks, B.R. Long-Range Lennard-Jones and Electrostatic Interactions in Interfaces: Application of the Isotropic Periodic Sum Method. *J. Phys. Chem. B.* **2007**, *111*, 4393-4400.
102. Allen, M.P.; Tildesley, D.J. *Computer Simulations of Liquids*. Clarendon Press: Oxford, England. 1987.
103. Lagüe, P.; Pastor, R.W.; Brooks, B.R. Pressure-Based Long-Range Correction for Lennard-Jones Interactions in Molecular Dynamics Simulations: Application to Alkanes and Interfaces. *J. Phys. Chem. B.* **2004**, *108*, 363-368.
104. Wennberg, C.L.; Murtola, T.; Pall, S.; Abraham, M.J.; Hess, B.; Lindahl, E. Direct-Space Corrections Enable Fast and Accurate Lorentz-Berthelot Combination Rule Lennard-Jones Lattice Summation. *J. Chem. Theory Comput.* **2015**, *11*, 5737-5746.
105. Hoover, W.G. Canonical Dynamics: Equilibrium Phase-Space Distributions. *Phys. Rev. A.* **1985**, *31*, 1695.
106. Nose, S.; Klein, M.L. Constant Pressure Molecular Dynammics for Molecular Systems. *J. Chem. Phys.* **1983**, *78*, 6928.

107. Anderson, H.C. Quantum Chemistry by Random Walk: Higher Accuracy. *J. Chem. Phys.* **1980**, *72*, 2384.
108. Ryckaert, J.P.; Ciccotti, G.; Berendsen, H.J.C. Numerical Integration of the Cartesian Equations of Motion of a System with Constrations: Molecular Dynamics of *N*-Alkanes. *J. Comput. Phys*. **1977**, *23*, 327.
109. Essmann, U.; Perera, L.; Berkowitz, M.L.; Darden, T.; Lee, H.; Pedersen, L.G. A Smooth Particle Mesh Ewald Method. *J. Chem. Phys.* **1995**, *103*, 8577-8593.
110. Zhang, Y.H.; Feller, S.E.; Brooks, B.R.; Pastor, R.W. Computer-Simulation of Liquid/Liquid Interfaces .1. Theory and Application to Octane/Water. *J. Chem. Phys.* **1995**, *103*, 10252-10266.
111. Yeh, I.C.; Hummer, G. System-Size Dependence of Diffusion Coefficients and Viscosities from Molecular Dynamics Simulations with Periodic Boundary Conditions. *J. Phys. Chem. B*. **2004**, *108*, 15873-15879.
112. Lipari, G.; Szabo, A. Effect of Librational Motion on Flourescence Depolarization and Nuclear Magnetic-Resonance Relaxation in Macromolecules and Membranes. *Biophys. J.* **1980**, *30*, 489-506.
113. Ottiger, M.; Bax, A. Determination of Relative N-H-N N-C ', C-Alpha-C ', Andc(Alpha)-H-Alpha Effective Bond Lengths in a Protein by NMR in a Dilute Liquid Crystalline Phase. *J. Am. Chem. Soc.* **1998**, *120*, 12334-12341.
114. Wu, X.W.; Brooks, B.R. Isotropic Periodic Sum: A Method for the Calculation of Long-Range Interactions. *J. Chem. Phys.* **2005**, *122*, 044107.
115. Wu, X.W.; Brooks, B.R. Using the Isotropic Periodic Sum Method to Calculate Long-Range Interactions of Heterogeneous Systems. *J. Chem. Phys.* **2008**, *129*, 154115.
116. Venable, R.M.; Chen, L.E.; Pastor, R.W. Comparison of the Extended Isotropic Periodic Sum and Particle Mesh Ewald Methods for Simulations of Lipid Bilayers and Monolayers. *J. Phys. Chem. B*. **2009**, *113*, 5855-5862.
117. Mecke, M.; Winkelmann, J.; Fischer, J. Molecular Dynamics Simulation of the Liquid-Vapor Interface: The Lennard-Jones Fluid. *J. Chem. Phys.* **1997**, *107*, 9264 - 9270.
118. Janecek, J. Long Range Corrections in Inhomogeneous Simulations. *J. Phys. Chem. B.* **2006**, *110*, 6264 - 6269.
119. MacDowell, L.G.; Blas, F.J. Surface Tension of Fully Flexible Lennard-Jones Chains: Role of Long-Range Corrections. *J. Chem. Phys*. **2009**, *131*, 074705.
120. Feller, S.E.; Pastor, R.W.; Rojnuckarin, A.; Bogusz, S.; Brooks, B.R. Effect of Electrostatic Force Truncation on Interfacial and Transport Properties of Water. *J. Phys. Chem*. **1996**, *100*, 17011-17020.
121. Nijboer, B.R.A.; Dewette, F.W. On the Calculation of Lattice Sums. *Physica*. **1957**, *23*, 309-321.
122. Williams, D.E. Accelerated Convergence of Crystal-Lattice Potential Sums. *Acta Crystall. A-Crys.*. **1971**, *A 27*, 452-&.
123. Karasawa, N.; Goddard, W.A. Acceleration of Convergence for Lattice Sums. *J. Phys. Chem*. **1989**, *93*, 7320-7327.
124. Veld, P.J.I.; Ismail, A.E.; Grest, G.S. Comp 6-Application of Ewald Summations to Long-Range Dispersion Forces. *Abstr. Pap. Am. Chem. Soc.* **2007**, *234*.
125. Isele-Holder, R.E.; Mitchell, W.; Ismail, A.E. Development and Application of a Particle-Particle Particle-Mesh Ewald Method for Dispersion Interactions. *J. Chem. Phys.* **2012**, *137*, 174107.
126. Isele-Holder, R.E.; Mitchell, W.; Hammond, J.R.; Kohlmeyer, A.; Ismail, A.E. Reconsidering Dispersion Potentials: Reduced Cutoffs in Mesh-Based Ewald Solvers Can Be Faster Than Truncation. *J. Chem. Theory Comput*. **2013**, *9*, 5412-5420.

127. Wennberg, C.L.; Murtola, T.; Hess, B.; Lindahl, E. Lennard-Jones Lattice Summation in Bilayer Simulations Has Critical Effects on Surface Tension and Lipid Properties. *J. Chem. Theory Comput*. **2013**, *9*, 3527-3537.
128. Steinbach, P.J.; Brooks, B.R. New Spherical-Cutoff Methods for Long-Range Forces in Macromolecular Simulation. *J. Comput. Chem.* **1994**, *15*, 667 - 683.
129. Small, D.M. *Handbook of Lipid Research 4: The Physical Chemistry of Lipids*. Plenum Press: New York. 1986.
130. Dymond, J.H.; Harris, K.R. The Temperature and Density Dependence of the Self-Diffusion Coefficeint of Normal-Hexadecane. *Mol. Phys*. **1992**, *75*, 461-466.
131. Zhang, Y.H.; Venable, R.M.; Pastor, R.W. Molecular Dynamics Simulations of Neat Alkanes: The Viscosity Dependence of Rotational Relaxation. *J. Chem. Phys.* **1996**, *100*, 2652 - 2660.
132. Berne, B.J.; Pecora, R. *Dynamic Light Scattering with Applications to Chemistry, Biology, and Physics* Vol. New York City, New York. John Wiley & Sons, Inc. 1976.
133. Khasanshin, T.; Samuilov, V.; Shchemelev, A. Determination of the Thermodynamic Properties of Liquid N-Hexadecane from the Measurements of the Velocity of Sound. *J. Engineering Phys. Thermmophys*. **2009**, *82*, 149 - 156.
134. Fischer, N.M.; van Maaren, P.J.; Ditz, J.C.; Yildirim, A.; van der Spoel, D. Properties of Organic Liquids When Simulated with Long-Range Lennard-Jones Interactions. *J. Chem. Theory Comput*. **2015**, *11*, 2938.
135. Vanommeslaeghe, K.; Hatcher, E.; Acharya, C.; Kundu, S.; Zhong, S.; Shim, J.; Darian, E.; Guvench, O.; Lopes, P.; Vorobyov, I.; A. D. Mackerell, J. CHARMM General Force Field: A Force Field for Drug-Like Molecules Compatible with the CHARMM All-Atom Additive Biological Force Fields. *J. Comput. Chem.* **2010**, *31*, 671–690.
136. Zhuang, X.; Makover, J.R.; Im, W.; Klauda, J.B. A Systematic Molecular Dynamics Simulation Study of Temperature Dependent Bilayer Structural Properties. *Biochim. Biophys. Acta-Biomembr.* **2014**, *1838*, 2520 - 2529.
137. Swendsen, R.H.; Wang, J.S. Replica Monte-Carlo Simulation of Spin-Glasses. *Phys. Rev. Lett*. **1986**, *57*, 2607-2609.
138. Ren, P.; Ponder, J.W. Temperature and Pressure Dependence of the Amoeba Water Model. *J. Phys. Chem. B.* **2004**, *108*.
139. Jiang, H.; Mester, Z.; Moultos, A.A.; Economou, I.G. Thermodynamic and Transport Properties of H2o + NaCl from Polarizable Force Fields. *J. Chem. Theory Comput*. **2015**, *11*, 3802 - 3810.
140. Huang, J.; MacKerell, A.D., Jr. Induction of Peptide Bond Dipoles Drives Cooperative Helix Formation in the (Aaqaa)3 Peptide. *Biophys. J.* **2014**, *107*, 991 - 997.
141. Kiss, P.T.; Baranyai, A. A Systematic Development of a Polarizable Potential of Water. *J. Chem. Phys.* **2013**, *138*, 204507 - 204517.
142. Kiss, P.T.; Baranyai, A. A New Polarizable Force Field for Alkali and Halide Ions. *J. Chem. Phys.* **2014**, *141*, 114501 - 114515.
143. Berendsen, H.J.C.; Grigera, J.R.; Straatsma, T.P. The Missing Term in Effective Pair Potentials. *J. Phys. Chem*. **1987**, *91*, 6269 - 6271.
144. Smith, D.E.; Dang, L.X. Computer-Simulations of NaCl Association in Polarizable Water. *J. Chem. Phys.* **1994**, *100*, 3757 - 3766.
145. Ingham, K.C. Protein Precipitation with Polyethylene Glycol *Methods in Enzymology*. **1984**, *104*, 351 - 356.
146. Raymond, P. Mallory-Weiss Tear Associated with Polyethylnene Glycol Electrolyte Lavange Solution. . *Gastrointest Endosc.* **1991**, *37*, 410 - 411.
147. Jang, H.J.; Shin, C.Y.; Kim, K.B. Safety Evaluation of Polyethylene Glycol (Peg) Compounds for Cosmetic Use. *Toxicol. Res*. **2015**, *31*, 105 - 136.

148. Williams, J.H.; Kuchmak, M.; Witter, R.F. Fatty Acids in Phospholipids Isolated from Human Red Cells. *Lipids*. **1966**, *1*, 391-&.
149. van de Vossenberg, J.; Driessen, A.J.M.; Konings, W.N. The Essence of Being Extremophilic: The Role of the Unique Archaeal Membrane Lipids. *Extremophiles*. **1998**, *2*, 163-170.
150. Guler, D.S.; Ghosh, D.D.; Pan, J.; Mathai, J.C.; Zeidel, M.L.; Nagle, J.F.; Tristram-Nagle, S. Effects of Ether Vs. Ester Linkage on Lipid Bilayer Structure and Water Permeability. *Chem. Phys. Lipids*. **2009**, *160*, 33 - 44.
151. Gawrisch, K.; Ruston, D.; Zimmerberg, J.; Parsegian, V.A.; Rand, R.P.; Fuller, N. Membrane Dipole Potentials, Hydration Forces, and the Ordering of Water at Membrane Surfaces. *Biophys. J.* **1992**, *61*, 1213 - 1223.
152. Oelmeier, S.A.; Dismer, F.; Hubbuch, J. Molecular Dynamics Simulations on Aqueous Two-Phase Systems - Single Peg-Molecules in Solution. *BMC Biophys*. **2012**, *5*, 14.
153. Xiang, Y.; Xu, R.G.; Leng, Y.S. Molecular Dynamics Simulations of a Poly(Ethylene Glycol)-Grafted Polyamide Membrane and Its Interaction with a Calcium Alginate Gel. *Langmuir*. **2016**, *32*, 4424-4433.
154. Kruczek, J.; Saunders, M.; Khosla, M.; Tu, Y.; Pandit, S.A. Molecular Dynamics Simulations of Ether- and Ester-Linked Phospholipids. *BBA - Biomemb*. **2017**, *1859*, 2297 - 2307.
155. Pan, J.; Cheng, X.; Heberle, F.A.; Mostofian, B.; Kucerka, N.; Drazba, P.; Katsaras, J. Interactions between Ether Phospholipids and Cholesterol as Determined by Scattering and Molecular Dynamics Simulations. *J. Phys. Chem. B*. **2012**, *116*, 14829 - 14838.
156. Shinoda, K.; Shinoda, W.; Baba, T.; Mikami, M. Comparative Molecular Dynamics Study of Ether- and Ester-Linked Phospholipid Bilayers. *J. Chem. Phys*. **2004**, *121*, 9648-9654.
157. Lee, H.; Venable, R.M.; MacKerell, A.D., Jr.; Pastor, R.W. Molecular Dynamics Studies of Polyethylene Oxide and Polyethylene Glycol: Hydrodynamic Radius and Shape Anisotropy. *Biophys. J.* **2008**, *95*, 1590 - 1599.
158. Han, X.; Holtzman, D.M.; McKeel, D.W. Plasmalogen Deficiency in Early Alzheimer's Disease Subjects and in Animal Models: Molecular Characterization Using Electrospray Ionization Mass Spectrometry. *J. Neurochem*. **2001**, *77*, 1168-1180.
159. Saab, S.; Mazzocco, J.; Creuzot-Garcher, C.P.; Bron, A.M.; Bretillon, L.; Acar, N. Plasmalogens in the Retina: From Occurrence in Retinal Cell Membranes to Potential Involvement in Pathophysiology of Retinal Diseases. *Biochimie*. **2014**, *107 Pt A*, 58-65.
160. Guan, Z.; Wang, Y.; Cairns, N.J.; Lantos, P.L.; Dallner, G.; Sindelar, P.J. Decrease and Structural Modifications of Phosphatidylethanolamine Plasmalogen in the Brain with Alzheimer Disease. *J. Neuropath. Exp. Neur*. **1999**, *58*, 740-747.
161. Han, X. Lipid Alterations in the Earliest Clinically Recognizable Stage of Alzheimer's Disease: Implication of the Role of Lipids in the Pathogenesis of Alzheimer's Disease. *Curr. Alzheimer Res*. **2005**, *2*, 65-77.
162. Hofteig, J.H.; Noronha, A.B.; Druse, M.J.; Keresztes-Nagy, C. Synaptic Membrane Phospholipids: Effects of Maternal Ethanol Consumption. *Exp. Neurol*. **1985**, *87*, 165-171.
163. Takamori, S.; Holt, M.; Stenius, K.; Lemke, E.A.; Grønborg, M.; Riedel, D.; Urlaub, H.; Schenck, S.; Brügger, B.; Ringler, P.; Müller, S.A.; Rammner, B.; Gräter, F.; Hub, J.S.; De Groot, B.L.; Mieskes, G.; Moriyama, Y.; Klingauf, J.; Grubmüller, H.; Heuser, J.; Wieland, F.; Jahn, R. Molecular Anatomy of a Trafficking Organelle. *Cell*. **2006**, *127*, 831-846.
164. Davletov, B.; Montecucco, C. Lipid Function at Synapses. *Curr. Opin. Neurobiol*. **2010**, *20*, 543-549.

165. Nagan, N.; Zoeller, R.A. Plasmalogens: Biosynthesis and Functions. *Prog. Lipid Res*. **2001**, *40*, 199-229.
166. Pike, L.J.; Han, X.; Chung, K.N.; Gross, R.W. Lipid Rafts Are Enriched in Arachidonic Acid and Plasmenylethanolamine and Their Composition Is Independent of Caveolin-1 Expression: A Quantitative Electrospray Ionization/Mass Spectrometric Analysis. *Biochem*. **2002**, *41*, 2075-2088.
167. Sebastião, A.M.; Colino-Oliveira, M.; Assaife-Lopes, N.; Dias, R.B.; Ribeiro, J.A. Lipid Rafts, Synaptic Transmission and Plasticity: Impact in Age-Related Neurodegenerative Diseases. *Neuropharmacol*. **2013**, *64*, 97-107.
168. Valiev, M.; Bylaska, E.J.; Govind, N.; Kowalski, K.; Straatsma, T.P.; Van Dam, H.J.J.; Wang, D.; Niepolcha, J.; Arpa, E.; Windus, T.L.; de Jong, W.A. Nwchem: A Comprehensive and Scalable Open-Source Solution for Large Scale Molecular Simulations. . *Comput. Phys. Commun*. **2010**, *181*, 1477 - 1493.
169. Brenerman, C.M.; Wilberg, K.B. Determining Atom-Centered Monopoles from Molecular Electrostatic Potentials. The Need for High Sampling Density in Formamide Conformational Analysis. *J. Comput. Chem*. **1990**, *11*, 361 - 370.
170. Klauda, J.B.; Garrison, S.L.; Jiang, J.; Arora, G.; Sandler, S.I. HM-IE: Quantum Chemical Hybrid Methods for Calculating Interaction Energies. *J. Phys. Chem. A*. **2004**, *108*, 107 - 112.
171. Brooks, B.R.; Brooks, C.L.; MacKerell, A.D., Jr.; Nilsson, R.; Petrella, J.; Roux, B.; Won, Y.; Archontis, G.; Bartels, C.; Boresch, S.; Caflisch, A.; Caves, L.; Cui, Q.; Dinner, A.R.; Feig, M.; Fischer, S.; Gao, J.; Hodoscek, M.; Im, W.; Kucerka, N.; Lazaridis, T.; Ma, J.; Ovchinnikov, V.; Paci, E.; Pastor, R.W.; Post, C.B.; Pu, J.Z.; Schaefer, M.; Tidor, B.; Venable, R.M.; Woodcock, H.L.; Wu, X.; Yang, W.; York, D.M.; Karplus, M. CHARMM: The Biolmolecular Simulation Program. *J. Comput. Chem.*. **2009**, *30*, 1545 - 1615.
172. Guvench, O.; MacKerell, A.D., Jr. Automated Conformational Energy Fitting for Force-Field Development. *J. Mol. Model*. **2008**, *14*, 667 - 679.
173. Leonard, A.N.; Simmonett, A.C.; Pickard, F.C.t.; Huang, J.; Venable, R.M.; Klauda, J.B.; Brooks, B.R.; Pastor, R.W. Comparison of Additive and Polarizable Models with Explicit Treatment of Long-Range Lennard-Jones Interactions Using Alkane Simulations. *J. Chem. Theory Comput.* **2018**, *14*, 948-958.
174. Deng, Y.; Roux, B. Hydration of Amino Acid Side Chains: Nonpolar and Electrostatic Contributions Calculated from Staged Molecular Dynamics Free Energy Simulations with Explicit Water Molecules. *J. Phys. Chem. B*. **2004**, *108*, 16567 - 16576.
175. Ferrenberg, A.M.; Swendsen, R.H. New Monte Carlo Technique for Studying Phase Transitions. *Phys. Rev. Lett.* **1988**, *61*, 2635-2638.
176. Ferrenberg, A.M.; Swendsen, R.H. Optimized Monte Carlo Data Analysis. *Phys. Rev. Lett.* **1989**, *63*, 1195-1198.
177. Kumar, S.; Rosenberg, J.M.; Bouzida, D.; Swendsen, R.H.; Kollman, P.A. The Weighted Histogram Analysis Method for Free-Energy Calculations on Biomolecules. I. The Method. *J. Comput. Chem.* **1992**, *13*, 1011-1021.
178. Van Gunsteren, W.F. A Molecular Dynamics Simulation Study of Chloroform. *Mol. Phys*. **1994**, *83*, 381-403.
179. Leonard, A.N.; Simmonett, A.C.; Pickard, F.C., IV; Huang, J.; Venable, R.M.; Klauda, J.B.; Brooks, B.R.; Pastor, R.W. Comparison of Additive and Polarizable Models with Explicit Treatment of Long-Range Lennard-Jones Interactions Using Alkane Simulations. *J. Chem. Theory Comput*. **2017**.
180. Wennberg, C.L.; Murtola, T.; Pall, S.; Abraham, M.J.; Hess, B.; Lindahl, E. Direct-Space Corrections Enable Fast and Accurate Lorentz-Berthelot Combination Rule Lennard-Jones Lattice Summation. *J. Chem. Theory Comput.* **2015**, *11*, 5737 - 5746.

181. Jo, S.; Kim, T.; Iyer, V.G.; Im, W. CHARMM-GUI: A Web-Based Graphical User Interface for CHARMM. *J. Comput. Chem*. **2008**, *29*, 1859 - 1865.
182. Jo, S.; Lim, J.B.; Klauda, J.B.; Im, W. CHARMM-GUI Membrane Builder for Mixed Bilayers and Its Application to Yeast Membranes. *Biophys. J*. **2009**, *97*, 50 - 58.
183. Wu, E.L.; Cheng, X.; Jo, S.; Rui, H.; Song, K.C.; Lee, J.; Davila-Contreras, E.M.; Beaven, A.H.; Monje-Galvan, V.; Venable, R.M.; Klauda, J.B.; Im, W. CHARMM-GUI Membrane Builder toward Realistic Biological Membrane Simulations. *J. Comput. Chem.* **2014**, *35*, 1997-2004.
184. Lee, J.; Cheng, X.; Swails, J.M.; Yeom, M.S.; Eastman, P.K.; Lemkul, J.A.; Wei, S.; Buckner, J.; Jeong, J.C.; Qi, Y.; Jo, S.; Pande, V.S.; Case, D.A.; Brooks, C.L.; MacKerell, A.D.; Klauda, J.B.; Im, W. CHARMM-GUI Input Generator for NAMD, GROMACS, AMBER, Openmm, and CHARMM/Openmm Simulations Using the CHARMM36 Additive Force Field. *J. Chem. Theory Comput.* **2016**, *12*, 405-413.
185. Phillips, J.C.; Braun, R.; Wang, W.; Gumbart, J.; Tajkhorshid, E.; Villa, E.; Chipot, C.; Skeel, R.D.; Kale, L.; Schulten, K. Scalable Molecular Dynamics with NAMD. *J. Comput. Chem.* **2005**, *26*, 1781-1802.
186. Feller, S.E.; Zhang, Y.H.; Pastor, R.W.; Brooks, B.R. Constant-Pressure Molecular-Dynamics Simulation - the Langevin Piston Method. *J. Chem. Phys.* **1995**, *103*, 4613-4621.
187. Martyna, G.J.; Tobias, D.J.; Klein, M.L. Constant Pressure Molecular Dynamics Algorithms. *J. Chem. Phys.* **1994**, *101*, 4177-4189.
188. Venable, R.M.; Luo, Y.; Gawrisch, K.; Roux, B.; Pastor, R.W. Simulations of Anionic Lipid Membranes: Development of Interaction-Specific Ion Parameters and Validation Using NMR Data. *J. Phys. Chem. B*. **2013**, *117*, 10183-10192.
189. Kucerka, N.; Katsaras, J.; Nagle, J.F. Comparing Membrane Simulations to Scattering Experiments: Introducing the Simtoexp Software. *J. Membrane Biol*. **2010**, *235*, 43 - 50.
190. *Matlab and Statistics Toolbox Release 2016a*. 2016, The MathWorks, Inc.: Natick, Massachusetts, United States.
191. Feller, S.E.; Pastor, R.W. Constant Surface Tension Simulations of Lipid Bilayers: The Sensitivity of Surface Areas and Compressiblities. *J. Chem. Phys*. **1999**, *111*, 1281 - 1287.
192. Humphrey, W., Dalke, A., and Schulten, K. VMD - Visual Molecular Dynamics. *J. Mol. Graphics*. **1996**, *14*, 33 - 38.
193. Lide, D.R.; Milne, G.W.A., eds. *Handbook of Data on Organic Compounds*, 3 ed. Vol. I. 1994, CRC Press, Inc.: Boca Raton, FL.
194. O'Neil, M.J., ed. *The Merck Index - an Encyclopedia of Chemicals, Drugs, and Biologicals*, 13 ed. 2001, Merck and Co., Inc.: Whitehouse Station, NJ, 1723.
195. Cabani, S.; Gianni, P.; Mollica, V.; Lepori, L. Thermodynamic Study of Aqueous Dilute Solutions of Organic Compounds; Part 5.: Open-Chain Saturated Bifunctional Compounds. *T. Faraday Soc*. **1978**, *67*, 1933 - 1942.
196. Sprott, G.D., *Archaeal Membrane Lipids and Applications*, in *Encyclopedia of Life Sciences*. 2011, John Wiley & Sons, Ltd.: Ottawa, ON, Canada.
197. Lim, J.B.; Klauda, J.B. Lipid Chain Branching at the Iso- and Anteiso-Positions in Complex Chlamydia Membranes: A Molecular Dynamics Study. *BBA-Biomembranes*. **2011**, *1808*, 323-331.
198. Rawicz, W.; Olbrich, K.C.; McIntosh, T.; Needham, D.; Evans, E. Effect of Chain Length and Saturation on Elasticity of Lipid Bilayers. *Biophys. J*. **2000**, *79*, 328 - 3239.
199. Nagle, J.F.; Tristram-Nagle, S. Structure of Lipid Bilayers.*BBA-Rev. Biomembranes*. **2000**, *1469*, 159 - 195.
200. Clarke, R.J. The Dipole Potential of Phospholipid Membranes and Methods for Its Detection. *Adv. Colloid Interfac*. **2001**, *89*, 263-281.

201. Wang, L.; Bose, P.S.; Sigworth, F.J. Using Cryo-Em to Measure the Dipole Potential of a Lipid Membrane. *PNAS*. **2006**, *103*, 18528 - 18533.
202. Peterson, U.; Mannock, D.A.; Lewis, R.; Phol, P.; McElhaney, R.N.; Pohl, E.E. Origin of Membrane Dipole Potential: Contribution of the Phospholipid Fatty Acid Chains. *Chem. Phys. Lipids*. **2002**, *117*, 19 - 27.
203. Friedman, R. Membrane-Ion Interactions. *J. Membr. Biol.* **2018**, *251*, 453-460.
204. Leonard, A.N.; Klauda, J.B.; Sukharev, S. Isothermal Titration Calorimetry of Be2+ with Phosphatidylserine Models Guides All-Atom Force-Field Development for Lipid-Ion Interactions. *J. Phys. Chem. B*. **2019**, *123*, 1554-1565.
205. Nelsestuen, G.L.; Broderius, M.; Martin, G. Role of Gamma-Carboxyglutamic Acid. Cation Specificity of Prothrombin and Factor X-Phospholipid Binding. *J. Biol. Chem.* **1976**, *251*, 6886-6893
206. Brasch, J.; Harrison, O.J.; Honig, B.; Shapiro, L. Thinking Outside the Cell: How Cadherins Drive Adhesion. *Trends Cell. Biol.* **2012**, *22*, 299-310.
207. Willems, B.A.; Vermeer, C.; Reutelingsperger, C.P.; Schurgers, L.J. The Realm of Vitamin K Dependent Proteins: Shifting from Coagulation toward Calcification. *Mol. Nutr. Food Res.* **2014**, *58*, 1620-1635.
208. Lemmon, M.A. Membrane Recognition by Phospholipid-Binding Domains. *Nat. Rev. Mol. Cell Bio.* **2008**, *9*, 99-111.
209. Bill, J.R.; Mack, D.G.; Falta, M.T.; Maier, L.A.; Sullivan, A.K.; Joslin, F.G.; Martin, A.K.; Freed, B.M.; Kotzin, B.L.; Fontenot, A.P. Beryllium Presentation to Cd4+ T Cells Is Dependent on a Single Amino Acid Residue of the Mhc Class Ii Beta-Chain. *J. Immunol. (Baltimore)*. **2005**, *175*, 7029-7037.
210. Martin, A.K.; Mack, D.G.; Falta, M.T.; Mroz, M.M.; Newman, L.S.; Maier, L.A.; Fontenot, A.P. Beryllium-Specific Cd4+ T Cells in Blood as a Biomarker of Disease Progression. *J. Allergy Clin. Immun.* **2011**, *128*, 1100-1106.
211. Alei, M.J.; Jackson, J.A. NMR Determination of the Hydration Number of Cations in Aqueous Percholate Solution. *J. Chem. Phys.* **1964**, *41*.
212. Luo, Y.; Roux, B.t. Simulation of Osmotic Pressure in Concentrated Aqueous Salt Solutions. *J. Phys. Chem. Lett.* **2010**, *1*, 183-189.
213. Venable, R.M.; Luo, Y.; Gawrisch, K.; Roux, B.; Pastor, R.W. Simulations of Anionic Lipid Membranes: Development of Interaction-Specific Ion Parameters and Validation Using NMR Data. *J. Phys. Chem. B.* **2013**, *117*, 10183-10192.
214. Han, K.; Venable, R.M.; Bryant, A.M.; Legacy, C.J.; Shen, R.; Li, H.; Roux, B.; Gericke, A.; Pastor, R.W. Graph-Theoretic Analysis of Monomethyl Phosphate Clustering in Ionic Solutions. *J. Phys. Chem. B*. **2018**, *122*, 1484-1494.
215. Høiland, H.; Ringseth, J.A.; Brun, T.S. Cation-Crown Ether Complex Formation in Water. Ii. Alkali and Alkaline Earth Cations and 12-Crown-4, 15-Crown-5, and 18-Crown-6. *J. Solution Chem.* **1979**, *8*, 779-792.
216. Chen, P.C.; Hub, J.S. Validating Solution Ensembles from Molecular Dynamics Simulation by Wide-Angle X-Ray Scattering Data. *Biophys. J.* **2014**, *107*, 435-447.
217. Knight, C.J.; Hub, J.S. Waxsis: A Web Server for the Calculation of Saxs/Waxs Curves Based on Explicit-Solvent Molecular Dynamics. *Nucleic Acids Res.* **2015**, *43*, W225-W230.
218. *Itc Data Analysis in Origin. Tutorial Guide, Version 7.0* in *MicroCal, LLC*. 2004: Northampton, MA, 1 - 117.
219. Yamaguchi, T.; Ohtaki, H.; Spohr, E.; Palinkas, G.; Heinzinger, K.; Probst, M.M. Molecular Dynamics and X-Ray Diffraction Study of Aqueous Beryllium(Ii) Chloride Solutions. *Z. Naturforsch.* **1986**, *41a*, 1175 - 1185.
220. Jo, S.; Kim, T.; Im, W. Automated Builder and Database of Protein/Membrane Complexes for Molecular Dynamics Simulations. *PloS one*. **2007**, *2*, e880.

221. Jo, S.; Kim, T.; Iyer, V.G.; Im, W. CHARMM-GUI: A Web-Based Graphical User Interface for CHARMM. *J. Comput. Chem.* **2008**, *29*, 1859-1865.
222. Lee, J.; Cheng, X.; Swails, J.M.; Yeom, M.S.; Eastman, P.K.; Lemkul, J.A.; Wei, S.; Buckner, J.; Jeong, J.C.; Qi, Y.; Jo, S.; Pande, V.S.; Case, D.A.; Brooks, C.L., 3rd; MacKerell, A.D., Jr.; Klauda, J.B.; Im, W. CHARMM-GUI Input Generator for NAMD, GROMACS, AMBER, Openmm, and CHARMM/Openmm Simulations Using the CHARMM36 Additive Force Field. *J. Chem. Theory Comput.* **2016**, *12*, 405-413.
223. Humphrey, W.; Dalke, A.; Schulten, K. VMD - Visual Molecular Dynamics. *J. Mol. Graphics*. **1996**, *14*, 33 - 38.
224. Lamoureux, G.; Roux, B. Absolute Hydration Free Energy Scale for Alkali and Halide Ions Established from Simulations with a Polarizable Force Field. *J. Phys. Chem. B.* **2006**, *110*, 3308-3322.
225. Harder, E.; Roux, B. On the Origin of the Electrostatic Potential Difference at a Liquid-Vacuum Interface. *J. Chem. Phys.* **2008**, *129*, 234706.
226. Yu, H.; Whitfield, T.W.; Harder, E.; Lamoureux, G.; Vorobyov, I.; Anisimov, V.M.; Mackerell, A.D., Jr.; Roux, B. Simulating Monovalent and Divalent Ions in Aqueous Solution Using a Drude Polarizable Force Field. *J. Chem. Theory Comput.* **2010**, *6*, 774-786.
227. Marcus, Y. Thermodynamics of Solvation of Ions. *J. Chem. Soc. Faraday T.* **1991**, *87*, 2995 - 2999.
228. Yang, Z.Z.; Li, X. Molecular-Dynamics Simulations of Alkaline-Earth Metal Cations in Water by Atom-Bond Electronegativity Equalization Method Fused into Molecular Mechanics. *J. Chem. Phys.* **2005**, *123*, 94507.
229. Mobley, D.L.; Chodera, J.D.; Dill, K.A. On the Use of Orientational Restraints and Symmetry Corrections in Alchemical Free Energy Calculations. *J. Chem. Phys.* **2006**, *125*, 084902.
230. Smiechowski, M. Theoretical Pk_a Prediction of O-Phosphoserine in Aqueous Solution. *Chem. Phys. Lett.* **2010**, *501*, 123 - 129.
231. Klauda, J.B.; Wu, X.; Pastor, R.W.; Brooks, B.R. Long-Range Lennard-Jones and Electrostatic Interactions in Interfaces: Application of the Isotropic Periodic Sum Method. *J. Phys. Chem. B.* **2007**, *111*, 4393-4400.
232. Small, D.M. *The Physical Chemistry of Lipids : From Alkanes to Phospholipids*. Handbook of Lipid Research ; V. 4. Plenum Press: New York. 1986.
233. Weast, R.C., ed. *Crc Handbook of Chemistry and Physics, 62nd Edition*, 61st ed. ed. 1981, CRC Press: Boca Raton, Fla.
234. Hammouda, B., *Chapter 22: Standard Plots*, in *The Sans Toolbox*. NIST Center for Neutron Research: https://www.ncnr.nist.gov/staff/hammouda/.
235. Sears, V.F. Neutron Scattering Lengths and Cross Sections. *Neutron News*. **1992**, *3*, 26-37.
236. Frisch, M.J.; Trucks, G.W.; Schlegel, H.B.; Scuseria, G.E.; Robb, M.A.; Cheeseman, J.R.; Scalmani, G.; Barone, V.; Petersson, G.A.; Nakatsuji, H.; Li, X.; Caricato, M.; Marenich, A.; Bloino, J.; Janesko, B.G.; Gomperts, R.; Mennucci, B.; Hratchian, H.P.; Ortiz, J.V.; Izmaylov, A.F.; Sonnenberg, J.L.; Williams-Young, D.; Ding, F.; Lipparini, F.; Egidi, J.G., F.; Peng, B.; Petrone, A.; Henderson, T.; Ranasinghe, D.; Zakrzewski, V.G.; Gao, J.; Rega, N.; Zheng, G.; Liang, W.; Hada, M.; Ehara, M.; Toyota, K.; Fukuda, R.; J., H.; Ishida, M.; Nakajima, T.; Honda, V.; Kitao, O.; Nakai, H.; Vreven, T.; Throssell, K.; Montgomery, J.A., Jr.; Peralta, J.E.; Ogliaro, F.; Bearpark, M.; Heyd, J.J.; Brothers, E.; Kudin, K.N.; Staroverov, V.N.; Keith, T.; Kobayashi, R.; Normand, J.; Raghavachari, K.; Rendell, A.; Burant, J.C.; Iyengar, S.S.; Tomasi, J.; Cossi, M.; Millam, J.M.; Klene, M.; Adamo, C.; Cammi, R.; Ochterski, J.W.; Martin, R.L.; Morokuma, K.;

Farkas, O.; Foresman, J.B.; Fox, D.J., *Gaussian 09, Revision A.02*. 2016, Gaussian, Inc.: Wallingford, CT.
237. Weigend, F.; Furche, F.; Ahlrichs, R. Gaussian Basis Sets of Quadruple Zeta Valence Quality for Atoms H–Kr. *J. Chem. Phys.* **2003**, *119*, 12753-12762.
238. Weigend, F.; Ahlrichs, R. Balanced Basis Sets of Split Valence, Triple Zeta Valence and Quadruple Zeta Valence Quality for H to Rn: Design and Assessment of Accuracy. *Phys. Chem. Chem. Phys.* **2005**, *7*, 3297-3305.
239. Marenich, A.V.; Cramer, C.J.; Truhlar, D.G. Universal Solvation Model Based on Solute Electron Density and on a Continuum Model of the Solvent Defined by the Bulk Dielectric Constant and Atomic Surface Tensions. *J. Phys. Chem. B.* **2009**, *113*, 6378-6396.
240. Whitfield, T.W.; Varma, S.; Harder, E.; Lamoureux, G.; Rempe, S.B.; Roux, B. A Theoretical Study of Aqueous Solvation of K Comparing ab Initio, Polarizable, and Fixed-Charge Models. *J. Chem. Theory Comput.* **2007**, *3*, 2068-2082.
241. Scott, B.L.; McCleskey, T.M.; Chaudhary, A.; Hong-Geller, E.; Gnanakaran, S. The Bioinorganic Chemistry and Associated Immunology of Chronic Beryllium Disease. *Chem. Commun.* **2008**, *2008*, 2837-2847.
242. Beglov, D.; Roux, B.t. Finite Representation of an Infinite Bulk System: Solvent Boundary Potential for Computer Simulations. *J. Chem. Phys.* **1994**, *100*, 9050-9063.
243. Noskov, S.Y.; Roux, B. Control of Ion Selectivity in Leut: Two Na+ Binding Sites with Two Different Mechanisms. *J. Mol. Biol.* **2008**, *377*, 804-818.
244. Marchand, S.; Roux, B.t. Molecular Dynamics Study of Calbindin D9k in the Apo and Singly and Doubly Calcium-Loaded States. *Proteins: Structure, Function, and Genetics*. **1998**, *33*, 265-284.
245. Petrache, H.I.; Tristram-Nagle, S.; Gawrisch, K.; Harries, D.; Parsegian, V.A.; Nagle, J.F. Structure and Fluctuations of Charged Phosphatidylserine Bilayers in the Absence of Salt. *Biophys. J.* **2004**, *86*, 1574-1586.
246. Seidell, A.; Linke, W.F., *Solubilities of Inorganic and Metal Organic Compounds a Compilation of Quantitative Solubility Data from the Periodical Literature*. 1940, D. Van Nostrand Co.: New York.
247. Ruan, C.; Huang, H.; Rodgers, M.T. A Simple Model for Metal Cation-Phosphate Interactions in Nucleic Acids in the Gas Phase: Alkali Metal Cations and Trimethyl Phosphate. *J. Am. Soc. Mass Specrom.* **2008**, *19*, 305-314.
248. Baker, C.M.; Lopes, P.E.; Zhu, X.; Roux, B.; Mackerell, A.D., Jr. Accurate Calculation of Hydration Free Energies Using Pair-Specific Lennard-Jones Parameters in the CHARMM Drude Polarizable Force Field. *J. Chem. Theory Comput.* **2010**, *6*, 1181-1198.
249. Luo, Y.; Jiang, W.; Yu, H.; MacKerell, A.D., Jr.; Roux, B. Simulation Study of Ion Pairing in Concentrated Aqueous Salt Solutions with a Polarizable Force Field. *Faraday Discuss*. **2013**, *160*, 135-149.
250. Skolnick, J.; Fixman, M. Electrostatic Persistence Length of a Wormlike Polyelectrolyte. *Macromolecules*. **1977**, *10*, 944-948.
251. Odijk, T. Polyelectrolytes near the Rod Limit. *J. Polymer Sci. Ploymer Phys. Ed.* **1977**, *15*, 477-483.
252. Sim, A.Y.; Lipfert, J.; Herschlag, D.; Doniach, S. Salt Dependence of the Radius of Gyration and Flexibility of Single-Stranded DNA in Solution Probed by Small-Angle X-Ray Scattering. *Phys. Rev. E Stat. Nonlin. Soft Matter Phys.* **2012**, *86*, 021901.
253. Basu, S.; Venable, R.M.; Rice, B.; Ogharandukun, E.; Klauda, J.B.; Pastor, R.W.; Chandran, P.L. Mannobiose-Grafting Shifts Pei Charge and Biphasic Dependence on Ph. *Macromol. Chem. Phys.* **2019**, *220*.
254. Mark, P.; Nilsson, L. Structure and Dynamics of the Tip3p, Spc, and Spc/E Water Models at 298 K. *J. Phys. Chem. A.* **2001**, *105*, 9954-9960.

255. Åqvist, J. Ion-Water Interaction Potentials Derived from Free Energy Perturbation Simulations. *J. Phys. Chem.-US.* **1990**, *94*, 8021-8024.
256. Perozzo, R.; Folkers, G.; Scapozza, L. Thermodynamics of Protein-Ligand Interactions: History, Presence, and Future Aspects. *J Recept. Signal Transduct. Res.* **2004**, *24*, 1 - 52.
257. Azam, S.S.; Hofer, T.S.; Bhattacharjee, A.; Lim, L.H.; Pribil, A.B.; Randolf, B.R.; Rode, B.M. Beryllium(Ii): The Strongest Structure-Forming Ion in Water? A Qmcf MD Simulation Study. *J. Phys. Chem. B.* **2009**, *113*, 9289-9295.
258. Shinoda, K.; Shinoda, W.; Baba, T.; Mikami, M. Comparative Molecular Dynamics Study of Ether- and Ester-Linked Phospholipid Bilayers. *J. Chem. Phys.* **2004**, *121*, 9648-9654.
259. Pan, J.; Cheng, X.; Heberle, F.A.; Mostofian, B.; Kučerka, N.; Drazba, P.; Katsaras, J. Interactions between Ether Phospholipids and Cholesterol as Determined by Scattering and Molecular Dynamics Simulations. *J. Phys. Chem. B.* **2012**, *116*, 14829-14838.
260. Khalifah, R.G.; Zhang, F.; Parr, J.S.; Rowe, E.S. Thermodynamics of Binding of the Co2-Competitive Inhibitor Imidazole and Related Compounds to Human Carbonic Anhydrase I: An Isothermal Titration Calorimetry Approach to Studying Weak Binding by Displacement with Strong Inhibitors. *Biochem.*. **1993**, *32*, 3058-3066.
261. Zhang, Y.L.; Zhang, Z.Y. Low-Affinity Binding Determined by Titration Calorimetry Using a High-Affinity Coupling Ligand: A Thermodynamic Study of Ligand Binding to Protein Tyrosine Phosphatase 1b. *Anal. Biochem.* **1998**, *261*, 139-148.